Scanning-Tunneling-Microscope investigations on Rb exposed TaS_2 and light emission from silicon

Dissertation
zur Erlangung des Doktorgrades
der Mathematisch-Naturwissenschaftlichen Fakultät
der Christian-Albrechts-Universität
zu Kiel

vorgelegt von
Patrick Schmidt

Kiel 2008

Referent/in: Prof. Dr. Richard Berndt
Korreferent/in: Prof. Dr. Michael Bauer
Tag der mündlichen Prüfung: 10.06.2008
Zum Druck genehmigt: Kiel, den 18.11.2008

Der Dekan

Abstract

Two different aspects of surface science were analyzed in this thesis. First, the light emission properties of single crystal silicon with different orientations and doping were studied using the scanning tunneling microscope. Tunneling electrons excite several optical transitions in silicon bulk. The direct interband transitions are well known, but this is the first time these transitions were observed with scanning-tunneling-microscope induced luminescence. For the case of electron tunneling from the metallic tip of the scanning tunneling microscope into the silicon sample ($V > 0$), a presented model, based on Auger mediated electron-hole recombination, explains the observed light emission spectra. For a change of polarity ($V < 0$), light emission was found only from the reverse driven p-type samples while spectra from the n-type samples appear still dark. A new mechanism of light emission is proposed which explains the experimental observations. The interplay between band bending, Zener tunneling and Auger processes enables light emission in this case. The findings in this study confirm and fulfil the theoretical predictions of direct interband transitions between 3.3 eV and 5.4 eV photon energy under tunneling contacts which have never been observed before experimentally.
Further investigation at substantially higher tunneling currents shows that the energies of a series of quantum well states in silicon, which were induced in the potential well of the band bending, can be resolved within the light emission spectra.

Second, the influence of *in vacuo* Rb adsorption on $1T$-TaS_2 was explored under different aspects. It is known that the Rb drives a Mott Hubbard transition; and, with photo emission spectroscopy, the energy of the lower Hubbard band with respect to the Fermi energy was measured. Concurrently, the adsorbate induces a transition from a $p(\sqrt{13} \times \sqrt{13})R13,9^\circ$ charge density wave into a $c(2\sqrt{3} \times 4)$ one, as observed recently by low energy electron diffraction experiments; and a nanostructured network establishes, as seen by scanning tunneling microscope studies.

In this study the $c(2\sqrt{3} \times 4)$ charge density wave was mapped in real space, and the complete Mott Hubbard gap was measured using scanning tunneling microscopy and scanning tunneling spectroscopy, respectively. Experimental spectroscopy data atop a Rb driven nanostructures indicate that these are most likely not fabricated from Rb. Further, the experimental evidence for the intercalation of Rubidium by using this *in vacuo* sample preparation method was given.

Kurzdarstellung

In dieser Arbeit wurden zwei verschiedene Aspekte der Oberflächenphysik bearbeitet. Die Lichtemission von Siliziumeinkristallen verschiedener Orientierungen und Dotierungen wurde bei Raumtemperatur untersucht. Die Energie der Tunnelelektronen regt im Halbleiter bekannte optische Übergänge an. Der Nachweis dieser Übergänge mittels der Rastertunnelmikroskopie induzierten Lumineszenz wurde erstmals in dieser Arbeit geführt. Für den Fall des Elektronentunnelns in den Halbleiter ($V > 0$) aus der Metallelektrode erklärt ein Modell basierend auf Augereffekt und Elektronen Loch Vernichtung die Emission. Die Lichtemission aus Silizium für Tunnelanregungen war bekannt nur für den Fall der Elektroneninjektion in den Halbleiter. Hier wurde erstmals für Elektronenextraktion aus dem Halbleiter Lichtemission ($V < 0$) nachgewiesen. Dieser neue Effekt tritt nur in p-dotiertem Material auf, während die Spektren von n-dotierten Proben dunkel bleiben. Ein Modell aus Bandverbiegung, Zenertunneln und Auger Prozessen erkärt die Lichtemission für p-Silizium und die fehlende Lichtemission für n-Silizium. Die hier nachgewiesenen Interbandübergänge zwischen 3.3 eV und 5.4 eV Photonenenergie erfüllen die theoretischen Vorhersagen zur Lichtemission aus Metall-Oxid-Silizium Strukuren, die bisher experimentell noch nicht nachgewiesen wurden.
Weitere Untersuchungen bei deutlich erhöhtem Tunnelstrom zeigten sogar, dass die Energien von Lochbändern, die durch die Bandverbiegung induziert werden, mittels Lichtemission bestimmt werden können.

Das Verhalten von $1T$-TaS_2 bei Raumtemperatur und bei 9 Kelvin mit verschiedenen Bedeckungen von Rubidium, welches bei Raumtemperatur auf die Proben aufgedampft worden ist, wurde untersucht. Die großflächige Interkalation des Rubidiums wurde dabei erstmals bei dieser Form der *in vacuo* Probenpräparation nachgewiesen. Die Anwesenheit des Rubidiums induziert bei Raumtemperatur einen Mott-Hubbard Übergang von Metall zu einem Halbleiter. Die Lage der unteren Bandkante ist aus der Photoemissionsspektroskopie bekannt. Die komplette Bandlücke mit beiden Bandkanten wurde im Rahmen dieser Arbeit bestimmt. Zudem verändert das Rubidium die Ladungsdichtewelle des Substrates von einer $p(\sqrt{13} \times \sqrt{13})R13,9°$ zu einer $c(2\sqrt{3} \times 4)$. Die $c(2\sqrt{3} \times 4)$ Ladungsdichtewelle wurde erstmals im Realraum abgebildet. Das Rubidium induziert bei Raumtemperatur ein nanostrukturiertes Netzwerk. Mittels Tunnelspektroskopie konnte gezeigt werden, dass diese Nanostrukturen nicht aus Rubidium bestehen.

Contents

1 Motivation and Introduction **3**
- 1.1 Light emission from silicon under tunneling junctions . . . 3
- 1.2 Rb on TaS_2 . . . 5
- 1.3 Further results . . . 6
- 1.4 Publications . . . 6

2 Scanning Tunneling Microscopy **7**
- 2.1 Principles of Tunneling . . . 7
- 2.2 Imaging with constant current mode and constant height mode . . . 9
- 2.3 dI/dU-Spectroscopy . . . 11
- 2.4 Drift correction method for dI/dU spectra recording at RT . . . 12

3 Light emission from tunneling junctions **15**
- 3.1 Light emission from Metal Insulator Metal systems . . . 15
- 3.2 STM induced light emission from semiconductors . . . 16
- 3.3 Light emission from MOS capacitors . . . 18

4 Experimental **21**
- 4.1 Overview . . . 21
- 4.2 Preparation chambers . . . 21
- 4.3 STM chambers . . . 23
- 4.4 Light emission recording setup . . . 23

5 Sample preparation **26**
- 5.1 Cleaving of TMDCs . . . 26
- 5.2 Silicon samples and preparation . . . 28
- 5.3 The new Si-sample holder . . . 28

6 Silicon **30**
- 6.1 Basic properties of silicon . . . 30
- 6.2 Surfaces . . . 31

7 Ultraviolet light emission from Si in a scanning tunneling microscope **33**
- 7.1 Abstract . . . 33
- 7.2 Introduction . . . 33
- 7.3 Experiment . . . 34
- 7.4 Results and discussion . . . 34
- 7.5 Conclusion . . . 40

8 Efficiency of light and ultraviolet emission from silicon 42
8.1 Introduction . . . 42
8.2 Experimental . . . 42
8.3 External quantum efficiency and silicon surface orientations . . . 42
8.4 Polarity effects on the external quantum efficiency . . . 44
8.5 Conclusion . . . 45

9 C_{60} on n-Si(100) 46
9.1 Introduction . . . 46
9.2 Experimental . . . 48
9.3 C_{60} manipulation and stable structures at extreme tunneling conditions 48

10 Multiple peaks light emission spectra from C_{60} covered n-Si(100) 52
10.1 Introduction . . . 52
10.2 The E_n transitions . . . 54
10.3 Hole-Subbands and light emission . . . 57

11 Structure of *in vacuo* Rb intercalated $1T$-TaS_2 61
11.1 Abstract . . . 61
11.2 Introduction . . . 61
11.3 Experiment . . . 62
11.4 Results and discussion . . . 63
11.5 Conclusion . . . 68

12 Scanning tunnelling microscopy and spectroscopy investigation of rubidium-induced Mott -Hubbard transition on $1T$-TaS_2 69
12.1 Abstract . . . 69
12.2 Introduction . . . 69
12.3 Experiment . . . 70
12.4 Results and Discussion . . . 71
12.5 Conclusion . . . 76

13 Summary 77

A Chemical identification of Se and S in $TiSe_{1.2}S_{0.8}$ using Scanning Tunnelling Microscopy 79

B Molecule powder deposition on Si(100) substrate 86

C List of abbreviations 90

D Thanks and Acknowledgements 91

Chapter 1

Motivation and Introduction

The scanning tunneling microscope (STM) is a powerful tool for investigations on a sub-nanometer scale in real space [1]. The high spatial resolution allows the observation of individual atoms or adsorbates at surfaces and the scanning tunneling spectroscopy allows one to analyze the electronic structure of individual objects, like molecules or adatoms [2]. The tunneling electrons can excite photons [3, 4], offering STM induced light emission spectroscopy [5]. These two modes of spectroscopy are used in this study to analyze the electronic structures of two different physical systems.

1.1 Light emission from silicon under tunneling junctions

Silicon is the most explored material in the world since the importance for commercial devices is so high. One of the basic silicon device is the MOS or MIS capacitor (from Metal-Oxide-Silicon and Metal-Insulator-Silicon) which for example is used to build up MOSFETs (from MOS-Field-Emission-Transistor). And there is of course a great interest in understanding the fundamental behavior of the carrier transport phenomena of MOS or MIS devices. Those structures exhibit light emission under biasing and, interestingly, the light emission from those capacitors is a fundamental aspect of the carrier transport [6, 7].

The light emission from MOS or MIS capacitors exhibit photon energies up to $\hbar\omega \approx 3.5$ eV [6,8–11], which is well understood, but several theoretical investigations predict the presence of characteristic direct interband transitions in silicon bulk between 3.3 eV and 5.4 eV photon energy [8–11]. But the energy of the emitted photons from MOS structures is limited to $\hbar\omega \approx 3.5$ eV due to the oxide breakdown [6, 8], and higher photon energies were not observed experimentally.

The STM can be understood as a simplified MOS/MIS structure since, between metallic STM-tip and the semiconductor, an insulating vacuum gap is present. Furthermore effects related to the oxide can be neglected, and indeed "oxide breakdown" did not happen in the STM experiments which enable the emission of higher photon energies from the silicon. Energy resolved light emission spectra ranging from 1.7 eV to 5.9 eV photon energy were recorded from single crystal silicon with different

surface orientations and doping. Within the recorded spectra, the above mentioned characteristic direct interband transitions in silicon bulk between 3.3 eV and 5.4 eV photon energy were successfully resolved and fulfil the theoretical predictions [8–11].

The light emission from MOS structures was known only for the case of electrons tunneling from the metal electrode into the semiconductor [6, 12]. For opposite current direction no light emission was observed from MOS or MIS capacitors, and indeed, for the n-Si samples no light was detected when the electrons tunnel from the silicon into the metallic STM-tip. Surprisingly, light emission from p-Si(111) samples was observed and the spectra exhibit the same direct interband transitions as in the case of electron tunneling into the semiconductor. In this study a new mechanism for light emission is proposed for the case of electrons being extracted from p-type silicon.

There is also a fundamental interest in light emission from STM since the STM combines light emission with a high spatial resolution [5]. Several studies have tried to explore the STM induced luminescence from silicon [3, 13–15] but have not come up with a satisfactory explanation of these phenomena yet. In the above mentioned studies three different interpretations on the origin of the light emission were given.

In the study done by *Gimzewski et al.* [3] p-Si(111) samples were used and isochromat spectra were presented. For isochromat spectra, the intensity of photons at an energy of $\hbar\omega \approx 9.5$ eV was recorded, while the applied bias between STM-tip and the sample was changed from 2 V to 20 V. *Gimzewski et al.* concluded that the light emission correlates with the emission one can get from inverse photo emission spectroscopy (IPES) experiments.

Later *Downes et al.* in Ref. [15] observed light emission from Si(111) at substantially lower photon energies using a photomultiplier tube. The emission process is suggested to result from a local plasmon decay, as known from systems where the STM tip and the sample were made of metal [16].

In studies done by *Thirstup et al.* and *Sakurai et al.* [13, 14] Si(100) samples of $p-$ and n-type (boron-doped, $1{\times}10^{18}$ cm^{-1}; and antimony-doped, $1{\times}10^{18}$ cm^{-1}, respectively) were used. Isochromat spectra were recorded for several photon energies between 1.5 eV and 3.1 eV, and the applied biases ranging from -10 V to 10 V. Light emission was detected from each sample type and for both polarities of the applied voltage. In there, plasmon decay is excluded to be responsible for the light emission. Instead, it is suggested that inelastic tunneling, where the tunneling electron looses the energy $\hbar\omega$ during tunneling between the tip state and the surface state of the silicon (or vice versa for changing of the bias polarity), is responsible for the light emission.

The different interpretations of recent light emission studies show that further investigations are useful, and the first aim of this study is to explain the STM induced light emission from silicon samples. In this study a set of Si samples (B doped p-Si(111), 9.7×10^{15} cm^{-3}; P doped n-Si(111), 7.9×10^{13} cm^{-3}; P doped n-Si(100), 4.5×10^{14} cm^{-3}) was used. The energy resolved spectra allow a clear interpretation of the data, which is in contrast to the explanations published in previous STM studies.

Semiconductors driven under revers bias show the effect of band bending. The bands bend upwards or downwards and a potential well is created at the surface, where additional quantum well states appear [17]. Access to these quantum well states in silicon (or type IV-semiconductors) is given using cyclotron resonance or Shubnikov-de Haas oscillations [18–21] or magnetotunneling [22]. Recently, it has been shown that these states can also be visualized with angle resolved photo emission spectroscopy (ARPES). The light emission from silicon results from direct interband transitions in silicon bulk, and hence it might be possible to find a signature of these quantum well states within the light emission spectra. Indeed, for substantially higher tunneling currents, two series of additional peaks appear in the light emission spectra. The peaks can be tentatively attributed to transitions into these quantum well states. STM induced luminescence offers a new way to explore the nature of these quantum well states.

1.2 Rb on TaS_2

Transition metal dichalcogenides (TMDCs) have attracted considerable attention. These materials can serve as the basis for lubricants [23], battery systems [24], and solar cells [25]. From a fundamental point of view TMDCs present a material class with intriguing phase diagrams which include metal-insulator transitions, charge density waves (CDW), and superconductivity [26, 27]. Owing to their peculiar geometric structure which consists of a periodic stacking of van der Waals-bonded TMDC layers, dimensionality effects on the above mentioned phases can be investigated. Many *in vacuo* photoemission experiments on alkali metal adsorption on TMDC materials show that local changes in the host metal d band are evident upon deposition [28–30]. However, the location of the alkali metal cannot be directly determined from such measurements.

Rossnagel et al. have demonstrated (by an angle-resolved photo electron spectroscopy (ARPES) experiment) the continuous tuning of electronic correlations by *in vacuo* Rb adsorption on $1T$-TaS_2 [30]. Charge transfer from the alkali metal to the substrate and simultaneous modification of the interlayer coupling were suggested to drive a Mott Hubbard type transition at the surface [30].

Clean $1T$-TaS_2 exhibits at RT an incommensurate $p(\sqrt{13} \times \sqrt{13})$R13.9° CDW which is suggested to alter upon Rb deposition into a $c(2\sqrt{3} \times 4)$ CDW as seen with low energy electron diffraction (LEED) measurements [30, 31].

STM studies have shown that the exposure to large amounts of metal adatoms drives the formation of nanostructures on the surface of $TiTe_2$ (also TMDC) and similar materials [31–33]. These studies have suggested that the alkali atoms remain on the surface forming nanostructures, and that no intercalation takes place. A recent SEM study on the other hand shows that introducing Cu adatoms to VSe_2 (also TMDC) drives a deformation of the top layers such that a nanofold network formation appears [34].

In this thesis scanning tunneling microscopy and spectroscopy data are presented for the clean and Rb covered $1T$-TaS_2 surface at 9 K and at room temperature. By comparing step heights of the clean surface with those of Rb-exposed samples, a

clear evidence of Rb atoms intercalation between the substrate layers is given. The increase of the step heights of TaS_2 is in accordance with a model presented in this thesis. The Rb atoms occupy adsorption sites within the van der Waals gap of the substrate.

On the surfaces of clean and Rb exposed $1T$-TaS_2 the incommensurate $p(\sqrt{13} \times \sqrt{13})$R13.9° CDW and the Rb modified $c(2\sqrt{3} \times 4)$ CDW, respectively, are observed in direct space.

The Mott-Hubbard transition of $1T$-TaS_2 for *in vacuo* Rb deposition is observed using scanning tunneling spectroscopy; and the onsets of the upper and lower Hubbard bands are found in the spectroscopy data. Since scanning tunneling spectroscopy comes along with the high spatial resolution of the STM, the distribution of the electronic states can be estimated at several points of particular interest on the surface, as for example atop a Rb driven nanostructure. The spectral signature indicates that the nanostructrures were most likely not made of Rb.

The research on TaS_2 was supported by the projects KR 2912/3-1 and FOR 353/2-2 of the Deutsche Forschungsgemeinschaft.

1.3 Further results

A model for chemical identification of individual S and Se atoms embedded into the $TiSe_{1.2}S_{0.8}$ surface -also a member of the family of TMDCs- is proposed in the Appendix A.

In Appendix B a new and fairly simple preparation method for molecules on Si(100) is explained. This may be important for those who work with molecules representing a class of molecules which cannot be deposited on sample surfaces with standard preparation procedures. As a result, individual molecules are resolved and different coverage at one sample surface within one preparation cycle are found.

1.4 Publications

Most of the work contained in this thesis has been published elsewhere. This part of the chapter contains a summary of my relevant publications.

Chapter 7 is published in *Physical Review Letters* **99**, 246103 (2007). [35]

Chapter 12 is published in *New Journal of Physics* **10**, 13022 (2008). [36]

Chapter 11 is published in *Physical Review B*, **74**, 193407 (2006). [37]

Text and figures of the above mentioned chapters are identical with the published one. The references of the publications are included in the bibliography at the end of the thesis.

Chapter 2

Scanning Tunneling Microscopy

This chapter gives a brief introduction into STM. Starting with the basic principles of the quantum mechanical tunneling process, the modes for imaging and tunneling spectroscopy are explained.

2.1 Principles of Tunneling

In classical mechanics it is not possible for a particle (e. g. an electron) with the energy E to overcome a potential barrier V_0 if the barrier V_0 is higher than the particle's energy E. The particle is reflected as depicted in Fig. 2.1. Only in case of $E > V_0$ the particle will pass the barrier.

In a scanning tunneling experiment an atomically sharp metallic tip is positioned above a surface at a distance of a few Å. For electrons in the tip the vacuum gap is a barrier (Fig. 2.1b). An electron inside the tip is described by its oscillating wave function Ψ_0. In the barrier region (with $E < V_0$) the wave function decays and is again of oscillating behavior inside the sample. Since $|\Psi^2(z)|$ is the probability to find the electron at the position z, the probability to find the electron in the sample is higher than zero, although its energy E is smaller than the barrier height V_0. Solving the Schrödinger equation for a step-like barrier (see e.g. [38]), one obtains the following equation for the transmitted wave function Ψ inside the barrier:

$$\Psi = \Psi_0 e^{-\kappa z}, \quad \kappa = \frac{\sqrt{2m(V_0 - E)}}{\hbar} \tag{2.1}$$

in which Ψ_0 represents the incoming wave function, κ the decay constant, z the width and V_0 the height of the barrier, m the mass and E the energy of the electron, and $\hbar$ representing Planck's constant divided by 2π.

When a voltage U is applied between tip and sample, the tunneling electrons lead to the following current

$$I \sim |\Psi|^2 \sim U e^{-2\kappa z}. \tag{2.2}$$

The current depends exponentially on the width of the tunneling barrier. With a typical barrier height of 4 - 5 eV for metal electrodes κ becomes $\approx 1\,\text{Å}^{-1}$. By increasing the barrier width by 1 Å the current decreases by about one order of

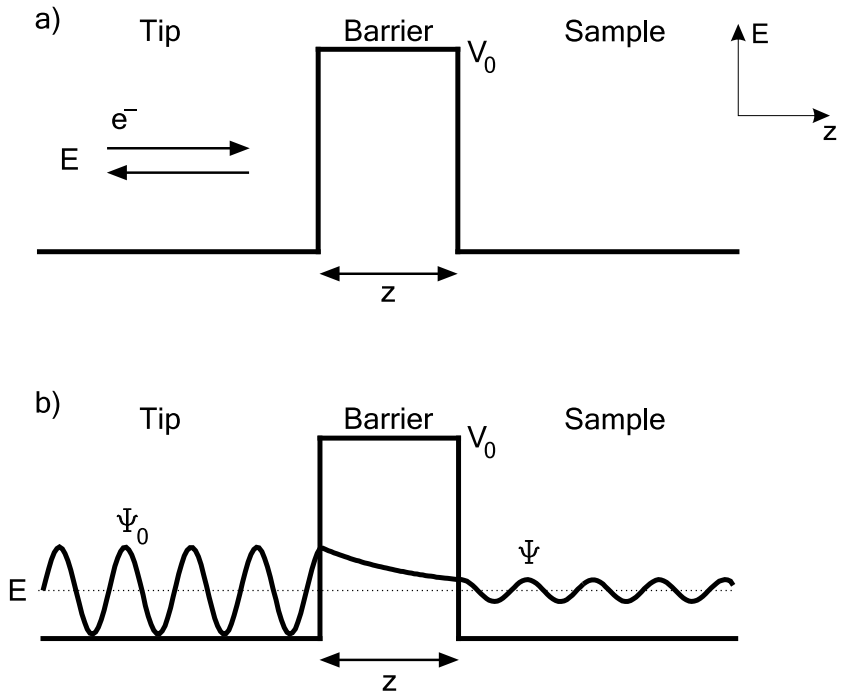

Figure 2.1: The tunneling effect. a) Situation for classical mechanics. The electron cannot pass the barrier if its energy E is lower than the barrier V_0. b) In the quantum mechanical situation the electron wave function Ψ_0 decays in the barrier and still exists in the sample. This means the probability for finding the electron in the sample is higher than zero. The electron can pass the barrier by tunneling through the barrier. Adapted from Ref. [39].

magnitude. This strong exponential behavior in the tunneling current is responsible for the high resolution of the STM.

Detailed analysis of the tunneling current [40–42] leads to the tunneling current density j:

$$j \approx \frac{2\pi e}{\hbar}\left(\frac{\hbar^2}{2m}\right)^2 \int_{-\infty}^{\infty} T(E,U,z)[f(E+eU)-f(E)]\rho_T(E+eU)\rho_S(E)dE, \quad (2.3)$$

where e denotes the electron charge, $f(E)$ the Fermi function, E the energy, U the applied voltage, and ρ_T (ρ_S) the local density of states (LDOS) of the tip and sample, respectively. The transmission coefficient T is defined as

$$T(E,U,z) \approx \exp\left\{-2z\sqrt{\frac{2m}{\hbar^2}\left[\bar{\Phi}+\frac{eU}{2}-(E-E_{||})\right]}\right\} \quad (2.4)$$

with E_F the Fermi energy, z the distance, $\bar{\Phi}$ the average of work function of the tip and the sample, and $E_{||}$ the energy of the electron in the surface plane. Beside the distance dependency information about the LDOS of the surface, ρ_S, and the tip ρ_T, is given – the latter is usually assumed to be constant [40, 41]. At sufficiently low temperatures, the Fermi functions in (2.3) can be approximated by step functions,

and the limits of the integral converge to E_F (Fermi energy, chosen to be 0) and $E_F + eU$. The current can be approximated by the following equation

$$I \propto \int_0^{eU} \rho_S(E_F + E)T(E_F + E, U, z)dE \tag{2.5}$$

While tip and sample are separated, the vacuum levels are the same, whereas the Fermi levels $E_{\mathrm{F,T}}$ and $E_{\mathrm{F,S}}$ adjust to each other when tip and sample reach tunneling contact (Fig. 2.2). Electrons start to tunnel from tip to sample and vice versa, but the net current remains zero. As soon as a voltage is applied between tip and sample a net current from occupied states of the tip to unoccupied states of the sample (or vice versa, depending on the voltage polarity) can be measured. The resulting current is proportional to the sum of the density of unoccupied states, weighted by the transmission coefficient as described by (2.5).

2.2 Imaging with constant current mode and constant height mode

Topographical imaging is the mode where sample surfaces can be resolved with atomical resolution or individual molecules can be observed in great detail.

The tip is positioned over the surface by a piezo ceramic device, which can move the tip in x-, y- and z-directions (Fig. 2.3a). Piezo ceramics are materials that elongate or contract when a voltage U_Z is applied to them. The piezo constant at room temperature is 14.5 Å/V for the z-direction. The limit for controlling the elongation and retraction of the piezo given by the noise level of the apparatus can be controlled with a precision of 0.0011 Å [43]. When the tunneling voltage U_{T} is applied between tip and sample, a current I_{T} consisting of tunneling electrons can be measured. To keep the current I_{T} constant while the tip is moving over the surface in the xy-plane, the control unit (*feedback loop*) adjusts the distance z by varying the voltage U_z applied to the z-piezo. Recording the changes in U_z in dependence of the x/y-position, one obtains detailed information about the LDOS according to (2.5). Since the tunneling current is an integral over the LDOS, areas of different LDOS may appear as protrusions or indentations. Depending on the voltage, adatoms can appear as protrusions, indentations [44], and they can disappear completely in the images [45]. Because the images obtained do not necessarily show the real topography of the surface, it is reasonable to use the term *Constant Current* images instead of *topographies*.

An alternative to the Constant Current mode is the Constant Height mode (Fig. 2.3b). While in constant current mode, the tip-sample distance is adjusted to keep the current constant. In constant height mode, the tip scans in a defined x, y-plane over the surface and the tunneling current I_{T} in dependance of the x, y position gives the STM image. By using this operation mode the tip can scan faster over the surface, but there is a risk of the tip colliding with the sample or loosing the tunneling contact.

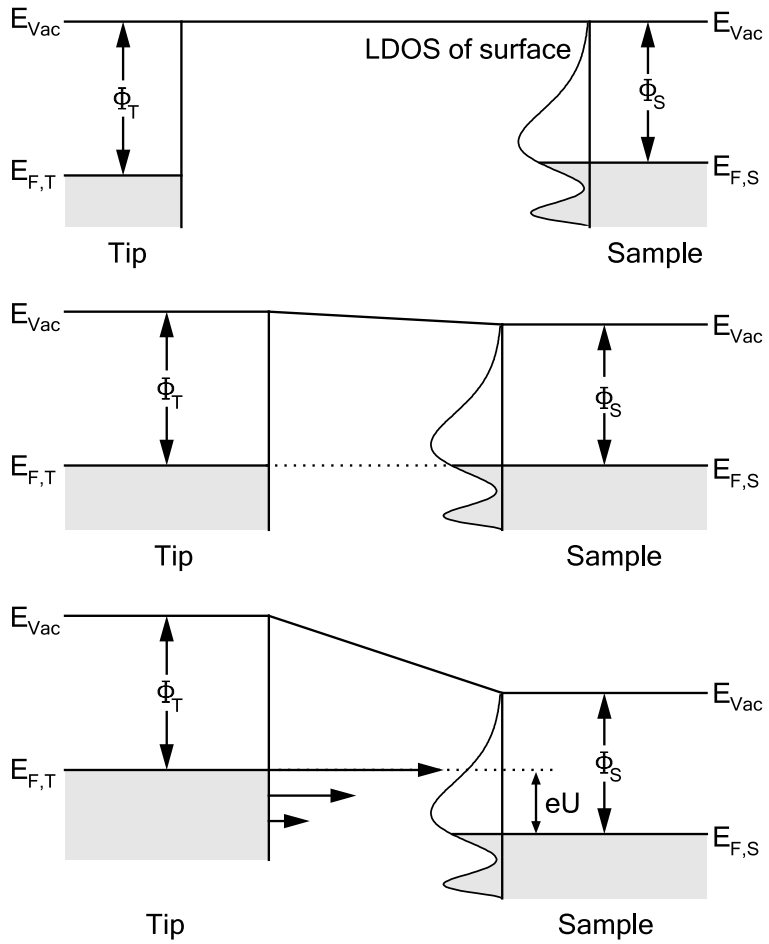

Figure 2.2: Energy levels of tip and sample. The energy bands of tip and sample are filled up with electrons to the level of the Fermi energies $E_{\mathrm{F,T}}$ and $E_{\mathrm{F,S}}$. The difference between the vacuum energy levels and the Fermi levels are the metal work functions Φ_T and Φ_S. Top: Tip and sample are separated, the vacuum energy levels E_{Vac} are the same. Middle: Tip and sample are in tunneling contact and the Fermi levels $E_{F,S}$ and $E_{F,T}$ adjust to each other. Bottom: A voltage U is applied and electrons are tunneling from occupied states of the tip to unoccupied states of the sample. Adapted from Ref. [43].

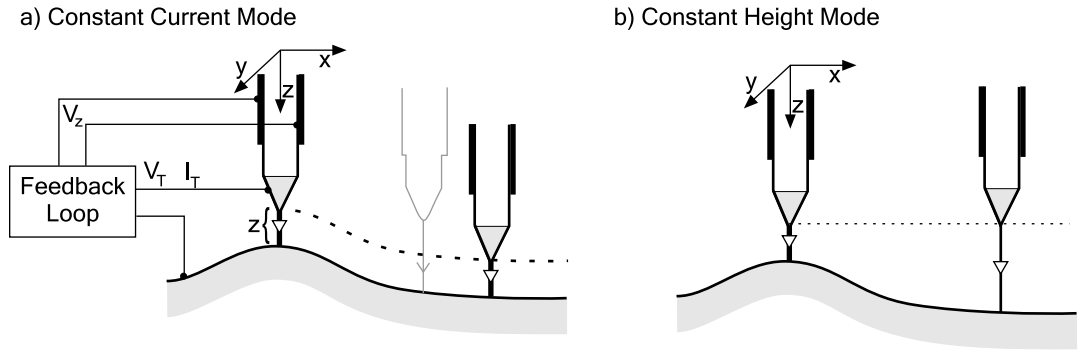

Figure 2.3: The two modes of operation of the STM. a) Constant Current Mode. While scanning the tip over the surface in the x, y-direction, the height z of the tip is adjusted by the feedback loop to keep the current I_T constant. The adjustments of the tip (U_T) carry the LDOS information. b) The tip is driven in even x, y plane over the surface referred to as the Constant Height Mode. Since the current depends on the distance z between tip and surface, the current contains the information about the LDOS. Adapted from Ref. [46].

2.3 dI/dU-Spectroscopy

The tunneling current I depends on the integration of the surface LDOS in equation (2.5) which makes it difficult to obtain information about the LDOS at a certain energy level. Taking the derivative of the tunneling current solves this problem:

$$\begin{aligned}\frac{dI}{dU} \propto\ & \rho_S(E_F+eU)T(E_F+eU,U,z) \\ & + \int_0^{eU} \rho_S(E)\rho_T(E+eU)\frac{dT(E,U,z)}{U}dE \\ & + \int_0^{eU} \rho_S(E)\frac{d\rho_T(E+eU)}{dU}T(E,U,z)dE\end{aligned} \tag{2.6}$$

The second and the third term of this sum are proportional to dT/dU and $d\rho_T/dU$, respectively, and can be neglected under the assumption that T varies only monotonously with U and with a constant set LDOS ρ_T of the tip.

Then the derivative dI/dU is approximately proportional to the surface LDOS:

$$\frac{dI}{dU} \sim \rho_S(eU)T(eU,U,z) \tag{2.7}$$

The easiest way to obtain dI/dU is to measure $I(U)$ and calculate the derivative numerically. But these experimental data always contains a noise of low amplitude at high frequency compared to the features related to LDOS of the undisturbed data. It is better for dU/dU-spectroscopy to measure the derivative of the tunneling current directly using a lock-in technique [48–50].

2.4 Drift correction method for dI/dU spectra recording at RT

During spectra recording the tip sample distance z has to be held constant. Then the total derivative in the second term of Equation 2.6 does not influence the $dI/dU(U)$ spectra and the integral of the second term can be neglected. The Lock-in technique is well established for STMs working at low temperatures where drift effects do not play a role and the tunneling gap can easily be kept constant with disabled feedback loop during dI/dU spectra recording. The usage of this mode at room temperature is difficult since drift is always present and the tunneling gap cannot be kept constant easily. Here the Lock-in mode was implemented successfully in the room temperature STM because drift effects were successfully compensated during spectra recording.

Drift in STM is caused by two effects [51]. First, one type of unintended moving is caused by the movement of the piezo and is named *creep*. If the tip moves a certain distance, the piezo follows; but the movement of the piezo induces creep, resulting in an unintended movement of the tip. If present, creep may effect tip motions in the z-direction as well in the x, y-plane. To minimize creep effects in STM experiments the distances for tip movements should be reduced. The use of only soft motions, the effect of creep can be reduced to 0.05 Ås^{-1} in the x, y-plane. In Fig. 2.4a an example of a z-piezo voltage recording is presented. Within the first ten minutes after reaching the tunneling contact, the piezo voltage exhibits a non-linear behavior in time, as can be seen by eye. This non-linear behavior was introduced by piezo creep since, during the previous approaching procedure of tip and sample the piezo was elongated and contracted several times over the entire travelling way. After ten minutes the z-piezo voltage exhibits a more linear behavior. This linear behavior is related to the second type of unintended piezo movement named *drift*.

Drift maybe induced by temperature changes, which have an influence on the piezo constant. But more critical are temperature changes of the whole STM which cause in thermal expansion or shrinking of the STM which in turn changes the tip sample distance[1].

An example of z-drift recording is shown in Fig. 2.4a. After 17 minutes the z-drift remains at a linear level as shown in Fig. 2.4b.

The linear drift can be compensated by applying an additional voltage ramp on the piezo during dI/dU spectra recording so that the piezo moves with the same speed as the drift but in the opposite direction. For testing the conditions of a constant tip sample distance, the tunneling current is measured for the same time as for dI/dU spectra recording (or longer) with disabled feedback loop for the constant applied voltage. For ideal z-drift compensation, the tunneling current is constant over the entire time since the applied voltage is not altered. Fig. 2.5 shows an example of such a test with adjusted z-drift compensation.

The tunneling current was recorded on a clean $1T$-TaS_2 surface for more than

[1]Since the room where the STM is located has temperature changes over the day due to changes of the sunlight behavior, it might be a promising alternative to perform measurements during the night.

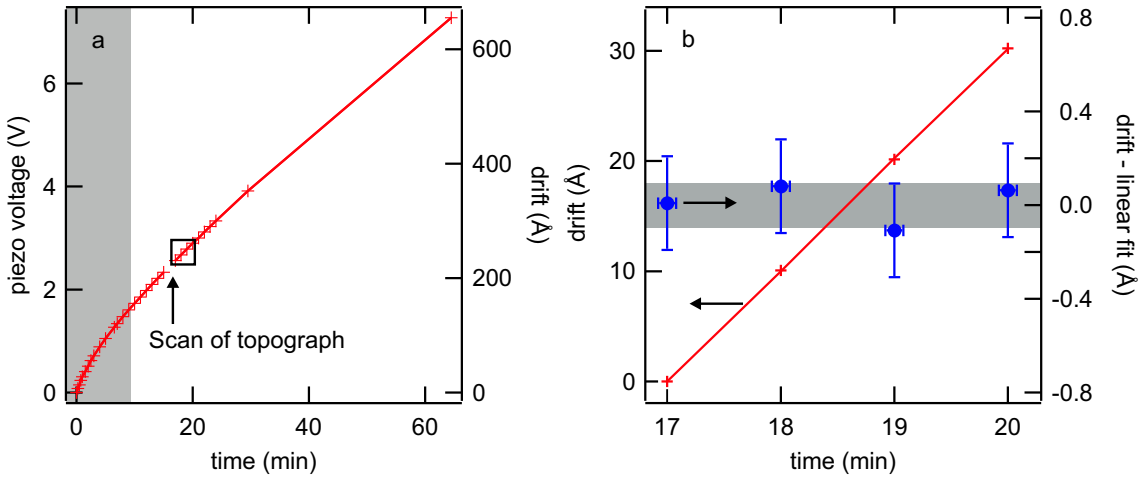

Figure 2.4: (a) Drift recording immediately after the tip has reached the tunneling contact. Left axis displays the piezo voltage and right axis shows the z-drift as calculated from the known piezo constant. The crosses represent data points. The solid line guides the eye. The non-linear drift behavior in the first 10 minutes (grey shaded area) becomes more linear with time. A STM topography was taken between the 16th and 17th minute (indicated by arrow). The data points inside the rectangle are enlarged as displayed in (b). (b) Drift between the 17th and 20th minute after tunneling contact. The solid line represents a linear fit through the data points. On the right axis the differences between this linear fit and the data points (blue circles) are displayed. Note, the maximum deviation from linear behavior is 0.1 Å. The error bars result from errors of observation (1 mV $\approx$ 0.1 Å of piezo voltage and 5 s in time).

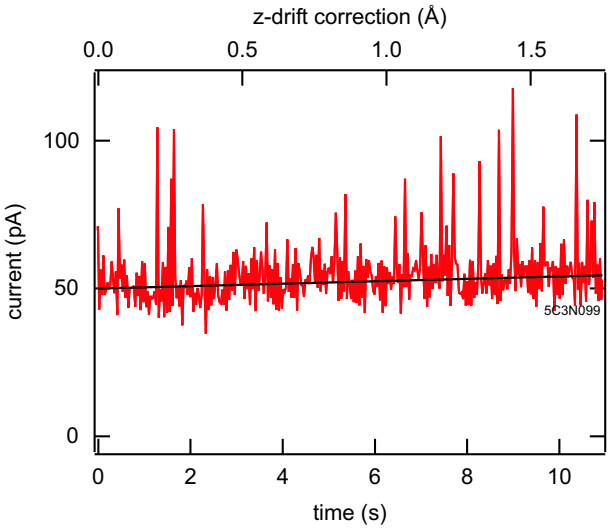

Figure 2.5: An example of z-drift correction on clean TaS_2. The feedback loop is disabled at $t = 0$ s ($U_T = 50$ mV) and the tunneling current was recorded for more than 10 s. The thick solid line represents the trend of the tunneling current (see text). The z correction during this time is $\approx$ 1.7 Å.

10 seconds, whereas the STM-tip is retracted by ≈1.7 Å for drift compensation (upper axis). The current exhibits several peaks ranging from 50 pA to 120 pA. This is typical for such a sample. The remaining noise in the tunneling current is the normal instrumental noise. The thick solid line represents a linear fit of the tunneling current without these peaks. The set tunneling current changes from 50 pA to 55 pA at the end of the data recording. Assuming that a change in tip sample distance of 1 Å would result in a change of the tunneling current by one order of magnitude, the change in tip sample distance here is in the range of 0.01 Å. This indicates that the tip sample distance was kept "nearly" constant and dI/dU spectra should not be influenced by artifacts caused by drift.

The dI/dU spectra presented in Chapter 12 are recorded with this correction mode.

Chapter 3

Light emission from tunneling junctions

Light emission from STM experiments is a topic of interest since Gimzewski *et al.* [3] reported about the possibility to observe light origin from the STM tunneling junction. Here the hope of observing light, which is characteristic in a way that sample material properties like electronic states can be extracted, was first inspired.

Three different systems resulting on light emission from a tunneling junction could be distinguished. First, the emission from tunneling junctions where the electrons tunnel through an insulating layer between two metal electrodes (named MIM contacts) is described. The light emission from STM tunneling junctions with metal sample and metal tip -mostly made of gold or silver- and an insulating vacuum barrier are ranked in this group as well. Second, an overview about the light emission from STM experiments, where the tip is made of metal and the sample is a semiconductor, is given. Within this class it is important to differentiate between indirect and direct semiconductors. And third, the light emission from electronic devices, which are based on the tunneling of carriers like metal-oxide-semiconductor (MOS) or metal-insulator-semiconductor (MIS) devices as their simplest application, is now described in detail.

3.1 Light emission from Metal Insulator Metal systems

Light emission from tunneling junctions which were made of two metal electrodes is a known phenomenon. The two metal electrodes separated by a thin insulating layer show light emission due to surface plasmon decay [53–55]. In principle, this process is responsible for STM induced light emission as well, if the tip and the sample are metals [16, 56–60]. The light emission can be understood here as a two step process. First, an electron tunnels inelastically (see Fig. 3.1) and excites a localized plasmon in the tunneling gap which then may decay by emitting a photon in the second step. The energy of the emitted photons is related to the energy of the localized plasmon. The energy of the emitted photons can be easily tuned by the applied bias between tip and sample. It is astonishing that the spatial resolution gained by this

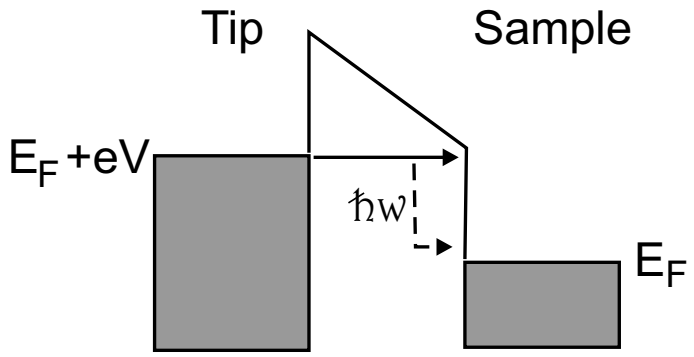

Figure 3.1: A schematic diagram of a tunneling barrier for positive sample voltage V. The solid line represents elastic tunneling and the dashed line shows inelastic tunneling while a local plasmon with the energy $\hbar\omega$ is excited. E_F stands for the Fermi energy.

experiments can reach the sub-nm range [5, 15, 16, 61–69].

Recently, light emission from STM was observed from metallic quantum well states in Na overlayers on Cu(111) [70]. Also, light was detected from adsorbed molecules on several substrates [71–76]. The metallic substrates were prepared with insulating layers of salt or oxide on which the molecules were deposited, or multilayers of molecules were adsorbed onto the metallic sample surfaces.

3.2 STM induced light emission from semiconductors

Prominent samples for STM induced light emission experiments are semiconductors which exhibit a direct band gap. One of the first STM luminescence studies was performed on a GaAs/AlGaAs crystal [4]. These semiconductors are known to emit light under excitation from tunneling electrons. The band gap and the donor/acceptor states are found in the light mission spectra [12, 77–82].

While on metals the light emission is excited in the tunneling gap region [16], the luminescence from direct semiconductors occurs inside their bulk [79, 80, 83]. In the case of an electron tunneling from the tip into the semiconductor, the electron is injected energetically above the conduction band edge, see Fig. 3.2a. After energy dissipation, e.g. by electron-phonon scattering, the electron reaches the conduction band edge inside the bulk where it recombines with a hole from the valence band edge by emitting a photon [12, 84]. This process is valid for p-type semiconductors. The injected electron is a minority carrier and holes in the valence band edge are present for radiative recombination.

Above a specific bias the injected electrons have enough energy to generate holes by Auger processes, see Fig. 3.2b. These holes can then recombine radiatively with an electron in the conduction band edge [85]. Thus, this process of light emission is also valid for n-type direct semiconductors.

For the opposite polarity where electrons tunnel from the semiconductor into

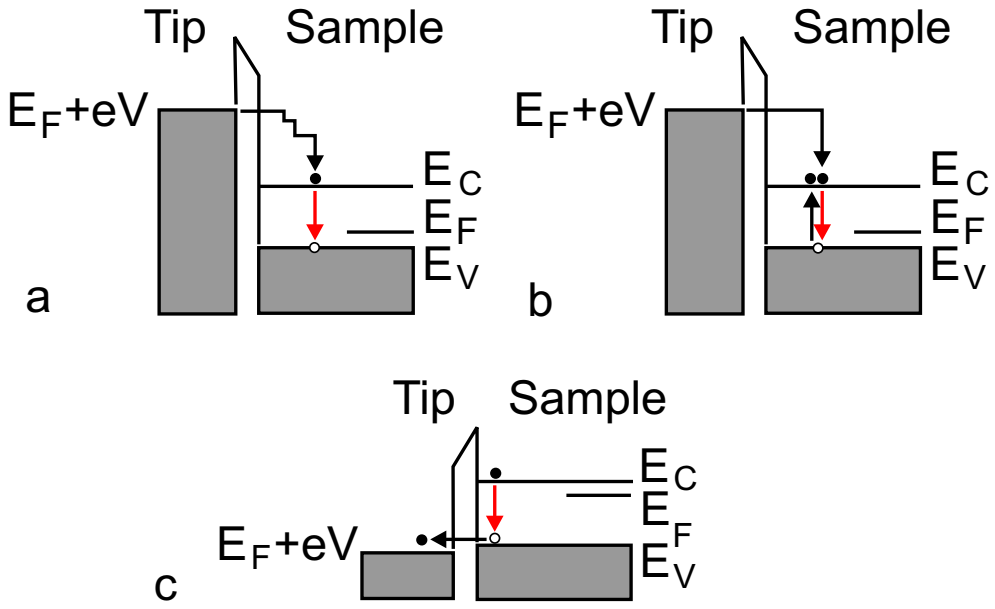

Figure 3.2: Schematic diagrams for light emission processes in direct semiconductors. The red arrow indicates the radiative electron-hole recombination. Band bending effects are neglected in the figure.

the STM tip a light emission mechanism was found for n-type semiconductors, see Fig. 3.2c. The tunneling current consists not only of electrons formerly in the conduction band edge, but also of electrons which tunnel from the valence band edge to the tip, leaving a hole in the valence band edge which recombines with an electron from the conduction band [79, 82].

One of the major drawbacks of silicon is the indirect band gap, which reduces the conduction band edge to valence band edge radiation since an additional phonon is required, see e.g. [12] and citations therein.

An approach to obtain luminescence from silicon is to use porous silicon. The indirect band gap shifts to a direct band gap if the silicon grains are reduced in size and luminescence efficiency is enhanced [87–89]. Reviews of luminescence from this material are given in Refs. [12, 90]. Since porous silicon reaches surface resistivity of around $10^9\,\Omega$cm [90] only thin layers of porous silicon can be used for STM investigations [12, 64, 90–94]. The porous layer is assumed to consist of small randomly orientated single silicon crystals separated by electrically passivated regions. The luminescence is attributed to electron hole pair recombination inside such a small grain of single Si crystal [12]. The spectral signature was observed for 3, 6 and 9 nm sized individual nanoparticles embedded in the porous layer where a blueshift with decreasing particle size is measured [64, 94]. Theoretical investigation support this observation since the gap between conductance and valence band opens for smaller cluster sizes [95].

Apart from Refs. [3, 13–15] no further investigations were reported on single crystal silicon dealing with light emission from STM. The reason for this is the weak luminescence associated with the low detection efficiency of the recording setup

[96–98]. Recent publications present isochromat spectra[1] at different photon energies ranging from 1.55 eV to 3.1 eV[2] from clean (p- and n-) Si(100) with STM tips made of tungsten [13, 14]. The mechanism of the light creating process as described in there is as follows: An electron tunnels inelastically from a tip state to a surface state of the Si(100) sample (or vice versa for bias polarity switching) by emitting a photon. The overall quantum efficiency for the emitted light is estimated to 10^{-7} photons per tunneled electron (in agreement with the efficiency found in this study) and light was detected for the case of electron tunneling from the tip into the sample as well as for the opposite polarity for p- and n-Si(100).

In another investigation Ref. [15] on the other prominent silicon surface Si(111), light emission was observed using tungsten tips with an estimated quantum efficiency of $\approx 10^{-7}$ photons per tunnelling electron. The light emission is attributed to inelastic tunneling and radiative plasmon decay as known from MIM systems[3]. Interpretation of the data presented in the above mentioned Refs. [13–15] was hindered by the fact that no energy or wavelength resolved spectra were presented.

The interpretation of the light emission spectra presented in this thesis is in contrast to the given interpretations of Refs. [13–15]. The underlying process for light emission is related to electron-hole recombination in silicon bulk, as observed from MOS or MIS devices.

3.3 Light emission from MOS capacitors

The electroluminescence from MOS or MIS structures results from energy relaxation of the tunneled electrons from the negatively biased metal electrode. Note, the luminescence from pn-junctions [105] or n-channel MOSFETs [106] results from heating the injected electrons in the space charge layer, and in MOS capacitors the electron is injected well above the conduction band and looses energy during relaxation processes, like phonon scattering or photon emission. Four different types of radiative transitions are known which are displayed in Fig. 3.3, namely:

1. indirect conduction band to conduction band (c-c)
2. direct conduction band to conduction band (c-c),
3. indirect conduction band to valence band (c-v) and
4. direct conduction band to valence band (c-v).

Several authors calculated the light emission spectra [8, 9, 11, 107] for MOS devices and for high biases, applied between metal electrode and semiconductor surface.

[1] An isochromat spectra displays the intensity within an interval of photon energy at a set photon energy in dependance of the applied voltage.

[2] Filter bandwidth 40 nm.

[3] The surface plasmon of the Si(100) surface is known to have an energy of about 12 eV [99] but the Si(111) surface remains to be metallic [100–104] and a surface plasmon may appear at this surface.

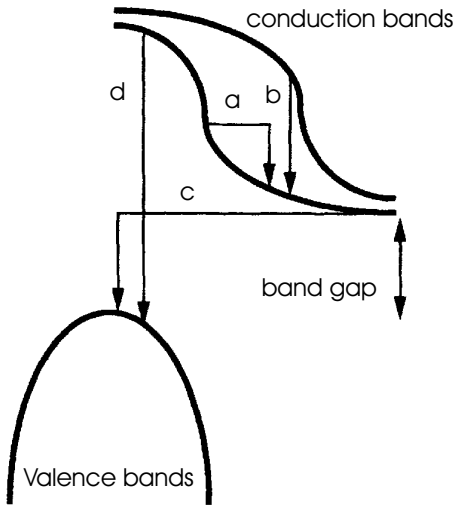

Figure 3.3: Distinction of various luminescence mechanisms in a semiconducting band structure. (a) Indirect c-c (b) direct c-c (c) indirect c-v (d) direct c-v. Adapted from [9].

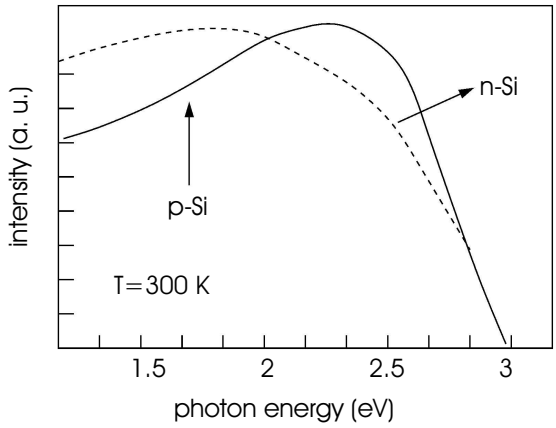

Figure 3.4: Data from the first recorded light emission spectra from MOS structure [10]. Adapted from [6].

Moreover peaks were predicted which result from direct c-v transitions at critical points in the silicon Brillouin zone [8]. At energies of ≈ 3.4 eV and ≈ 4.3 eV the spectra should exhibit two clearly resolved peaks[4]. But oxide breakdown avoids the light emission from MOS or MIS devices at such high photon energies. For lower photon energies in the 1.7 eV to 3 eV range the emitted spectra is supposed to be featureless as observed from experiments [6, 8–11], see Fig. 3.4. Experimental evidence for higher photon energies are not reported in literature since the formerly mentioned oxide breakdown prevents that any higher voltage is being applied [108].

The situation in the STM can be understood as a MOS/MIS device with altered structure since a metal electrode (tip) and silicon sample are separated by an insulating vacuum gap. The STM experiment has the advantage that higher voltages can be applied and oxide breakdown does not happen. Indeed, it is possible -as done in this study- to extend the photon energy range up to 5.9 eV, which moakes out the limit of the detection setup.

It is known that light emission from MOS or MIS devices does not occur for the case of electron tunneling from the semiconductor into the metal electrode. Since the STM is an analogy to MOS/MIS structures, one could expect to observe no light emission from STM under this current direction. And for n-type silicon samples this expectation is fulfilled. But light emission is found here from p-Si(111) in the case of electron tunneling from the semiconductor into the STM-tip. A process never observed previously for light generation from silicon was discovered and a model for explanation is proposed in Chapter 7.

[4]Each of this two peaks consists of several c-v transitions which are grouped around this two peaks.

Chapter 4

Experimental

The work in this thesis was carried out with two home build ultrahigh vacuum (UHV) scanning tunneling microscopes (STMs), optimized for work at room temperature (RT) and low temperature (LT) at 9 K. The RT-STM was designed and built by Dr.Thomas Jürgens [43] and the LT-STM was designed and built by Dr. Jörg Kröger and collaborators [39,50]. The photon detection setup for light emission experiments was established by Germar Hoffmann [97, 109] and the optical unit at the room temperature STM was improved during my diploma [110].

4.1 Overview

The Figs. 4.1 and 4.2 show technical drawings of the apparatus used for the experiments. Each system consists of an analysis chamber which contains the STM (and in LT case the cryostat as well) and a preparation chamber. In both cases a small fast-entry load lock for moving samples, tips, and evaporators into the apparatus without breaking the UHV is mounted on the preparation chambers. The vacuum is generated by combinations of turbo molecular drag pumps (back pumped by rotary vane pumps), ion getter pumps, and titanium sublimation pumps with a base pressure of 10^{-8} pa or better. The entire apparatus is mounted on a frame made of aluminium profiles borne by pendulum air dampers for vibration isolation. All chambers are connected, and samples, tips or evaporators can be transferred in UHV using magnetic motion drives.

4.2 Preparation chambers

The preparation chambers of both apparatuses may be used for storage and preparation of samples and tips. The available tools in the preparation chamber of the RT-STM are sputter gun (for sample cleaning), mass spectrometer, quartz microbalance, heating station for samples or tips (temperature $< 1600°$C), and station for molecule evaporation or for resistive heating of silicon samples. At the LT-STM apparatus a Low Energy Electron Diffraction (LEED) is available for sample characterization at RT, also various electron guns are mounted.

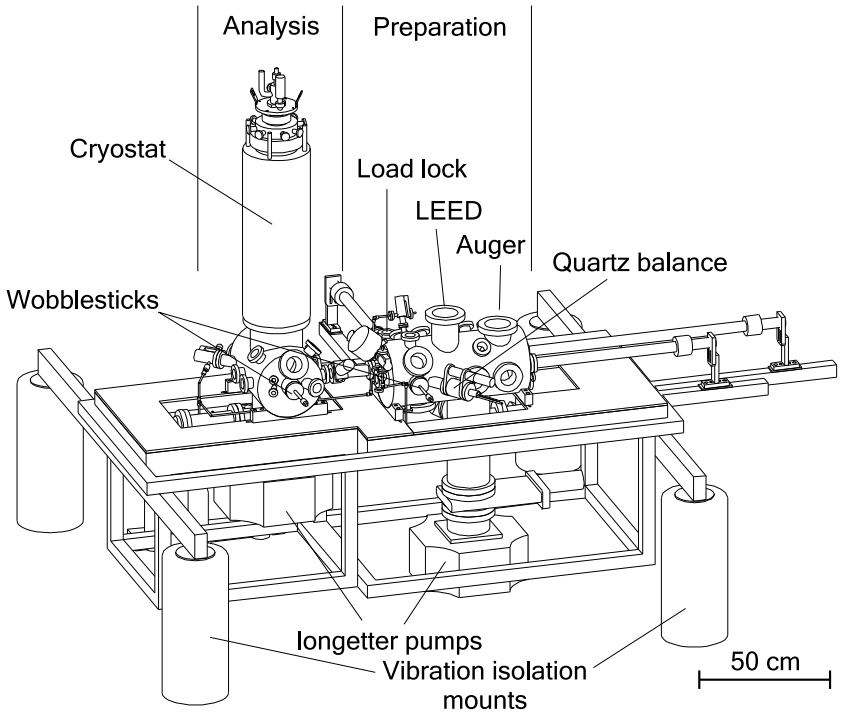

Figure 4.1: Technical drawing of the LT-STM. Adapted from [39].

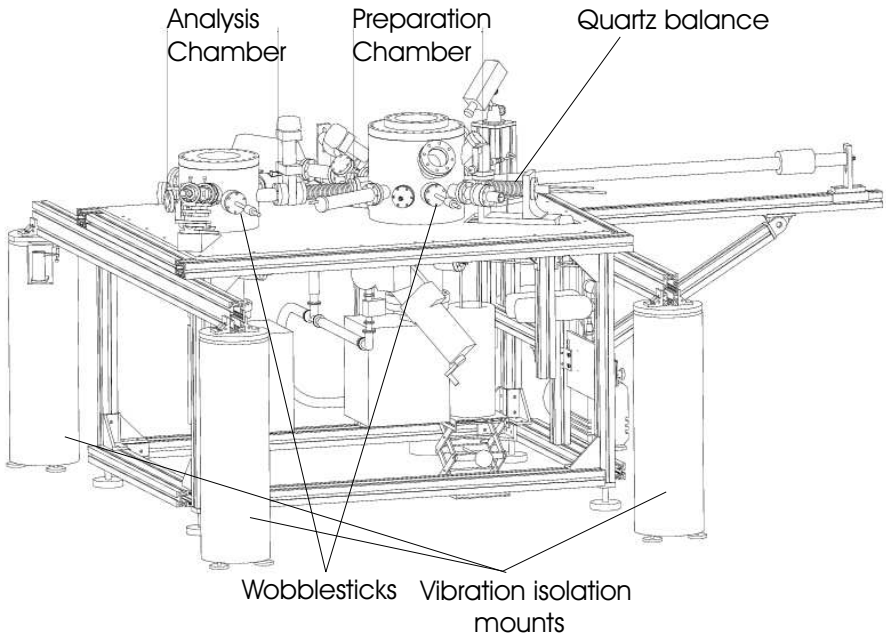

Figure 4.2: Technical drawing of the RT-STM. Adapted from [43].

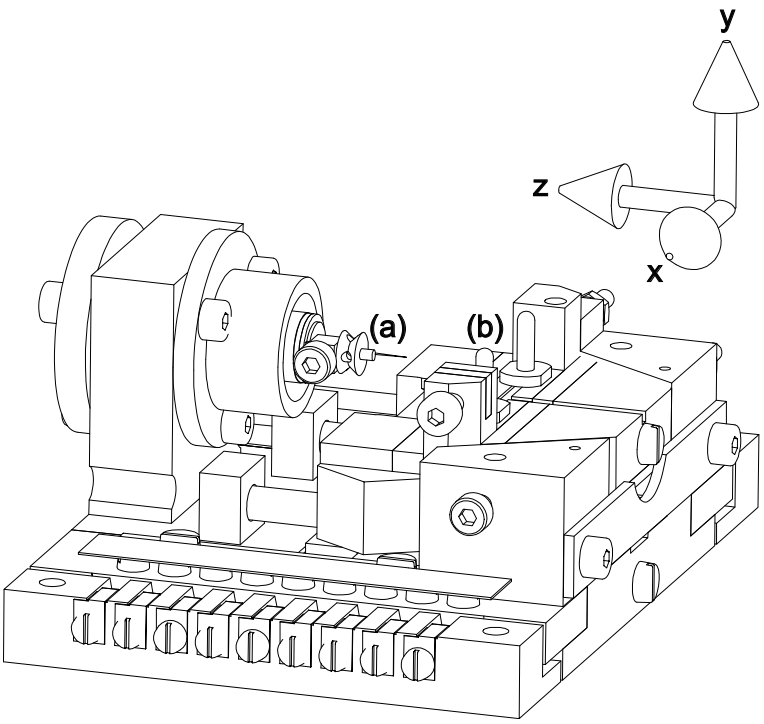

Figure 4.3: Technical drawing of the STM used in the RT- and the LT-STM apparatus. (a) STM tip, (b) Slider for sample mounting. Adapted from [43].

4.3 STM chambers

The STM chamber of the LT-STM is equipped with two cryostats. An outer dewar filled with 15 liters of liquid nitrogen insulates the inner dewar filled with 4 liters of liquid helium or liquid nitrogen. The STM was mounted inside the helium dewar, reaching a miniumum temperature of $\approx$ 7 K. The RT-STM chamber is equipped with an optical setup for recording STM induced light emission.

The STM itself is shown in Fig. 4.3. The sample can be fixed by a screw on the slider by using the wobble stick. The slider is lying on three piezos which move the slider to reach tunneling contact. A Titanium holder for carrying the tip is glued inside the triple segmented scanning piezo. During the experiments only the segmented tube piezo scanner was in use.

4.4 Light emission recording setup

For recording light emission from the tunneling area, a system of lenses made of fused silica is mounted in vacuum. The properties of these optics were especially designed for STM applications as the intensity of the emitted light is in the order of pW or substantially lower. The design was calculated for maximum efficiency in collecting the excited photons from the tunneling region [110]. The optic covers a solid angle of $\approx$ 0.6 sr centered at $\angle = 30^\circ$ with respect to the sample surface. It

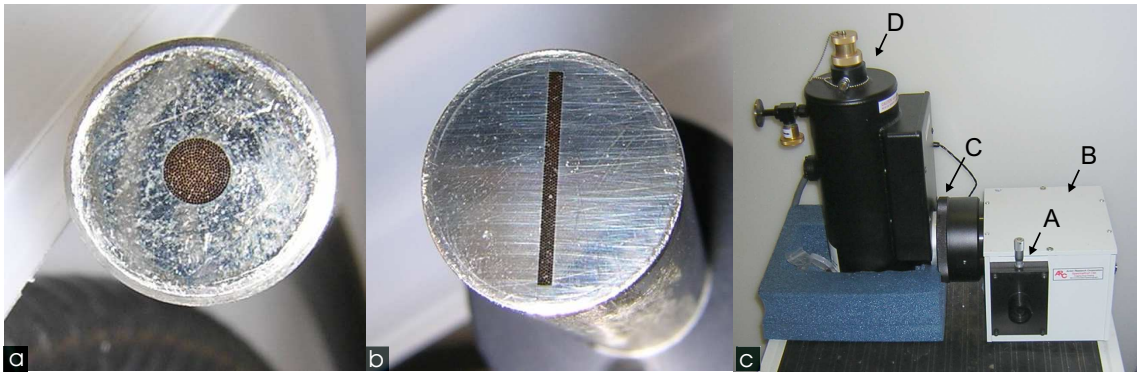

Figure 4.4: (a) At this end of the glass fibre the light from the tunneling region is focused by the in-vacuum lens system. The fibre bundle is arranged circular. (b) At the spectrometer side the fibre bundle is forming an entrance slit. (c) Photograph of spectrometer and CCD camera. The light enters from the entrance slit A the spectrometer B and is being wavelength resolved measured in the CCD camera C. The dewar D is filled with liquid nitrogen for CCD-chip cooling down to -110 $°C$.

consists of three lenses made of fused silica separated by 0.1 mm. The collected light was focused into an optical fibre[1], see Fig. 4.4a. The optical fibre consists of a bunch of multimode fibres bundled at the STM side. The arrangement of the fibres on the spectrometer side form a slit[2], imitating the entrance slit of the following spectrometer[3] (Fig. 4.4b). A blazed grating[4], valid for wavelengths from 200 nm to 750 nm with a blaze wavelength of 300 nm, decomposes the light into wavelength resolved spectra. The photons were recorded with a liquid nitrogen cooled CCD camera[5] with 1340 channels of detection (Fig. 4.4c). The data is stored by a connected computer.

The wavelength axis of the spectrometer was calibrated by a mercury lamp before each cycle of measuring using the Hg-emission lines from 253 nm to 576 nm.

The acquired spectra were weighted by the spectral response function of the complete optical setup to recalculate the deviations caused by instrumentation. CCD quantum efficiency, reflectivity of the grating, optical response of the spectrometer, and transmittance of the fibre are known from the manufacturers and are taken into account to calculate the transmittance of the optical setup. Since the wavelength dependent transmittance of the lens system is not known for the complete spectral range, it is set to a constant value of 0.3 which may cause a systematic error[6]. The

[1]Prinz Optics, Germany, LUV 105 μm.

[2]The dimensions of the slit are 0.5 mm $\times$ 8 mm.

[3]Acton Model: 150.

[4]Acton, 300 g/mm.

[5]Princeton Instruments Spec-10; CCD chip: 1340/400-EB.

[6]The calculated maximum transmittance is 0.46 for blue light [110]. The transmittance is defined here as the ratio of the quantity of the photons entering the optical fibre to the number of photons emitted into a solid angle of 0.6 sr from a point-like light source. Since the optimization was done for visible light, the transmittance is supposed to decrease for UV-light.

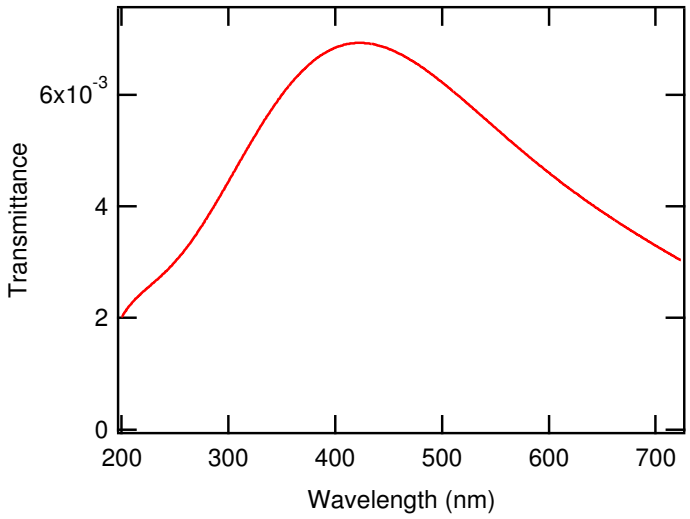

Figure 4.5: Spectral response function of the optical setup (see text).

solid angle of the lens system is included as well. The optic collects only a part of the light which is irradiated from a point-like light source[7] into the half sphere above the sample. The solid angle of the half sphere above the sample is 2π sr and the optic covers a solid angle of ≈0.6 sr; and the inverse ratio of both is taken into account for the overall spectral response of the complete optical setup. It is displayed in Fig. 4.5.

By dividing the measured spectra by the spectral response, the intensity corresponds roughly to the number of emitted photons from the sample per channel of detection.

To transform the measured intensity $[\mathrm{d}I/\mathrm{d}\lambda]$ into an energy equidistant scale $[\mathrm{d}I/\mathrm{d}\hbar\omega]$, the transformation

$$\frac{dI}{d[\hbar\omega]} = \frac{dI}{d\lambda} \cdot \lambda^2$$

was used. The shown spectra are weighed by the transmittance and transformed to an energy equidistant scale if no additional announcement is given.

[7]The light source for STM induced luminescence can be understood as a point-like light source.

Chapter 5

Sample preparation

This chapter gives a brief description of the sample preparation of the transition-metal dichalcogenides (TMDCs) crystals and of the silicon surfaces which were used in the experiments. A new procedure for cleaving of the TMDCs was introduced. Also a tool has been developed to re-cleave the sample in ultra-high vacuum if the initial cleaving fails.
A new silicon sample holder was constructed for better fixation of the sample.

5.1 Cleaving of TMDCs

Cleaving of TMDCs single crystals in ultrahigh vacuum results in clean sample surfaces. Since the interlayer bonding is of a weak van der Waals force, the sample may be cleaved parallel to the layers at this van der Waals gap. The samples were glued onto stainless steel sample holders with a UHV compatible conducting silver glue. A cleaving lever made of aluminium sheet (1 mm thick, see left side of Fig. 5.1) was glued on the top of such a mounted crystal and transferred into the preparation chamber. For cleaving, the wobble stick is usually used and the cleaving lever falls off to the ground of the chamber. Instead of a cleaving lever, a second sample holder was glued on top of the sample, see Fig. 5.1. The second sample holder was utilized as cleaving lever but held with the wobble stick during cleavage. Two sample surfaces are created, and the second sample can be used for further investigations since the "lever" is not lost on the ground of the chamber.

Sometimes it happens that the cleaving was not successful in terms that the crystal surface is covered with partially detached crystal layers. The sample looks like a cleaved crystal but some additional amount of TMDCs layers still appears on the surface which can be seen by eye. Stable conditions for tunneling experiments are maybe hard to adjust due to oscillations of the partially detached layers. If necessary, the crystal can be re-cleaved. A foil of molybdenum was welded under a tip carrier, see Fig. 5.2, and slightly bent to increase mechanical stability as well as sharpened like a blade on the opposite site of the tip carrier. The blade from this tool is placed under the partially detached layers and the layers were in turn removed by lifting the blade. So, it is possible to re-cleave the sample. This procedure was tested for TaS_2 under UHV conditions.

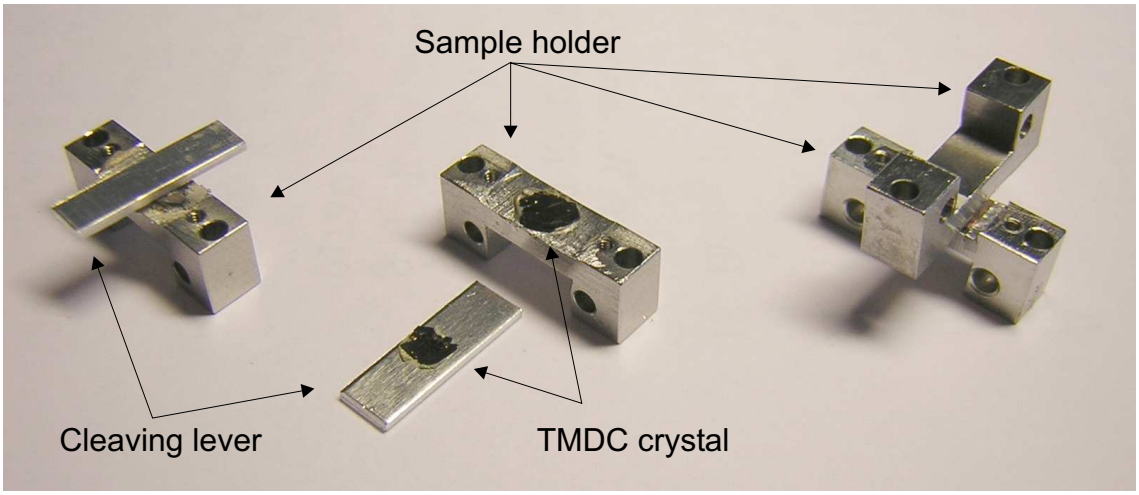

Figure 5.1: On the left side: a sample holder with cleaving lever and TMDC ready for cleaving. Middle: The TMDC glued onto the sample holder and cleaving lever. After cleaving in UHV, the cleaving lever normally falls off to the chamber ground. Right: The conventional cleaving lever is replaced by the second sample holder. After cleaving, the part of TMDC remains on the "lever" can be used for further experiments.

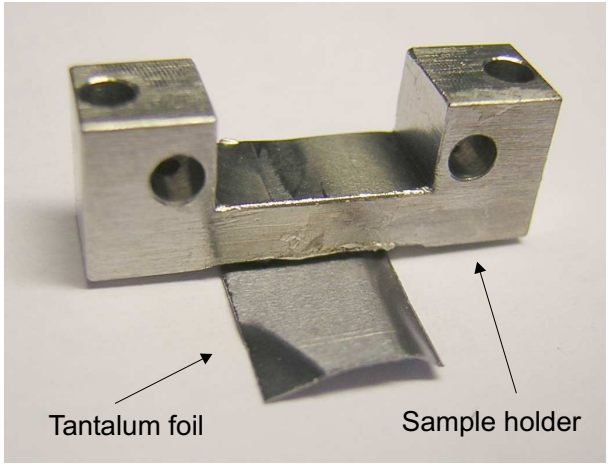

Figure 5.2: The photo shows the tool for the re-cleaving of the TMDCs in case of a bad cleave. The tantalum foil welded under a sample holder works as a blade which removes partially detached crystal layers. The foil was bent to increase mechanical stability and sharpened at the left side.

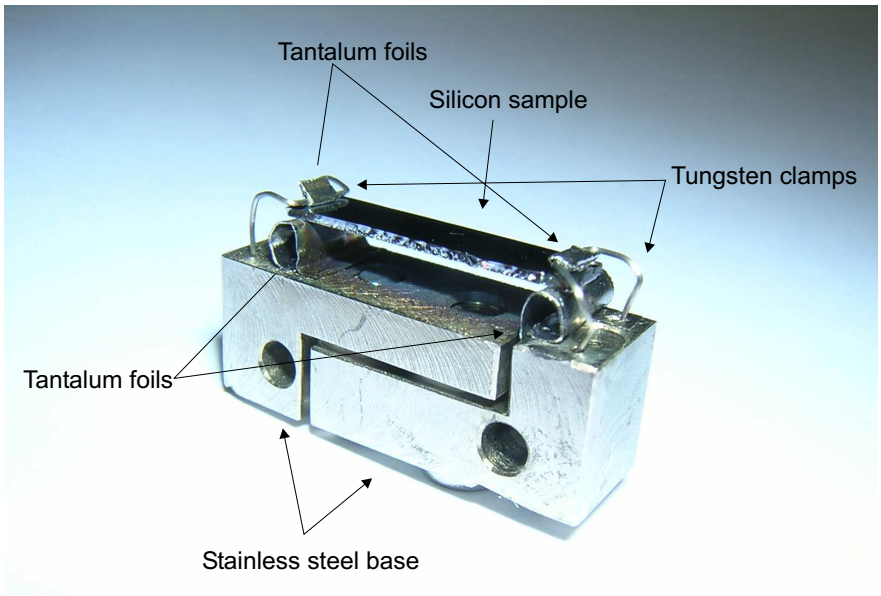

Figure 5.3: Photograph of the silicon sample holder. The silicon sample is clamped between the tantalum covered tungsten wires and bent tantalum foils.

5.2 Silicon samples and preparation

The silicon samples were cut from parts of commercially available Si wafers with various dopant levels and surface orientations. The sample surfaces were prepared by resistive heating in cycles, where sample temperature was monitored by a pyrometer. For the first cycle the sample was degassed at a temperature of 350 °C for several hours till the vacuum pressure remained in the base pressure range of 10^{-8} pa. In the following cycles the samples were heated up to 1200 °C for 10 s. This procedure was repeated between 20 and 30 times. Sample cooling in the last preparation cycle was carried out within 30 s from 1200 °C to 700 °C to establish the surface reconstruction. The surface quality was checked with STM and stopped when the (2×1) on Si(100) or (7×7) reconstruction on Si(111) surface was observed.

5.3 The new Si-sample holder

In the previously used sample holder design, the samples were simply clamped between two sheets of tantalum foil. During the preparation procedure the clamping became sometimes softer and the sample started to vibrate during STM measurements or fell off.

A photograph of the new sample holder is shown in Fig.5.3. The sample is positioned on two small tantalum tubes made of foil to avoid mechanical contact with the stainless steel basis. The clamping was achieved by the two outer tungsten wires (0.25 mm in diameter) covered with Ta foil at the points where mechanical

contact to the Si wafer occurs. On each side of the sample holder two holes (0.3 mm in diameter) were drilled. The tungsten clamps were placed in the holes and fixed under the sample holder with small welded sheets of Ta foil. To place or replace a piece of Si sample the clamps can be bent by a tweezer and the sample can be easily changed. This procedure works even after sample preparation with sample temperatures of 1200 °C since the current for resistive heating (up to ≈4 A) runs only partially through the tungsten clamps.

Comfortable and effective work with this type of sample holder is guaranteed by the fixing properties of the tungsten clamps, which are not affected by the sample heating.

Chapter 6

Silicon

In this chapter the basic properties of silicon are described, including the prominent silicon surface reconstructions: (2×1)-Si(100) and (7×7)-Si(111).

6.1 Basic properties of silicon

The single crystal of silicon has a diamond cubic crystal structure with an octahedron Brillouin zone [111–113] which is shown in Fig. 6.1a. The general definition of distinguished points by letters in the Brillouin zone is also indicated in the figure. The corresponding band structure of this semiconductor is shown in Fig. 6.1b. The numbers notated at the bands in Fig. 6.1b name the bands for addressing specific bands at one point in the Brillouin zone. In general, bands with a prime are valence bands while others are conduction bands[1]. The notation follows Ref. [111]. The maximum of the energetically highest located valence band is at the $\Gamma_{25'}$ point in the middle of the Brillouin zone. The lowest position of the conduction band is at Δ_1. These two points are named valence band edge and conduction band edge and form the indirect bang gap $E_{g,ind}$ of silicon. The size of the band gap is temperature dependent [114] and at room temperature the indirect band gap $E_{g,ind}$ is 1.12 eV [115]. The direct band gap $E_{g,dir}$ is between $\Gamma_{25'}$ and Γ_{15} and has an energy of 3.4 eV [116].

Since the band structure is of great interest for scientific research and technical applications, many experiments were performed to analyze the band structure either with theoretical approaches [117, 119, 120] or experimentally obtained data. Very common experiments are angle resolved photo emission spectroscopy (ARPES) or inverse photo emission spectroscopy (IPES) techniques [121–128]. The advantage of ARPES is that access is given to energy and the k-vector of the band structure. But both have the disadvantage that only either the occupied states (valence bands) or the unoccupied states (conduction bands), respectively, can be explored.

Techniques like electroreflectance [129, 130], wavelength modulated reflectance [131], or ellipsometry [132] give an indirect approach to band structure since the favored transition energies in the Brillouin zone can be explored. These techniques have in common that the samples were irradiated with light, and holes below the

[1] Another notation uses v and c for specifying valence and conduction bands, respectively.

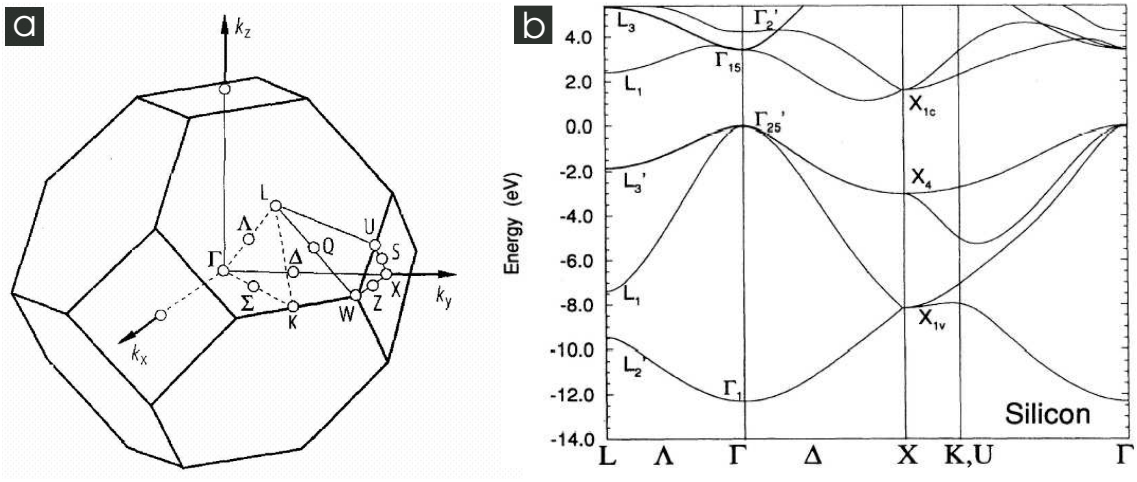

Figure 6.1: (a)Brillouin zone of silicon as shown in Ref. [111]. (b) Calculated silicon band structure, taken from Ref. [117].

valence band edge were generated by photon absorption and electrons entering conduction bands states well above the conduction band edge. Relaxation processes for energy dissipation of these electrons and holes are phonon scattering and photon emission by electron-hole recombination. The preferred radiative electron-hole transitions are direct ones at those points in the Brillouin zone where the bands appear parallel [133].

It will be shown in chapter 7 and chapter 9 that an excitation of the electron-hole system in silicon bulk can be achieved with STM and peaks in the emitted light can be attributed to several direct interband transitions, which are also found using electroreflectance, wavelength modulated reflectance, or ellipsometry techniques.

6.2 Surfaces

The research of surface reconstructions on silicon surfaces has a long history and is still a topic of extensive research. By cleaving a single crystal of silicon, the covalent bonding towards the surface break and a number of half filled electron orbitals are left on the surface. On the Si(100) surface, dimers are created to reduce the number of half filled orbital. These dimers are forming dimer lines running along the $[1\bar{1}0]$ direction [134, 135]. Fig. 6.2 a shows a room temperature STM image of the Si(100) surface with symmetric dimers and buckled dimers. Calculations of the surface band structure show dangling-bond bands (π, π^*) in the bulk band gap region. Dimer-bond (ρ), anti-bonding dimer bond (ρ^*), back-bond (B), and anti-back-bond (B^*) bands are predicted [136–139] and photoemission and scanning tunneling spectroscopy studies support this scenario [126, 140–143]. Nevertheless, the (2×1)-Si(100) surface remains to be a really semiconducting one since filled and empty surface state bands are separated by a band gap.

The second famous surface reconstruction on silicon is the (7×7) on Si(111), first discovered by LEED in 1959 [144]. The atomic arrangement within the surface

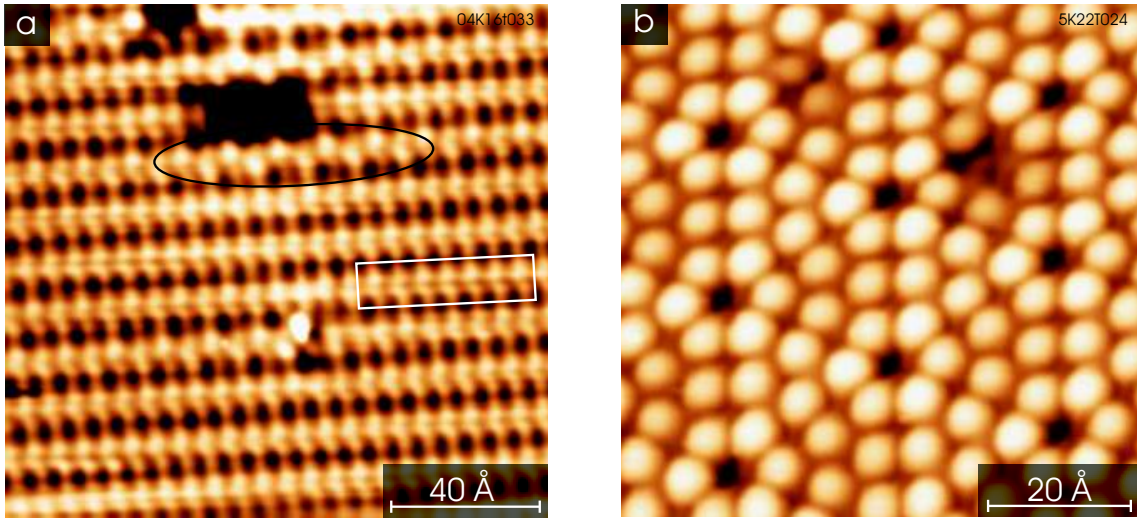

Figure 6.2: (a) STM topography (-2.5 V; 347 pA) of (2×1)–Si(100) surface. Dimer lines are formed of symmetric Dimers and buckled dimers (inside white rectangle and black ellipse, respectively). (b) STM image (-1.9 V; 435 pA) exhibit the (7×7)–Si(111) surface.

unit cell was under debate for at least 30 years, and today the model proposed by Takayanagi *et al.* [145,146] is accepted. A STM image recorded at room temperature is shown in Fig. 6.2b. The electronic structure of the surface remains to be metallic since the number of electrons in the unit cell is uneven and experimental techniques, such as PES, IPES or EELS, support its metallic character [147–154]. Recently, the electrons responsible for the metallic behavior were addressed to be strongly correlated [104, 155], and for sufficiently strong correlation this would give rise to a Mott-Hubbard insulator transition [103].

In summary, it can be concluded that the (2×1)-Si(100) reconstruction is really a semiconducting one since a band gap is present. And the (7×7)-Si(111) is either metallic or close to a Mott insulator, but the surface is not energetically gaped as the (2×1)-Si(100). Those two surfaces are really different in the surface states distribution. In this study, both surfaces were used for STM induced light emission and no significant differences from surface states was found within the recorded spectra, see Chapter 7.

Chapter 7

Ultraviolet light emission from Si in a scanning tunneling microscope

The text from this Chapter has also been published with this title in *Physical Review Letters* **99**, 246103 (2007)[1]. Richard Berndt and Mikhail I. Vexler are the co-authors. Theoretical calculations were performed by Mikhail I. Vexler.

7.1 Abstract

Ultraviolet and visible radiation is observed from the contacts of a scanning tunneling microscope with Si(100) and (111) wafers. This luminescence relies on the presence of hot electrons in silicon, which are supplied, at positive bias on n- and p-type samples, through the injection from the tip, or, at negative bias on p-samples, by Zener tunneling. Measured spectra reveal a contribution of direct optical transitions in Si bulk. The necessary holes well below the valence band edge are injected from the tip or generated by Auger processes.

7.2 Introduction

The tip of a scanning tunneling microscope (STM) can be used to locally inject electrons or holes into a sample with atomic-scale precision and to excite the emission of light [3]. This emission has been observed and analysed from metals, adsorbed molecules and semiconductors [64, 79–83, 86]. While on metals the light emission is excited in the tunneling gap region [16], the fairly intense luminescence from direct semiconductors has been shown to occur inside their bulk [79, 80, 83]. Recently, tunneling-induced luminescence from Si(100), an indirect-band material, has been observed and attributed to inelastic transitions between Si dangling bond states and states specific to W tips [13, 14]. Very similar isochromat spectra were reported from n- and p-type material independently of the polarity of the tip-to-sample bias. Besides, the radiation from a STM contact with Si(111) has been reported and related to a localised plasmon which was suggested to arise on this Si surface [15].

[1]The text was structured with additional sub-titles for pleasant reading

Emission from the bulk of Si owing to the diffusing carriers was excluded. On the other hand, luminescence of bulk silicon is a known phenomenon [156, 157], which is currently being used, e.g., in studies of metal-oxide-semiconductor (MOS) devices [9, 10]. A number of theoretical analyses have addressed the role of direct and phonon-assisted processes and of impurities [9, 11, 158, 159].

Here we undertake an experimental investigation into the STM-induced luminescence from n- and p-type Si. For the first time, detailed luminescence spectra are reported. We included both (111) and (100) orientations in our study, in order to vary the Si surface electronic structure, but the data suggests that this structure does not significantly affect the spectra. As will be shown further, our results are consistent with the model of radiative transitions within the bulk Si. In general, the luminescence of a STM contact has much in common with that of planar MOS structures. However, while the luminescence studies in MOS devices are limited to a low bias regime due to the oxide breakdown at elevated electric fields, this problem is less severe in STM experiments. As a result, we can observe the emission of ultraviolet photons with energies exceeding 4 eV.

7.3 Experiment

The experiments were carried out in a custom built STM under ultra high vacuum conditions at ambient temperature [43]. Si samples (B doped p-Si(111), 1.5 Ωcm; P doped n-Si(111), 56.5 Ωcm; P doped n-Si(100), 10 Ωcm; corresponding to dopant densities of 9.7×10^{15}, 7.9×10^{13}, 4.5×10^{14} cm^{-3}, respectively) were prepared by resistive heating. NaOH etched and *in vacuo* heated tungsten tips were used. The photon detection setup was similar to the one reported in Ref. [97]. A solid angle of 0.6 sr centered at $\angle = 30°$ with respect to the surface was detected. Light emission spectra were recorded on clean, reconstructed (7×7) Si(111) and (2×1) Si(100) surfaces. In all cases, they were corrected for the wavelength dependency of the detection sensitivity. The spectra were not noticeably affected by scanning the tip in a constant current mode. Since tip changes or surface damage are conveniently diagnosed during scanning we used this mode for spectroscopy and made sure that tip and surface remained unaltered.

7.4 Results and discussion

Series of luminescence spectra from p-Si(111) recorded at different sample voltages V are presented in Fig. 7.1. For negative V, clear peaks are observed at photon energies $h\nu = 4.5$ eV and 5.4 eV. An additional structure is discernible at $h\nu = 3.4$ eV for $V = -4.5 \ldots -8$ V. For positive V, the peaks at $h\nu = 4.5$ eV and 5.4 eV were observed too, while at $h\nu = 3.4$ eV, enhanced intensity is hardly discernible except for the $V = 6$ V data. Spectra from n-Si (Fig. 7.2) exhibit pronounced peaks at $h\nu = 3.4$ eV and 4.5 eV, but at 5.4 eV the intensity is only weakly perturbed. All the spectra show an intensity increase at low photon energies which is consistent with the luminescence of almost thermalized carriers observed also on Si MOS capacitors [8].

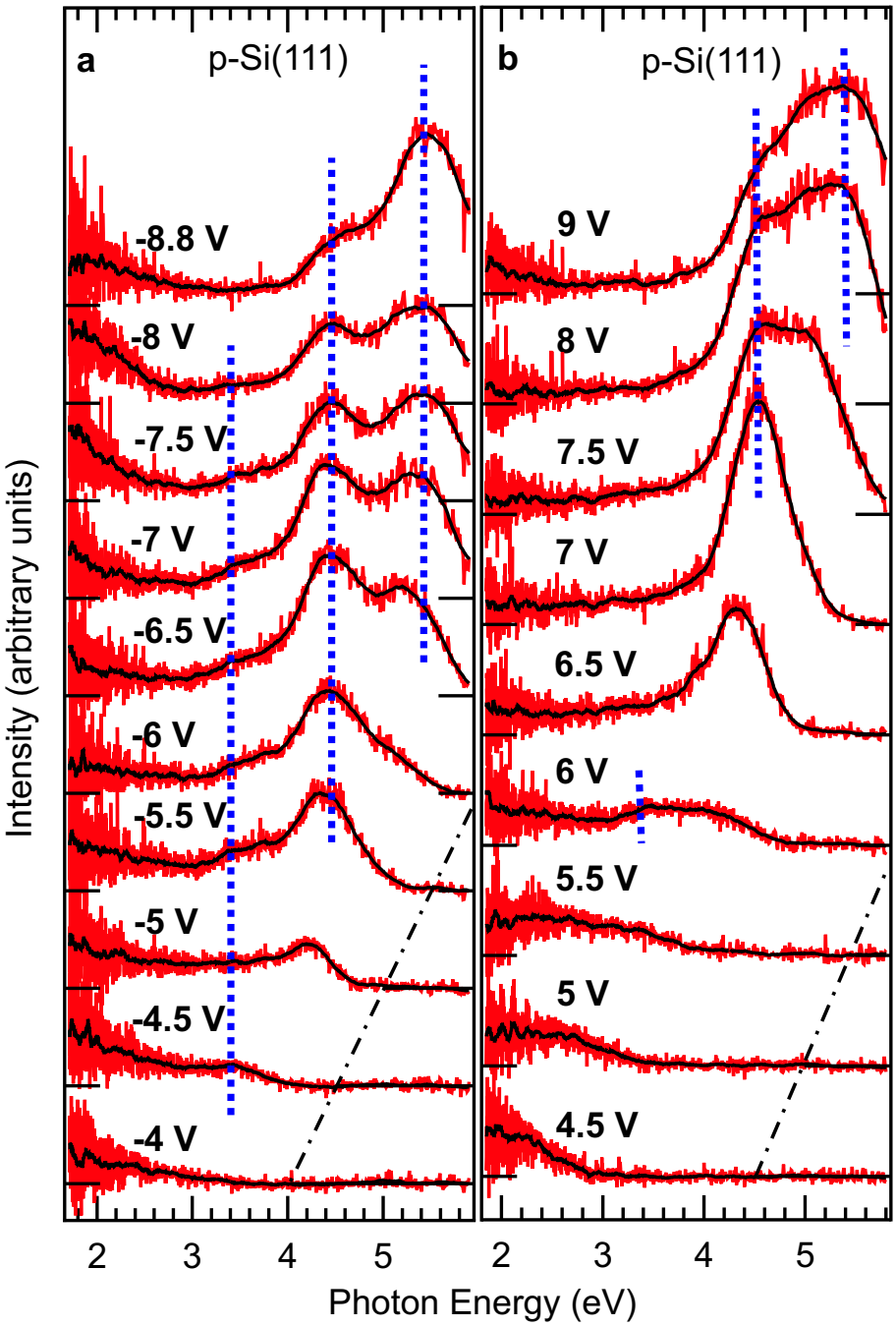

Figure 7.1: Luminescence spectra recorded from p-Si(111) at tunneling current $I = 26.7$ nA for (a) negative and (b) positive sample voltage V. "Noisy" curves represent raw data acquired with 1340 channels, smoother curves are obtained by averaging. Photon energies $h\nu = 3.4$, 4.5 and 5.4 eV are marked with vertical dashed lines. Dash-dotted lines represent the condition $h\nu = eV$.

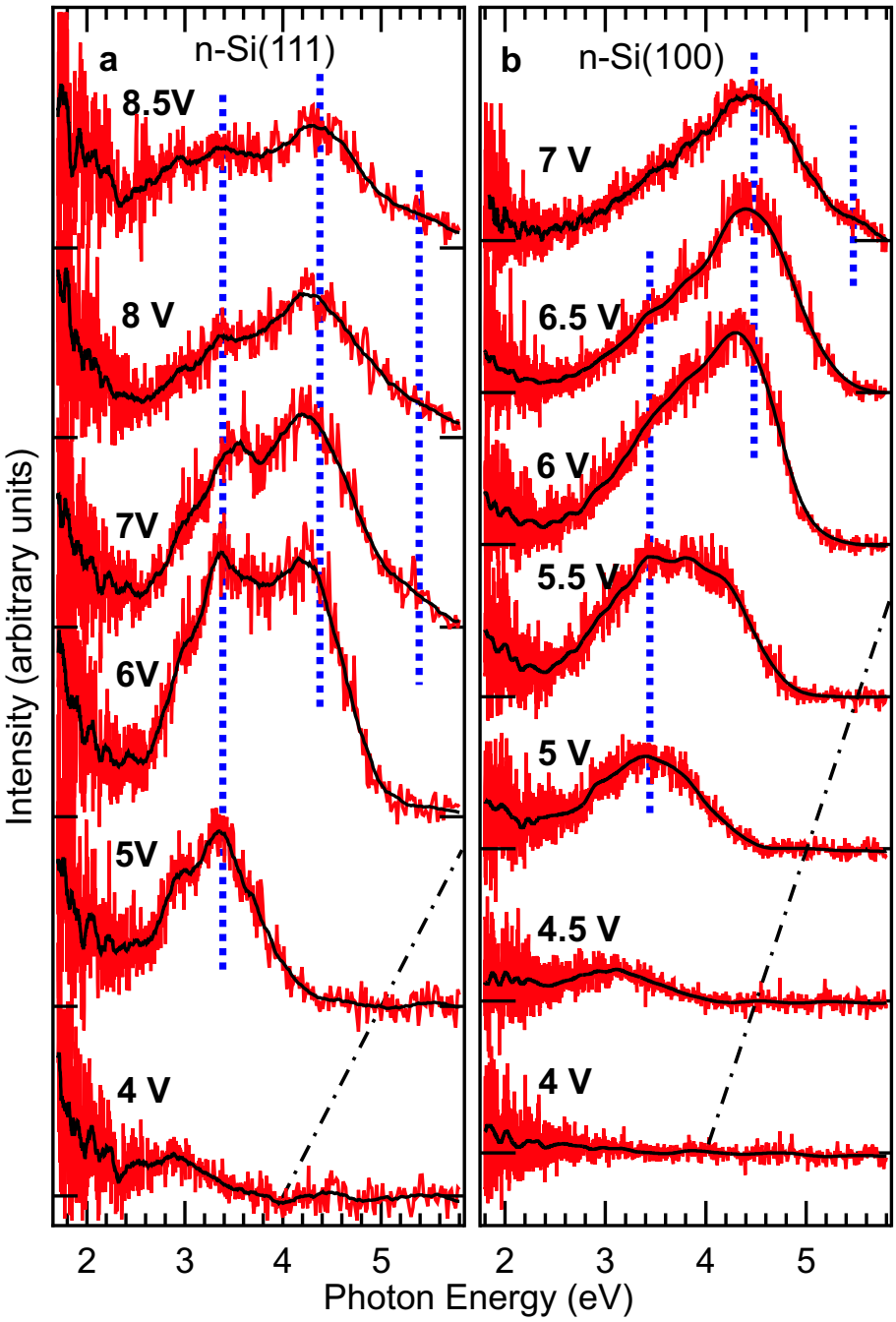

Figure 7.2: Luminescence spectra recorded at positive bias V from (a) n-Si(111) at $I = 9.2$ nA and (b) n-Si(100) at $I = 10.7$ nA. Dashed and dash-dotted lines defined as in Fig. 7.1.

No radiation was detected from the n-Si samples for $V < 0$, unless we previously touched the Si surface with the W tip.

The observed peaks match the energies of direct interband transitions in Si as determined from reflectance and ellipsometry measurements [130, 131, 160]. Three sets of transitions can be identified [114]: (a) $\Gamma_{25'} \to \Gamma_{15}$ and $L_{3'} \to L_1$ at $h\nu \sim 3.4$ eV, (b) $\Gamma_{25'} \to \Gamma_2, \Delta_{5'} \to \Delta_1, X_{4'} \to X_1, \Sigma_{5'} \to \Sigma_1$ at $h\nu \sim 4.5$ eV, and (c) $L_{3'} \to L_3$ at $h\nu \sim 5.4$ eV. Some of these transitions, e.g. $L_{3'} \to L_3$, involve holes with energies much lower than that of the valence band edge E_V.

In this work we did not intend to perform detailed electrical or optical simulations considering the exact geometry of a STM contact. Instead, we restrict ourselves to a qualitative analysis and use models of a one-dimensional (planar) MOS tunnel structure. Such models allow to estimate the band bending in the semiconductor, the electron and hole components of the tunneling current through the insulator, the Zener current within silicon etc. and thus capture the essential physics. Note that the hole tunneling in a vacuum gap, oppositely to an oxide, occurs through the upper barrier formed by this gap, as there is no "insulator valence band". Like in a regular MOS structure, the charge states of depletion, inversion and accumulation can be supported in a STM contact. An important difference between the planar and real topologies is that the depletion layer width for the given band bending value will be smaller than in planar case as can be verified from a calculation for a junction between a semiconductor and a metal sphere. When the sphere radius is large, the flat situation is imitated.

Below we use the energy diagrams of the tip-vacuum-semiconductor system, as if this system were planar, (Figs. 7.3,7.4) to illustrate the processes responsible for light generation.

At positive sample bias, $V > 0$ (Figs. 7.3a,b), electrons (**1**) are injected into Si with energies up to 9 eV above the conduction band edge of the quasineutral area. At such energies, Auger ionization processes are the predominant relaxation mechanism with a quantum yield around one [161, 162]. The probability for the resulting hole $\mathbf{1'_p}$ to be created significantly below E_V is high (e.g., for a 4.5 eV electron, the probability of generating a hole with an energy under $E_V - 2\,\text{eV}$ exceeds 0.2 [7]). A second injected electron **2** can then radiatively recombine with $\mathbf{1'_p}$. These optical processes are localized at the depth of about ten nm in Si [8], so that a large fraction of emitted photons should reach the detector without reabsorption.

The above scenario is valid for both p- and n-type silicon. However, the energy of the injected electron **1** with respect to E_C and, therefore, the threshold for exciting a transition involving a specific conduction band state for a given bias voltage depends on doping (Fig. 7.3). Experimentally, such a variation is indeed observed. Fig. 7.3c displays isochromat spectra for the most intense spectral feature in the photon energy range (4.28 ± 0.15) eV. The observed shift $\Delta = 0.76$ eV between spectra from n- and p-type Si agrees with the difference in bulk Fermi energies. This is strong indication that most of the photons are generated in the bulk material. For hypothetical near-surface transitions, Δ should have reflected the band bending which is rather large and different for n- and p- Si.

At negative sample voltage, as already mentioned, the light was observed only

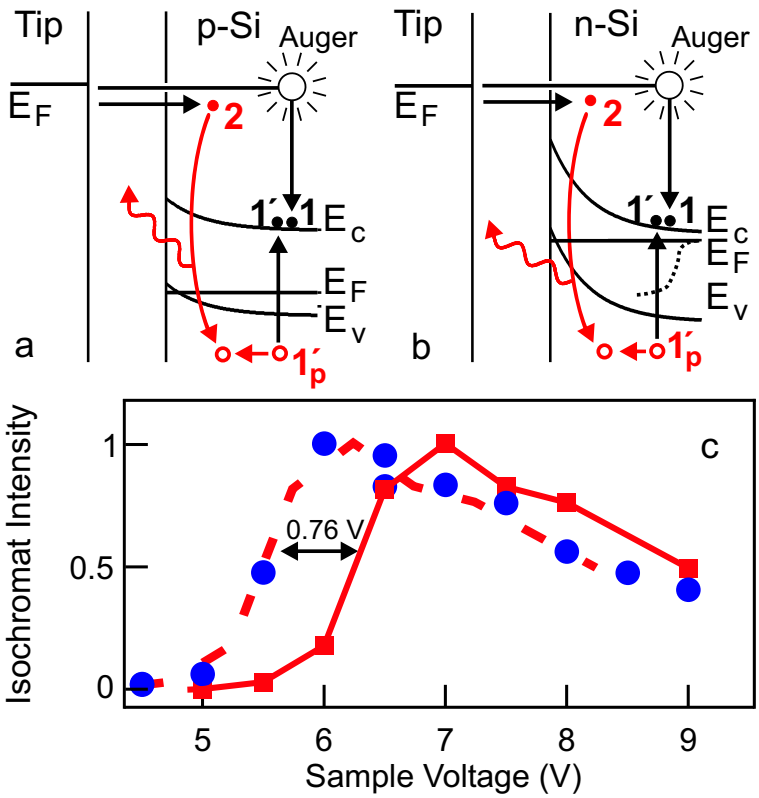

Figure 7.3: Band diagrams and relevant processes for STM-induced light emission at positive substrate bias V. (a) p-Si. Hot electrons **1** and **2** are injected from the tip. Electron **1** undergoes an Auger transition creating an electron $\mathbf{1}'$ and a hot hole $\mathbf{1}'_\mathbf{p}$. Electron **2** radiatively recombines with $\mathbf{1}'_\mathbf{p}$ which may have drifted in the accumulation zone. (b) n-Si. Similar processes occur as in p-Si. Dotted line indicates the position of quasi Fermi level for holes. (c) Isochromat spectra for photon energies (4.28 ± 0.15) eV from n- (dots) and p- (squares) Si(111). Spectra have been scaled to identical maximum intensity. The solid line connects p-Si(111) data points. A shift $\Delta = 0.76$ eV yields the dashed line.

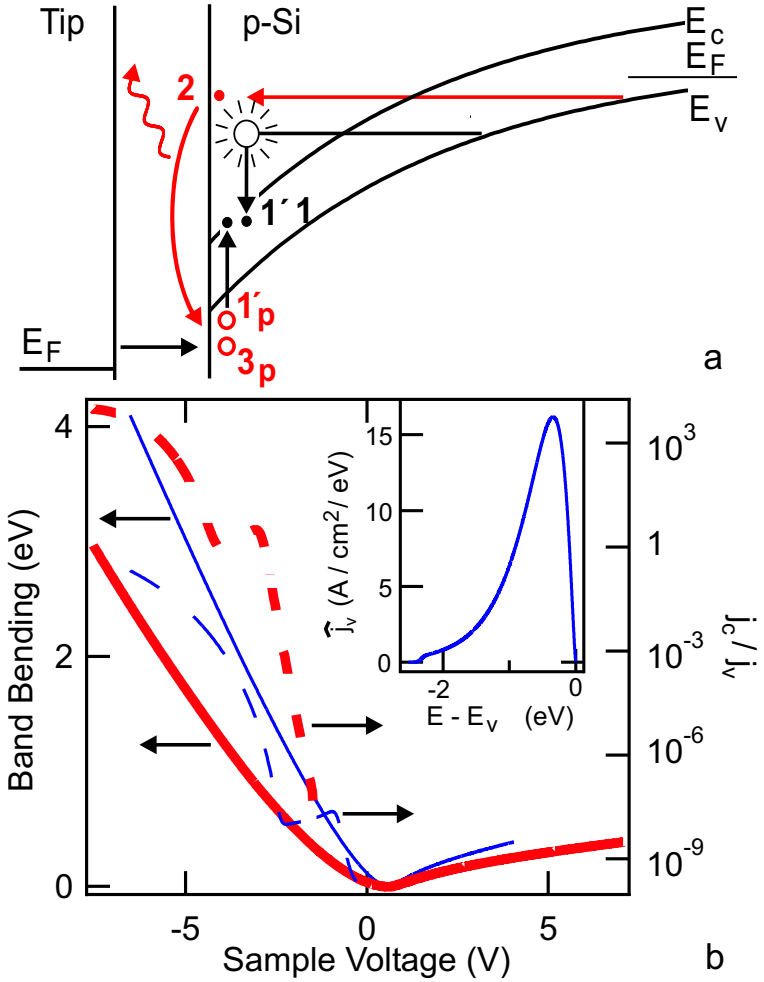

Figure 7.4: (a) Band diagram and relevant processes for STM-induced light emission from p-Si at negative bias V. Zener tunneling of electrons **1** and **2** occurs. **1** undergoes an Auger transition creating $\mathbf{1}'$ and $\mathbf{1}'_\mathbf{p}$. **2** radiatively recombines either with $\mathbf{1}'_\mathbf{p}$ or with a hot hole $\mathbf{3_p}$, which tunneled from the tip. (b) Band bending for a planar W-vacuum-Si junction along with the ratio j_c/j_v of tunnel components. Calculations were performed for 1 nm (thin curves) and 2 nm (thick) vacuum gap; dopant concentration is $5 \cdot 10^{18}$ cm^{-3}. An energy distribution of the valence band current (inset, $V = -6.5$ V) shows that hole tunneling some eV below E_V is significant.

for p-Si. The absence of luminescence from n-Si at $V < 0$ is easy to understand. The junction operates at forward bias and the band bending is small. No hot electrons appear in the conduction band of silicon in such a case.

The origin of luminescence from p-Si at $V < 0$ can be explained as follows (Fig. 7.4a,b). The junction is reversely biased and strong band bending occurs. As a consequence, Zener tunneling of electrons from the valence band is possible; subsequently, these electrons are moving within the conduction band gaining high energy. Thus hot electrons **2** and, via Auger transitions, hot holes $\mathbf{1'_p}$ are generated. An alternative process leading to the appearance of hot holes is tunneling between the tip and the states in Si underneath the valence band edge ($\mathbf{3_p}$ in Fig. 7.4a, inset to Fig. 7.4b). The final step is radiative recombination of **2** with $\mathbf{1'_p}$ or with $\mathbf{3_p}$.

There might be doubts about the validity of a Zener transport mechanism in our relatively low doped p-silicon samples. Indeed, this mechanism is known from the textbooks to come into the play at fairly high fields for which high dopant concentrations, say 10^{18}-10^{19} cm^{-3}, are required. However, one should not forget that these values refer to the planar geometry, and the same fields in the depleted region of a semiconductor may be attained in a STM contact topology even for much more moderate doping levels.

Fig. 7.4b (dashed lines) displays the calculated ratio of conduction and valence band current densities j_c/j_v, where the acceptor concentration was taken larger than in our samples, to roughly compensate for the geometry effect. Qualitatively, at high negative bias, most hot holes are found to be provided by Zener tunneling followed by Auger processes, while hole injection from the tip becomes more significant for lower voltages. Note also that for a positive bias $V > 0$, Fig. 7.3, the role of valence band tunneling in supplying hot holes is always minor, since $j_c \gg j_v$.

It is not useless to mention that ordinary MOS structures on highly doped p-Si emit no light for $V < 0$, although Zener tunneling certainly occurs there. This may be due to the intense non-radiative scattering of hot electrons on defects in the presence of a large impurity concentration. In a STM contact, due to the difference in a topology, less highly doped samples can be used, which favors the observation of luminescence.

7.5 Conclusion

In summary, we have reported ultraviolet and visible light from Si(100) and (111) surfaces in a scanning tunneling microscope. While electron injection causes luminescence from n- and p-type samples, no emission is detected at negative sample bias from n-Si in contrast to previous reports. We have presented the first detailed luminescence spectra revealing a great contribution of direct transitions of hot electrons and holes. The luminescence from p-Si at reverse bias involves Zener tunneling and injection of holes well below the valence band edge.

Our results, in particular the similarity of the data from (100) and (111) surfaces, the spectral features observed, and the polarity dependence of the emission are not consistent with the interpretation of Si light emission in terms of localised plasmons [15]. They also are at variance with the interpretation of Refs. [13, 14] in terms of

an inelastic transition between a specific W tip state and Si dangling bond states. It is important to note, however, that the dopant density of the Si samples used in Refs. [13, 14] was substantially higher than in our present work.

We thank P. Johansson, University of Örebro, for many discussions and for calculations of the electromagnetic response of a tunneling gap between a W tip and a Si surface. One of the authors (MIV) thanks the A. von Humboldt foundation for a support of his stay at the TU Braunschweig where part of this work has been done.

Chapter 8

Efficiency of light and ultraviolet emission from silicon

8.1 Introduction

The efficiency of the light emission process is studied in this chapter which is an addendum to the previous. This part is excluded from the previous chapter to keep the form as published.

The efficiency of a light emission process contains information about the underlying processes itself; and in this case some characteristics of the efficiency are found which are in agreement with the suggested model of photon excitation in the previous chapter.

8.2 Experimental

From the measured spectra, the efficiency of the light emission process can be estimated. For that, the quantity of the emitted photons is estimated from the spectra as discussed in Chapter 4.4. Here, the external quantum efficiency is calculated. It is defined as the ratio of emitted photons per tunneling electron. Here, the photon reabsorption and (total) reflection effects inside the silicon bulk are not taken into account. And the number of tunneling electrons is used, and multiplication of carriers inside the semiconductor, due to Auger processes, is ignored[1]. The efficiency for voltages lower than 3 V could not be estimated from the recorded spectra since, for the chosen tunneling currents and the exposure times of the CCD camera, the limit of detection is reached.

8.3 External quantum efficiency and silicon surface orientations

In this section the external quantum efficiency is analyzed under the aspect of influence of surface orientations. For that the n-type silicon samples (2×1)-Si(111) and

[1]The number of tunneling electrons is calculated from the measured tunneling current.

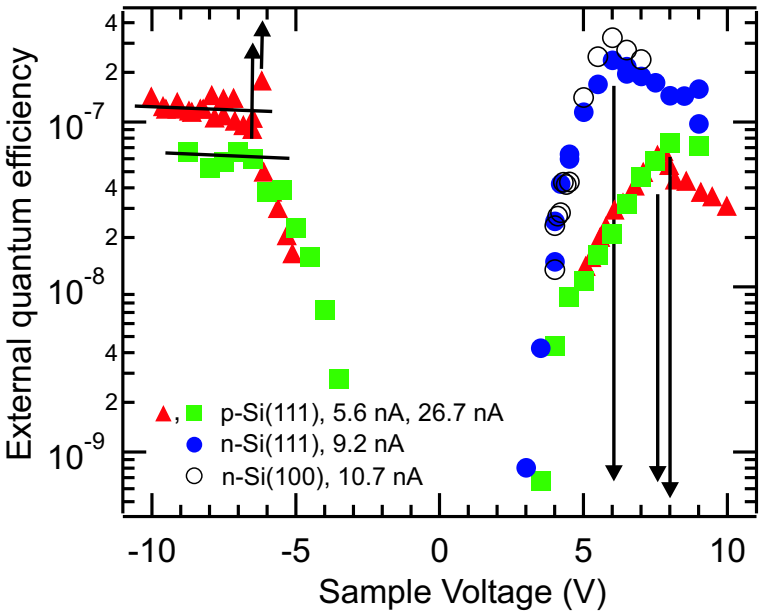

Figure 8.1: Quantum efficiency of the emitted light from different silicon surfaces and doping types. The arrows in the figure indicate the sample voltage at which a maximum in efficiency or a plateau-like level in efficiency is reached. The solid lines mark two different plateau-like levels. Each series of spectra was recorded in one run.

(7×7)-Si(100) are taken into account.

Since the (2×1)-Si(111) and (7×7)-Si(100) samples are similar in doping (7.9×10^{13} and 4.5×10^{14} cm^{-3}, respectively) the Fermi levels are located close to each other at 0.7 - 0.8 eV above the valence band edge. An electron which tunnels into the (2×1)-Si(111) at a certain applied voltage V_x has the same energy with respect to the valence band edge as an electron being injected in the (7×7)-Si(100) sample for the same applied voltage[2] V_x.

The external quantum efficiencies of the n-Si samples are displayed in Fig. 8.1. Data points from n-Si(111) and n-Si(100) are represented by filled and open circles, respectively. Both curves reach a maximum at ≈ 6 V bias voltage and both exhibit a similar run of the curves. Here, no significant differences in the external quantum efficiency are found which can be attributed to surface state effects. The finding is also in agreement with the expectation from the presented model, where the light emission is claimed to depend only on the energy of the tunneling electron into the semiconductor.

[2]This argumentation implies that the surface states have no significant influence on the band banding. Such an influence could not be excluded in principle, but the behavior of band bending for applied biases, as were used here under STM tunneling junction, is not explored to my knowledge.

8.4 Polarity effects on the external quantum efficiency

The presented model for photon excitation suggests that for positive sample bias the efficiency is independent of the tunneling current, while for opposite polarity the light emission properties are depending on the interplay of band bending, Zener tunneling, and hole tunneling. In the latter case, the band bending is current depending[3] and a change of band bending will affect the Zener tunneling processes and hole tunneling as well. One could expect to find a different behavior in the efficiency at positive and negative sample bias due to the current depending physical processes which are considered in the model.

Two data sets from p-Si(111) over a wide range of an applied bias with two different tunneling currents of 5.6 nA and 26.7 nA are displayed in Fig. 8.1, represented by triangles, and squares, respectively. The efficiencies of the p-Si(111) at positive sample voltages reaches a maximum at ≈ 8 V, and the values of the maximum efficiency are found to be close to each other at $8 \cdot 10^{-8}$ photons/tunneled electron and $6 \cdot 10^{-8}$ photons/tunneled electron, respectively. For voltages between 4 V and 8 V the quantum efficiencies of the two data sets of p-Si(111) appear in a remarkable similar behavior. This confirms the presented model where the efficiency for this polarity depends only on the energy of the injected electron. For biases higher than 8 V additional effects which are current depending may play a role[4]. At negative sample voltage, no clear maximum is found in the external quantum efficiency. Instead, two plateau-like levels at $6 \cdot 10^{-8}$ photons/tunneled electron and $1 \cdot 10^{-7}$ photons/tunneled electron are reached between -6 V and -7 V sample voltage.

If one compares the characteristics of the p-Si(111) for positive and negative sample voltages, three differences can be seen. First, the plateau-like levels at the negative bias are reached 1 to 2 Volts earlier than the maximum in efficiency at the positive sample bias. Second, the efficiency reaches more or less similar maxima at positive sample voltage but different plateau levels at negative voltage. And third, the efficiencies for negative sample biases exhibit no clear trend to downsize for an increasing of the applied voltage.

At negative sample voltage the p-Si(111) is driven under reverse conditions and the presented model suggests that the efficiency is influenced by the interplay of band bending, Zener tunneling, and hole tunneling, which may result in a modified characteristic of the external quantum efficiency for negative sample voltages in comparison to positive Voltages. And indeed, those differences were found. This analysis shows that the interpretation of the presented data of external quantum efficiency is in agreement with the presented model. For more quantitative argumentation theoretical investigations are required.

[3] STM experiments which studied the electronic states at semiconductor surfaces by scanning tunneling spectroscopy observed an influence in band bending upon a change of the tunneling current, see e. g. Ref. [143, 163].

[4] See section 10.3.

8.5 Conclusion

The external quantum efficiencies of light emission from different silicon samples were analyzed. First, the influence in the efficiency of surface orientations was analyzed. The efficiencies of the (2×1)-Si(100) and (7×7)-Si(111) [both were n-type Si] are compared and no effects related to the different surface orientations were found. Second, the external quantum efficiency of p-Si(111) was studied for two different tunneling currents. It was shown that the efficiencies at positive sample voltage are independent of the tunneling current over a wide range of voltage, while the efficiencies at negative sample voltage offer a current dependance. But most important, these findings are in agreement with the proposed model for light emission from silicon samples in Chapter 7.

Chapter 9

C_{60} on n-Si(100)

It has been shown in Chapter 7 that light emission from STM is a powerful tool to explore several electronic states of silicon by recording the STM induced luminescence, and maybe silicon has the potential to act as a promising template for light emission resulting from adsorbates like molecules. A STM induced light emission experiment on silicon with adsorbed molecules was performed. The molecule which is chosen for the experiment is the fullerene C_{60}. This molecule has the disadvantage that it is not a dye molecule, but the sample system C_{60} on Si(100) is well explored (as described later in this text). It was shown that this molecule can be used under high tunneling currents without destroying it [164, 165]. For this experiment the tunneling current was set to 340 nA and, under these extreme tunneling conditions, a modification of the C_{60} layer was induced. But after the surface has altered once, the modified C_{60} structure remained stable and enables spectra recording.

9.1 Introduction

The research dealing with C_{60} molecules on (2×1)-Si(100) has been a topic of extensive scientific research. Several studies explored the nature of individual C_{60} molecules with submonolayer coverage on silicon substrates. From STM investigations, it is known that the C_{60} adsorbs on a (2×1)-Si(100) surface mainly between the dimer rows of the silicon surface reconstruction [166] and appears in STM with a height of 6.78 Å[1] [167]. At this submonolayer C_{60} coverage the intra-molecular structure reveals a number of fine structures [168]. The bonding behavior of C_{60} on Si(100) surfaces is thought to be of a van der Waals type [166–173] and no charge transfer is observed. This weak interaction induces just small changes of the electronic structure of adsorbate and substrate and, indeed, the STM tip was used to move the molecule over the surface [166, 174, 175]. By moving the molecules over the surface with a STM tip, the Si dimers along the travelling path, as well as the C_{60} itself, were not damaged.

The bonding changes if the sample is heated to 670 K into a chemisorption nature [171, 172]. STM investigation on the chemisorbed C_{60}-Si(100) system at

[1]The height of the C_{60} might depend on the chosen tunneling conditions, but the here cited value represents the magnitude of order for C_{60} molecules heights in STM studies.

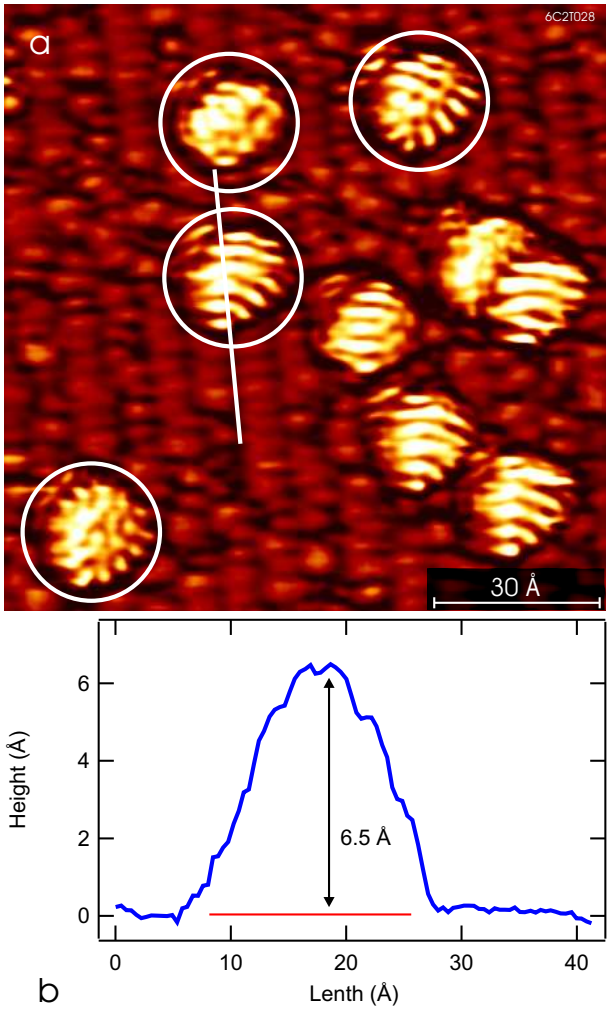

Figure 9.1: (a) STM image (-2.45 V, 3.81 nA) of C_{60} molecules on (2×1)-*n*-Si(100) with submonolayer coverage. The C_{60} molecules were evaporated on the substrate for 5 seconds and several C_{60} molecules were adsorbed on the surface. Some of them are indicated in the circles. The molecules exhibit a rich fine structure and different shapes. A dimer molecule is located at the right side. A profile along the white line is presented in (b). (b) Profile across the centers of a C_{60} molecule on the surface. The height of the C_{60} molecule is 6.5 Å measured from the top of the molecule to the valley between two dimer rows.

submonolayer coverage reveals a change of the C_{60}. The molecules, supposed to be bonded onto the dimer lines, appeared in STM at a height of 4.6 Å while the C_{60} between the dimer rows have a significantly lower height of 2.8 Å [167]. Further annealing of the C_{60} covered Si(100) to 1070 K results in a decomposition of the molecules; and the formation of SiC takes progress [172]. The C_{60} molecules are arranged for submonolayer coverage in an unordered formation. For 3 ML or higher C_{60} coverage a uniform hexagonal structure establishes [176].

9.2 Experimental

For this experiment *n*-Si(100) samples were used which are identical to those used in Chapter 7. Samples were prepared by resistive heating in cycles. The pristine sample was checked with STM and the preparation procedure was stopped when the (2×1) surface reconstruction establishes. On the clean *n*-Si(100) sample surface C_{60} molecules were sublimated from a commercial evaporator [177], driven with a heating current of 1.3 A.

9.3 C_{60} manipulation and stable structures at extreme tunneling conditions

A STM image of the (2×1)-Si(100), covered with several individual molecules, is shown in Fig. 9.1a. The C_{60} molecules are resolved with submolecular resolution and their intramolecular structure reveals a rich fine structure. The shapes of the molecules are similar to those observed in Ref. [168]. The height of the C_{60} molecules, as it appears in STM, is measured from a profile which is taken along the center of a C_{60} molecule, see Fig. 9.1b. The apparent height of the molecule is 6.5 Å. This value is within the same order as reported from Ref. [167]. And it can be concluded that the C_{60} molecules which are van der Waals bonded onto the (2×1)-Si(100) surface appear in STM at a height of ≈6.5 Å.

After evaporation of C_{60} for 45 seconds onto the silicon sample, the STM topographs exhibit an unordered film of C_{60} molecules. Individual molecules on this surface are resolved as bright protrusions in Fig. 9.2a. Following the interpretation of Ref. [176], the C_{60} coverage is between 1 ML and 3 ML.

The manipulation of the C_{60} layer was induced by recording a STM topography at 6 V of applied bias and a 340 nA tunneling current. After this surface scan the STM image shown in Fig. 9.3a was recorded at 4 V and 340 nA tunneling current. It can be seen that a modification of the C_{60} film has taken place and small molecule clusters appear at the surface. After the C_{60} film was manipulated with the STM tip, the (2×1) reconstruction of the silicon surface appears, indicating that the sample surface is still intact, while the C_{60} was removed completely.

Individual molecules were resolved in the STM images. Some of them are marked within the white circles of Fig. 9.3a, indicating that there is a reasonable chance that the molecules were not destroyed during this manipulation procedure. Surprisingly,

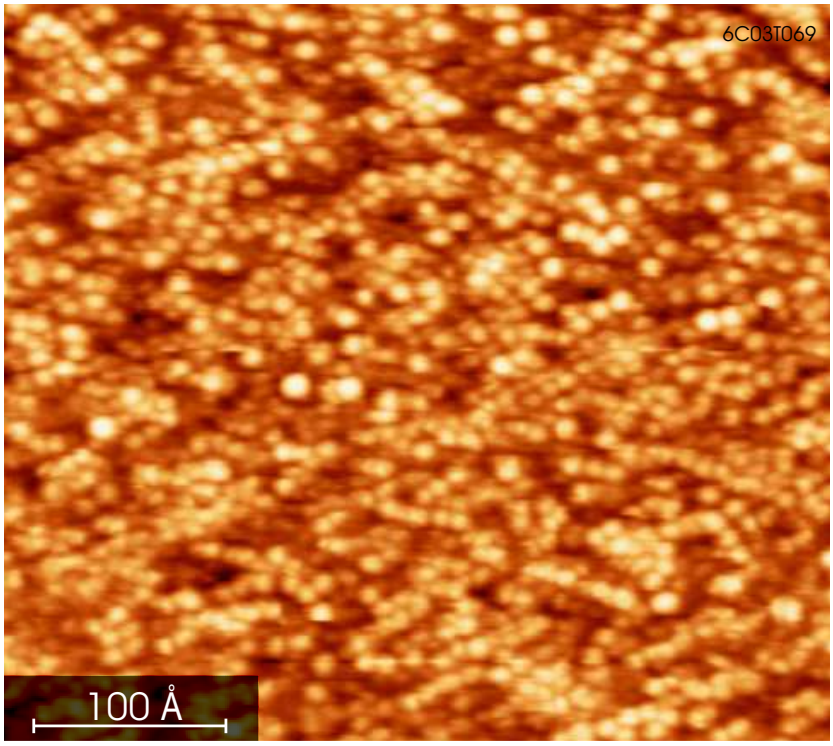

Figure 9.2: (a) STM image of a C_{60} covered (2×1)-n-Si(100) recorded at 4.5 V and 51 nA. Individual molecules are displayed as bright protrusions. Following the interpretation of Ref. [176], the coverage is between 1ML and 3 ML.

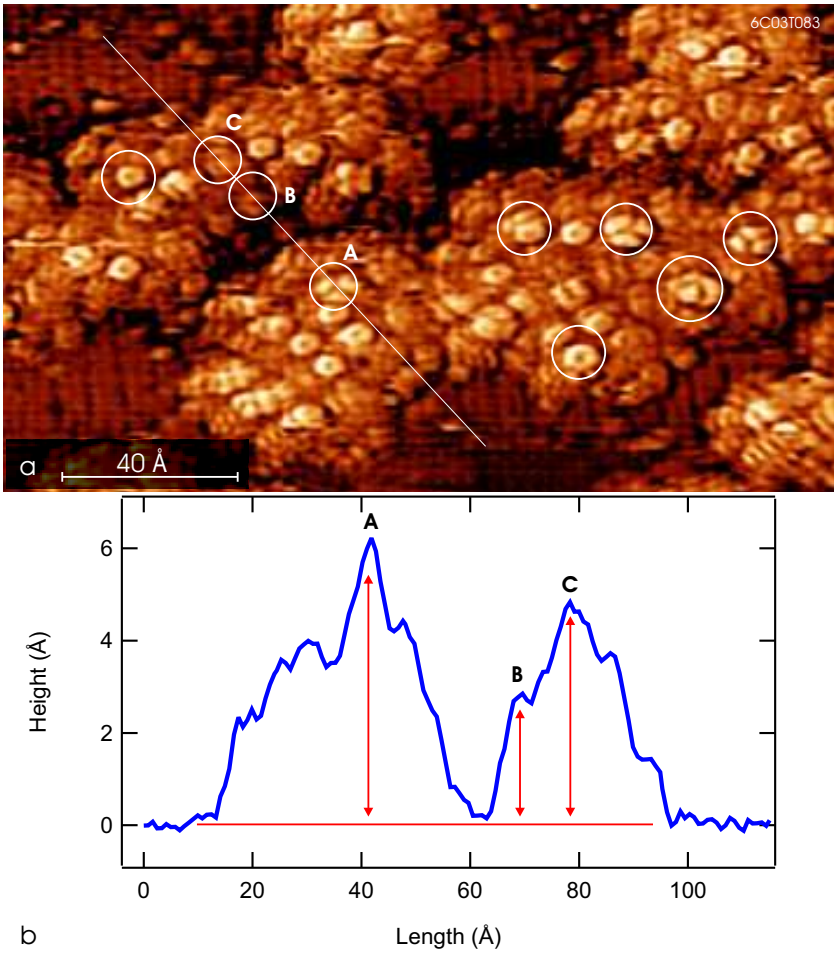

Figure 9.3: (a) STM image recorded at significant higher tunneling current (4 V; 340 nA). The C_{60} film has changed its shape before. Small clusters of molecules appear with a height ranging from 2.5 Å to 6.1 Å. Individual C_{60} molecules were resolved, as indicated in the white circles. In between the molecules' clusters, the dimer rows of the (2×1) surface reconstruction are visible. Along the thin white line a profile is extracted from the image. The profile crosses several centers of molecules indicated in the white circles and named by the letters A, B and C. (b) Profile along the C_{60} clusters. The horizontal line represents the base level for measuring the molecules' heights; arrows indicate the heights of individual molecules A, B and C within the C_{60} clusters.

the shape of several molecules has changed[2]. Those appearances of the molecules are known from C_{60} adsorbed on metal surfaces [178] or polymerized C_{60} arrangements on silicon substrates [179].

A profile is recorded along the white line in Fig. 9.3a which crosses the center of three individual molecules, named A, B and C. The profile is displayed in Fig. 9.3b. The flat regions at the beginning and the end of this profile are related to the parts of the clean silicon surface. The level of the silicon surface is also reached between the two molecule clusters. The heights of the two clusters are smaller than one would expect since the maximum heights are below the apparent height of the individual C_{60} molecule in the previous case, see Fig. 9.1b for comparison. The molecules B and C appear substantially reduced in height at 2.8 Å and 4.7 Å, respectively. This shows, first, that the C_{60} clusters are made most likely only of a single monolayer of molecules and, second, that the heights of molecules B and C are in agreement with those of the individual C_{60} molecules which were chemisorbed on (2×1)-Si(100) [167]. This indicates that the bonding status of several molecules has changed into a chemisorbed type.

The molecule A has the largest height of 6.2 Å within the chosen set of molecules. This value is close to the height of individual van der Waals bonded C_{60} molecules on the (2×1)-Si(100) surface as shown in Fig. 9.1b. This can be interpreted in terms, that the molecule A is still van der Waals bonded within a C_{60} cluster. The fact that the appearance of the molecule is not similar to those which are van der Waals bonded, see Fig.9.1a, may indicate that this C_{60} molecule is not bonded to the silicon surface.

A substantially stronger bonding of the molecules may also explain the stable tunneling conditions after the manipulation with the STM. The clusters' appearance, as seen in Fig. 9.2b, remained stable after it has changed once. During manipulation the amount of C_{60} on the surface seems to be reduced. The missing molecules are supposed to adhere on the STM tip.

In summary, the STM tip was used for manipulation of the C_{60} layer. After manipulation clusters made of individual molecules are found on the surface. The reduced heights of the C_{60} indicate a change in the bonding status with the surface from a van der Waals type into a chemisorbed one.

After the surface has altered once, no further changes are observed, and optical spectra recording at such high currents under stable tunneling conditions was achieved.

[2]See Fig. 9.1a for comparison.

Chapter 10

Multiple peaks light emission spectra from C_{60} covered n-Si(100)

10.1 Introduction

The light emission from the previously described partially C_{60} covered n-Si(100) surface was detected. In order to increase the intensity and to detect photons resulting from C_{60} excitations, the tunneling current was increased to 340 nA. The signal to noise ratio of the spectra has improved as expected. The emitted spectra are still dominated by the silicon bulk radiation. Several c-v transitions which were unresolved in the presented spectra in Chapter 7 are now resolved. The c-v transitions are identified by comparing the measured transition energies with the known c-v transition energies from literature. Several studies about this transitions in silicon bulk were performed at temperatures ranging from 4 K to 1000 K. Reviews about the transition energies can be found in Refs. [130,180]. In Ref. [180] the dependency on temperature was studied. The c-v transition energies increase with temperature and the changes are in order of 0.1 eV or more over a temperature range of 800 K. Therefore, only studies performed at RT are taken into account for identifying the c-v transitions by their energies.

The recorded spectra from the C_{60}-Si(100) sample are rich in peaks and two additional series of peaks are found in the photon energy which range from 3.3 eV to 4.0 eV and 4.1 eV to 4.7 eV and which could be not identified by the known c-v transitions in silicon bulk. These remaining transition energies are compared with known excitations from C_{60} on silicon, but the energies reported in the literature did not match and no evidence of radiation resulting from the molecules are given in the spectra.

A n-Si(100) sample was used for this experiment which was driven under the reverse current direction. Band bending is enabled and a potential well is created within the upward bent bands located at the surface. A series of quantum well states named hole-subbands (HSBs) is induced in this potential [17,186] and which is providing extra states for radiative transitions. The two series of peaks are attributed tentatively to direct optical transitions into these quantum well states.

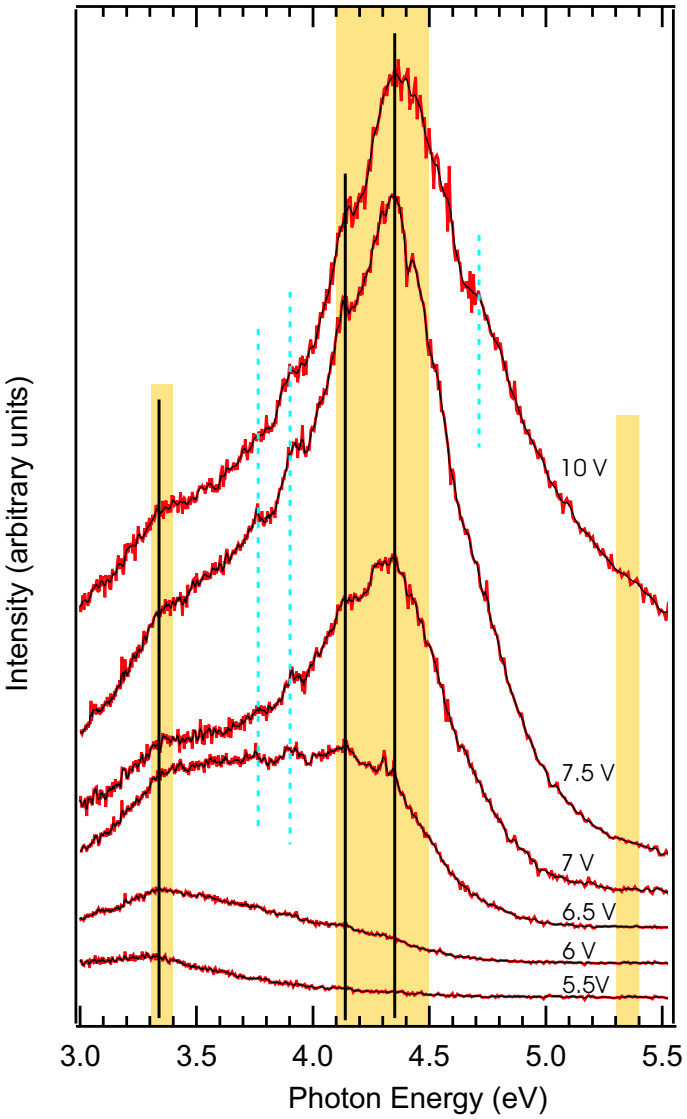

Figure 10.1: Series of light emission spectra recorded at 340 nA. The applied sample voltages are indicated in the figure. Black curves are obtained by averaging. See text.

Before continuing with spectra analysis, a second notation of the direct c-v transitions which is often used in literature should be introduced, see e.g. [111]. The direct c-v transitions in silicon bulk are assigned with E_n (n=0,1,2). The E_1 transition is subdivided into two transitions named E_1 and E_1',. E_2 consists of three transitions named $E_2(1)$, $E_2(2)$ and $E_2(3)$. For a better overview, the E_n transitions are listed in Table 10.1. In there the E_n transitions are addressed to the specific point in the Brilloiun zone at which the transitions occur. A collection of the transition energies, as reported from several authors from RT investigations, is given there, and the values for the E_n transitions found in this study are shown there as well.

10.2 The E_n transitions

The spectra were recorded at 340 nA tunneling current during scanning and later divided by the optical transfer function and transformed from a wavelength scale into an eV scale as described in section 4.4.

A series of spectra recorded at voltages ranging from 5.5 V to 10 V of applied bias is shown in Fig. 10.1. The E_n transitions in silicon bulk, which result in a peaked structure in the light emission spectra, are expected to occur within three photon energy intervals. Those intervals are indicated as shaded areas in Fig. 10.1. Within these shaded areas three peaks can be seen which are indicated by the vertical solid lines. But six E_n transitions are expected, see Table 10.1. Between 3.3 eV to 3.4 eV photon energy two transitions are expected (E_0' and E_1); and in the photon energy range of 4.1 eV to 4.5 eV three optical transitions ($E_2(1)$, $E_2(2)$, and $E_2(3)$) are known to occur. The E_1' transition between 5.3 eV and 5.4 eV is energetically separated from the other transitions, but the intensity in this photon energy range is still poor. There is interest in improving the signal to noise ratio to identify all E_n transitions.

Three additional peaks which cannot be attributed to silicon c-v transitions are marked by the vertical dashed lines. Those peaks remained more or less constant in photon energy under any changes of the applied bias.

The E_n transitions are assumed to be independent of the bias, and the unknown peaks in the spectra remain at constant photon energies under changes of the voltage. To improve the signal to noise ratio further, the spectra from one series of recording are added. The upper curve of Fig. 10.2 is the sum of nine spectra recorded at 4.5 V, 5 V, 5.5 V, 6 V, 6.5 V, 7 V, 7.5 V, and 10 V (2 $\times$). The lower curve is the sum of a second series of spectra recorded at 4.5 V, 5 V, 5.5 V, 6 V, 6.5 V, and 7 V. The lower curve is several times lower in intensity since the applied biases are significantly lower.

Both spectra exhibit several structures which have to be identified. If one compares the indicated peak positions from the upper and lower spectra of Fig. 10.2, a good matching of the indicated structures is found. The differences are 0.05 eV photon energy or less (See later in this text).

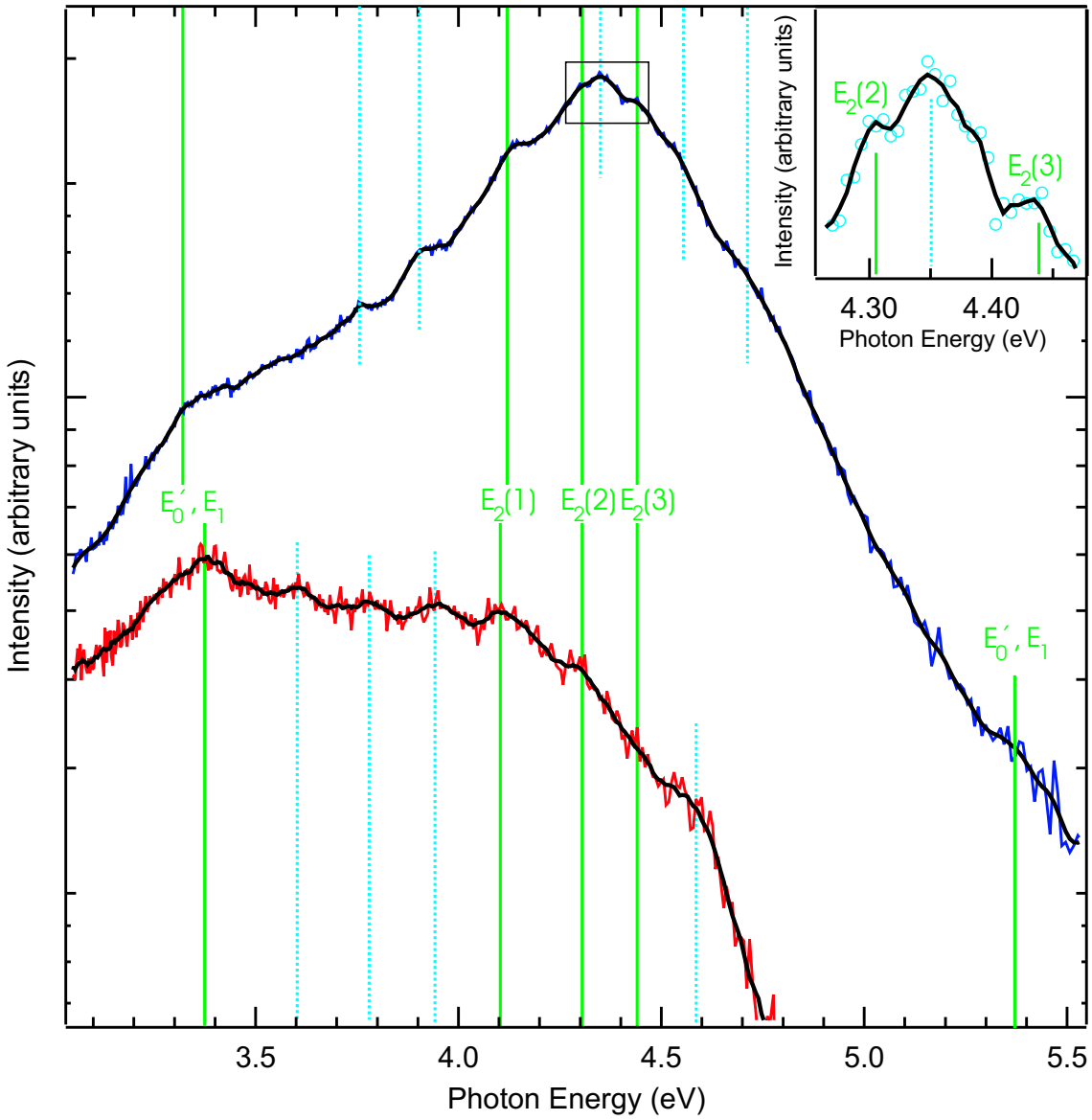

Figure 10.2: Light emission spectra from C_{60}-*n*-Si(100) surface. Each of the spectra is the sum of several spectra recorded at 340 nA and biases ranging from 4.5 V to 10 V. The summation improves the signal to noise ratio so that a variety of peaks in the spectra can be seen and identified. The solid lines indicate the silicon bulk transitions denoted as E_n, see text. The peaks assigned with the dashed lines contribute to two series of transitions into hole-subbands (see text).The inset is a magnification of a small part of the upper curve within the rectangle. The open circles represent data points.

Transition	denoted as	Transition energy at RT (eV)	Measured transition energy (eV)
$L_{3'} \rightarrow L_3$	E'_1	5.30 [181, 182]	5.38 ± 0.05
$\Delta_{5'} \rightarrow \Delta_1$	$E_2(3)$	4.5 [183]	4.44 ± 0.01[1]
$\Sigma_{2'} \rightarrow \Sigma_3$	$E_2(2)$	4.3 [183]	4.31 ± 0.01
$\Gamma_{25'} \rightarrow \Gamma_2$	$E_2(1)$	4.05 ± 0.1 [183]	4.11 ± 0.01
		3.40 [130]	
$\Delta_{3'} \rightarrow \Delta_1$	E_1	3.412 [184]	
		3.36 [185]	
		3.330 [130]	3.35 ± 0.04[2]
$\Gamma_{25'} \rightarrow \Gamma_{15}$	E'_0	3.294 [184]	
		3.281 [185]	

[1] appears only in upper curve of Fig. 10.2

[2] The E_1 and E'_0 are not resolved in the spectra.

Table 10.1: The classification of E_n transitions to specific points in the Brillouin zone follows Ref. [111]. The measured transition energies found for this work are listed in the table as well.

By comparing the known transition energies with the ones indicated in Fig. 10.2, several c-v transitions in silicon bulk, excited by STM, can be identified. The highest peak energy is found at (5.38 ± 0.05) eV. The exact position of this peak is hard to discern since it is located at the fast decreasing shoulder of an another peak. Nevertheless, it can easily be attributed to the $E_{1'}$ transition. This direct c-v transition in known to occur in the Brillouin zone at $L_{3'} \rightarrow L_1$. The corresponding reported transition energy is 5.30 eV from ellipsometry and thermoreflectance measurements at RT [181, 182].

The E_2 transition consists of three direct c-v transitions in the silicon Brillouin zone, labelled $E_2(1)$, $E_2(2)$ and $E_2(3)$, e.g. [182]. The transition energies, as reported for RT investigations, are (4.05 ± 0.1) eV, 4.3 eV and 4.5 eV, respectively [183]. The $E_2(1)$ transition is found here at (4.11 ± 0.01) eV in this study. The $E_2(2)$ and $E_2(3)$ transitions are found at (4.31 ± 0.01) eV and (4.44 ± 0.01) eV, respectively. Note, that the 4.31 eV and 4.44 eV peaks are resolved, as can be seen in the inset of the Fig. 10.2. The errors in intensity[1] are in the order of the size of the open circles which represent data points. The peak energy of 4.31 eV is also found in the lower curve.

It is known that, between 3.3 eV and 3.4 eV photon energy, two direct c-v transitions, namely E'_0 and E_1, exist. The values of transition energies, as reported from different authors, are: E'_0 at 3.330 eV [130], 3.294 eV [184], 3.281 eV [185] and E_1 at 3.40 eV [130], 3.412 eV [184] and 3.36 eV [185]. Later research with ellipsometry, combined with a theoretical approach [182], claimed the transition

[1] Square root of the intensity (counting events per channel of detection) as measured in the raw data.

energies to be at 3.35 eV and 3.40 eV [2]. The two transitions are not resolved in the shown spectra definitely. In the lower curve of Fig. 10.2, a clear peak is at 3.38 eV photon energy, which matches well with reported values for E_1. At this energy a peak is missing in the upper curve. Instead, a kink in intensity is at 3.32 eV photon energy, which matches quite well with reported values for the E_0' transition. Since each spectrum contains only a single peak, it cannot be excluded that this is the same unresolved transition. Therefore, the energy of the peak found in the spectra is set to the averaged value of (3.35 ± 0.04) eV photon energy.

In Summary, the known transition energies which occur in silicon bulk are compared to those measured with STM induced light emission investigations made in this work. The found peak positions match well with the known transition energies and allow one to identify several transitions. The $E_{1'}$ at (5.38 ± 0.05) eV and the energetically narrow spaced "triplet" transition $E_2(1)$, $E_2(2)$ and $E_2(3)$ at (4.11 ± 0.01) eV, (4.31 ± 0.01) and (4.44 ± 0.01) eV, respectively, are successfully resolved.

10.3 Hole-Subbands and light emission

Former research on HSBs, or hole confinement in *n*-Si devices, was done using cyclotron resonance, Shubnikov-de Haas oscillations [18–21], or magnetotunneling [22]. Great advantage was reached in Ref. [186] where these HSBs are directly visualized by ARPES measurement in k-space. Theoretical investigation on this carrier confinement was first done by Stern in Ref. [17]; later several authors contributed [187–189].

HSB also appear in direct semiconductor materials. In heterostructured GaAs/AlAs semiconductors hole confinement was observed as well [190]. In direct semiconductors access is given to the confinement states using optical experimental setups like photoluminescence spectroscopy [191–195] whereas on type IV-semiconductors (like Si) no reports are found in the literature that make use of such techniques.

The *n*-Si(100) is biased under reverse conditions which enables strong band bending. Within the upward bent valence band a potential well is created and additional electronic quantum well states appear. This situation is schematically shown in Fig. 10.3. The HSBs only have a dispersion in momentum parallel to the surface with a maximum at the gamma point, while they have no dispersion perpendicular to the surface [17]. These band bending induced electronic states can act as final states for direct optical transitions resulting in extra peaks in the spectra. The photon energies of the transitions from Γ_2 or Γ_{15} into the HSBs converge towards the known c-v transitions if the transitions occur deeper in the bulk, see Fig. 10.3. But close to the surface, the photon energies reflect the onset of the individual HSBs resulting in steps or peaks in the measured spectra.

If no HSBs are present, two specific transitions [E_0', $E_2(1)$] will occur at the Γ point. In the case of existing HSBs below the valence band edge [$\Gamma_{25'}$], one could expect to find two additional series of peaks from Γ_2 and Γ_{15} in the HSBs. Focusing on the measured spectra, two series of optical transitions were indeed found. The

[2] All given values here were estimated from RT experiments.

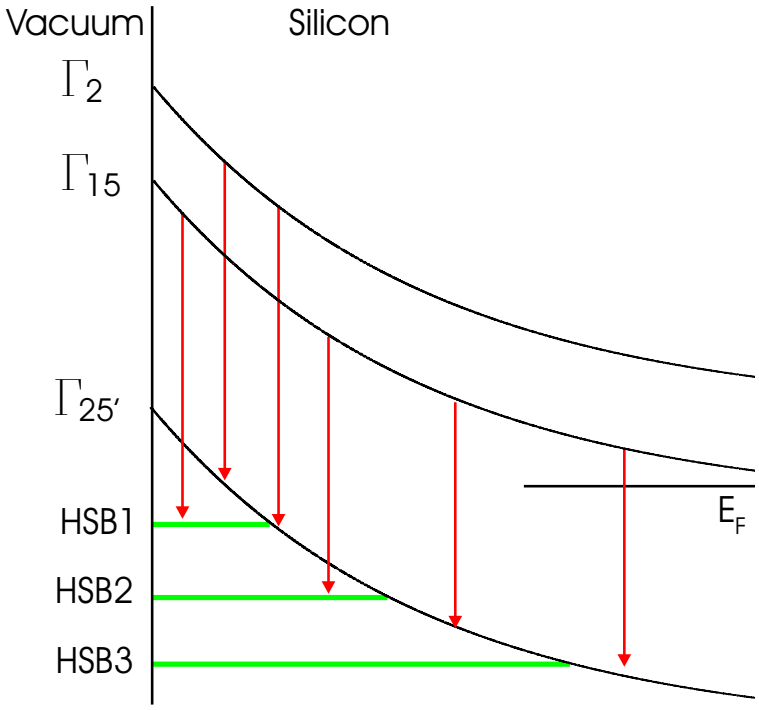

Figure 10.3: (a) Sketch of the HSBs for a n-Si. The upward bent valence band $\Gamma_{25'}$ formes a potential well for holes. The HSBs are located in the space charge region and are without dispersion perpendicular to the surface. The red arrows indicate several electron-hole recombinations which occur in silicon bulk. The electrons from the conduction band at Γ_{15} or Γ_2 can either recombine radiatively with holes in the valence band at $\Gamma_{25'}$ or end up in a HSB state. Note, since the HSBs are without dispersion perpendicular to the surface, the transition energies vary continuously over the space charge layer and finally reach the transition energies of the known c-v transition. But for radiative transitions close to the surface, an onset in the transition energies is expected.

Transition	Photon Energy (eV)	$E(\Gamma_{25'})$ – $E(\mathrm{HSB_n})$ (eV)	Energy levels of HSB_n as calculated (eV)
$\Gamma_{15} \rightarrow \Gamma_{25'}$	3.35±0.04		
$\Gamma_{15} \rightarrow$ HSB1	3.60±0.02[2]	0.25	0.24
$\Gamma_{15} \rightarrow$ HSB2	3.78±0.03	0.43	0.42
$\Gamma_{15} \rightarrow$ HSB3	3.92±0.02	0.57	0.56
$\Gamma_2 \rightarrow \Gamma_{25'}$	4.11±0.01		
$\Gamma_2 \rightarrow$ HSB1	4.35±0.02[1]	0.24	
$\Gamma_2 \rightarrow$ HSB2	4.54±0.05	0.44	
$\Gamma_2 \rightarrow$ HSB3	4.70±0.05[1]	0.59	

[1] appears only in upper curve of Fig. 10.2
[2] appears only in lower curve of Fig. 10.2

Table 10.2: Transition energies as observed and energy levels of the HSBs below the valence band edge [$\Gamma_{25'}$] from experimental data and calculated levels.

peaks from this series are marked with the horizontal dashed lines in Fig. 10.2; and the extracted transition energies are summed up in Table 10.2. The peak positions related to the HSBs located between 4.1 eV and 4.7 eV photon energy are hard to discern, while the transitions of the second series at 3.3 eV to 3.9 eV photon energy were measured with higher precision, see Table 10.2.

If the additional peaks result from HSB states, one distinctive mark of this series is that the energy differences of the transition energies have to respect the energy of the specific HSB. The differences of the direct c-v transitions ($\Gamma_{15} \rightarrow \Gamma_{25'}$ and $\Gamma_2 \rightarrow \Gamma_{25'}$) with the observed transition energies into HSBs have a remarkable consistence -as can be seen in the third column of Table 10.2. This proves that one series of HSBs is responsible for the two series of transition energies.

The potential well can be described approximately as a triangular shaped potential, and the discrete energy levels of the HSBs, with respect to the valence band edge at the surface, can be calculated exactly by using

$$E_n = \left(\frac{\hbar^2}{2m_z^\star}\right)^{1/3} \left(\frac{3\pi eF}{2}\left(n+\frac{3}{4}\right)\right)^{2/3}, \tag{10.1}$$

where $m_z^\star$ is the electron effective mass along the direction perpendicular to the surface, and eF is the slope of the triangular potential [17]. Using equation (10.1) and $m_z^\star = 0.19\ m_e$, taken from Ref. [17] where m_e denotes free electron mass and describes eF as an adjustable fit parameter, the HSBs energy levels below $\Gamma_{25'}$ are calculated at 0.24 eV, 0.42 eV and 0.56 eV for $eF = 0.606$ eV/nm, which matches quite well with the estimated energy differences $E(\Gamma_{25'}) - E(\mathrm{HSB}_n)$, see Table 10.2. The energy differences from the series of transitions between 3.3 eV and 3.9 eV photon energy were only taken into account to show the good matching between experimental data and theoretical expectation, since these experimental data are of less error than the other series. Note, in Ref. [186] the difference in energy from HSB1 to HSB2 was found to be 0.134 eV for a highly p-doped Si sample ($1{\cdot}10^{18}$

cm^{-3}). Here, the energy difference from HSB1 to HSB2 is 0.17 eV, which is larger, but the band bending may be higher due to the altered geometry of the electrical contact made by STM tip.

These findings confirm the assumption made in Chapter 7 that stronger band bending occurs in the low doped silicon samples, as expected from textbooks where a planar geometry of MOS devices is taken into account. Note, in Chapter 7 strong band bending was assumed for *p*-Si under reverse conditions. Here the strong band bending is found for *n*-Si also under reverse bias. A consistent picture is given since for both doping types such strong band bending seems to occur. The high current density in the semiconductor near the apex of the STM-tip and the induced strong electric field play a key role for the presence of this strong band bending. Here further investigations -combined with theoretical approach- are required.

The additional peaks result most likely not from C_{60} excitations. The properties of thin films made of C_{60} on silicon surfaces are well explored with different experimental techniques [196–200], and the observed transition energies in the literature do not match with the experimental observations here.

In summary, the *n*-Si(100) sample is driven under reverse conditions and strong band bending is enabled. The bands were bent upwards and a potential well is created by the upward bent bands and the surface at the Γ-point in the Brillouin zone. Within this potential a series of additional states appear. These additional quantum well states -named hole subbands- result in additional peaks in the light emission spectra; and the energy levels of the hole subband system can be extracted from these spectra. This is the first time that these hole subbands are found in STM induced light emission spectra from silicon.

To confirm the results presented in this chapter it is suggested to continue research with STM induced light emission on clean silicon sample surfaces to eliminate any influence of the adsorbate. With adsorbate at the silicon surface there will always be doubt about the given interpretations in this chapter but due to lack of time it was not possible to perform a new series of experiments.

Chapter 11

Structure of *in vacuo* Rb intercalated $1T$-TaS_2

The text from this Chapter has also been published with this title in *Physical Review B* **74**, 193407 (2006))[1]. B. Murphy, J. Kröger, H. Jensen and Richard Berndt are the co-authors.

11.1 Abstract

Rb adsorption in ultra-high vacuum on the transition metal dichalcogenide $1T$-TaS_2 is investigated by scanning tunneling microscopy at 9 K and at room temperature. Comparison of step heights on clean and Rb-covered surface provides direct evidence that the adsorbed Rb atoms intercalate between the topmost layers of the substrate. This result resolves the current uncertainty about the structure of these widely investigated surfaces. The increase of the van der Waals gap between the substrate layers is discussed on the basis of a sphere model.

11.2 Introduction

Transition metal dichalcogenides (TMDCs) have attracted considerable attention. These materials can serve as the basis for lubricants [23], battery systems [24], and solar cells [25]. Crystals at the nanometer scale were synthesized from TMDCs [201, 202] as well as single-wall nanotubes [203]. Recently, surfaces of TMDCs have been used to fabricate nanostructures [32, 219]. From a fundamental point of view TMDCs present a material class with intriguing phase diagrams which include metal-insulator transitions, charge density waves (CDW), and superconductivity [26, 27]. Owing to their peculiar geometric structure consisting of a periodic stacking of van der Waals-bonded TMDC layers dimensionality effects on the above mentioned phases can be investigated. By intercalation it is possible to tailor the interlayer spacing in these materials while conserving the structural integrity within the layers [217]. During this process the van der Waals gap between the layers is increased

[1]The text was structured with additional sub-titles for pleasant reading

in order to accommodate the intercalated compound. For instance, by preparing reactants in sealed pyrex tubes or using a solution suspension, the *ex situ* insertion of pyridine molecules between TaS_2 layers has been achieved. Electron microscopy and diffraction studies report an increase in the interlayer spacing of about 6 Å while the superconductivity of the hosting substrate is preserved [204, 205]. In other early studies intercalation compounds were prepared during growth or by electrochemical processes [217, 218].

Since the electronic properties can be tuned by introducing intercalate compounds to the host lattice, it is naturally desirable to perform this process *in vacuo* so that dimensionality and electronic properties may be tuned on a local level. Many *in vacuo* photoemission experiments, on alkali metal adsorption on TMDC materials, show that local changes in the host metal d band are evident upon deposition [28–30]. However, the location of the alkali metal cannot be directly determined from such measurements. For instance, a gradual transformation of the three-dimensional electronic structure of clean VSe_2 to an essentially two-dimensional structure of Cs-intercalated VSe_2 has been observed [28]. Rossnagel *et al.* have demonstrated by an angle-resolved photoelectron spectroscopy (ARPES) experiment the continuous tuning of electronic correlations by *in vacuo* Rb adsorption on $1T$-TaS_2 [30]. Charge transfer from the alkali metal to the substrate and simultaneous modification of the interlayer coupling were suggested to drive a Mott-Hubbard type transition at the surface [30].

STM studies have shown that the exposure to large amounts of metal adatoms drives the formation of nanostructures on the surface of $TiTe_2$ and similar materials [31–33]. These studies have suggested that the alkali atoms remain on the surface forming nanostructures and that no intercalation takes place. Recent SEM studies on the other hand show that introducing Cu adatoms to VSe_2 drives a deformation of the top layers such that a nanofold network formation appears [34]. This point of view is supported by ARPES studies of Rb deposition on $1T$-$TaSe_2$ [216]. Despite the interest devoted to electronic and structural aspects of TMDC surfaces, a real-space analysis with atomic resolution which clearly demonstrates intercalation, or lack of it, for *in vacuo* adsorbed atoms has not been reported. Until now only indirect evidence for intercalation has been given. The aim of this study is to determine if adsorbed Rb stays at the surface of $1T$-TaS_2 or intercalates between the layers.

In this Letter we present a scanning tunneling microscopy (STM) study of $1T$-TaS_2 (Fig. 11.1) and Rb-covered TaS_2 at 9 K and at room temperature. By comparing step heights of the clean surface with those of Rb-exposed samples we provide clear evidence that the adsorbed Rb atoms intercalate between the substrate layers. The increase of the step heights of TaS_2 is in accordance with Rb atoms occupying adsorption sites within the van der Waals gap of the substrate.

11.3 Experiment

These experiments were performed in ultra-high vacuum (UHV) with a base pressure of 10^{-9} Pa. Data were acquired by scanning tunneling microscopes optimized for the operation at 9 K and at room temperature. Crystalline order of $1T$-TaS_2

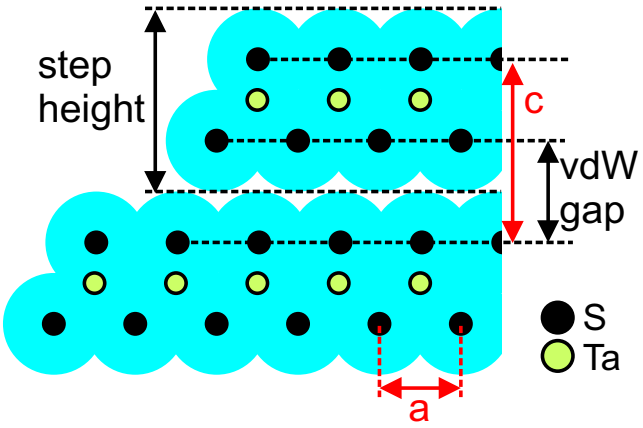

Figure 11.1: (Color online) Sketch of two adjacent layers of $1T$-TaS_2 with indicated van der Waals gap, lattice constants a and c, and step height (identical to c).

surfaces cleaved in UHV was monitored using STM and low energy electron diffraction (LEED). Consistent with previous reports, room temperature LEED of freshly cleaved $1T$-TaS_2 surfaces exhibited a commensurate p($\sqrt{13} \times \sqrt{13}$)R13.9° CDW pattern [30]. Rubidium was deposited onto a clean $1T$-TaS_2 substrate surface by thermal evaporation from a commercial dispenser [206] for 5 minutes. The deposition rate was set to 0.9 Å min^{-1} as monitored with a quartz microbalance. The sample temperature monitored during evaporation with a pyrometer, was less than 340 K.

11.4 Results and discussion

An atomically resolved constant-current STM image of the clean substrate surface at 9 K is shown in Fig. 11.2a. The commensurate CDW is visible: A hexagonal mesh of protrusions with a mutual distance of ≈ 12 Å is attributed to the CDW pattern.

A typical constant-current STM image of Rb-covered $1T$-TaS_2 at 9 K is presented in Fig. 11.2b. We tentatively attribute the highest protrusions to individual Rb atoms which reside on the maxima of the CDW (lower protrusions), though this could also be due to an additional CDW ordering. The apparent height of such a Rb adatom is ≈ 0.9 Å higher than the CDW maxima (≈ 0.3 Å) at the chosen sample voltage and current. The minimum mutual Rb distance is $\sqrt{3}$ times the CDW wavelength. The CDW has hexagonal symmetry with the periodicity of the $\sqrt{13} \times \sqrt{13}$ superstructure known from the clean surface showing the sample is in the $1T$ phase [29].

While on pristine $1T$-TaS_2 the surface was flat over lateral distances of 1 μm, apart from corrugations due to substrate atoms and the CDW, at 9 K the terrace width is limited to ≈ 600 Å. On the terraces we occasionally find a lowering of extended areas by some tenths of an Å and defects such as the indicated disruption (arrows in Figs. 11.2c and d). Figure 11.2d displays a profile across a typical step edge observed at 9 K. From this and many other profiles we measure a step height

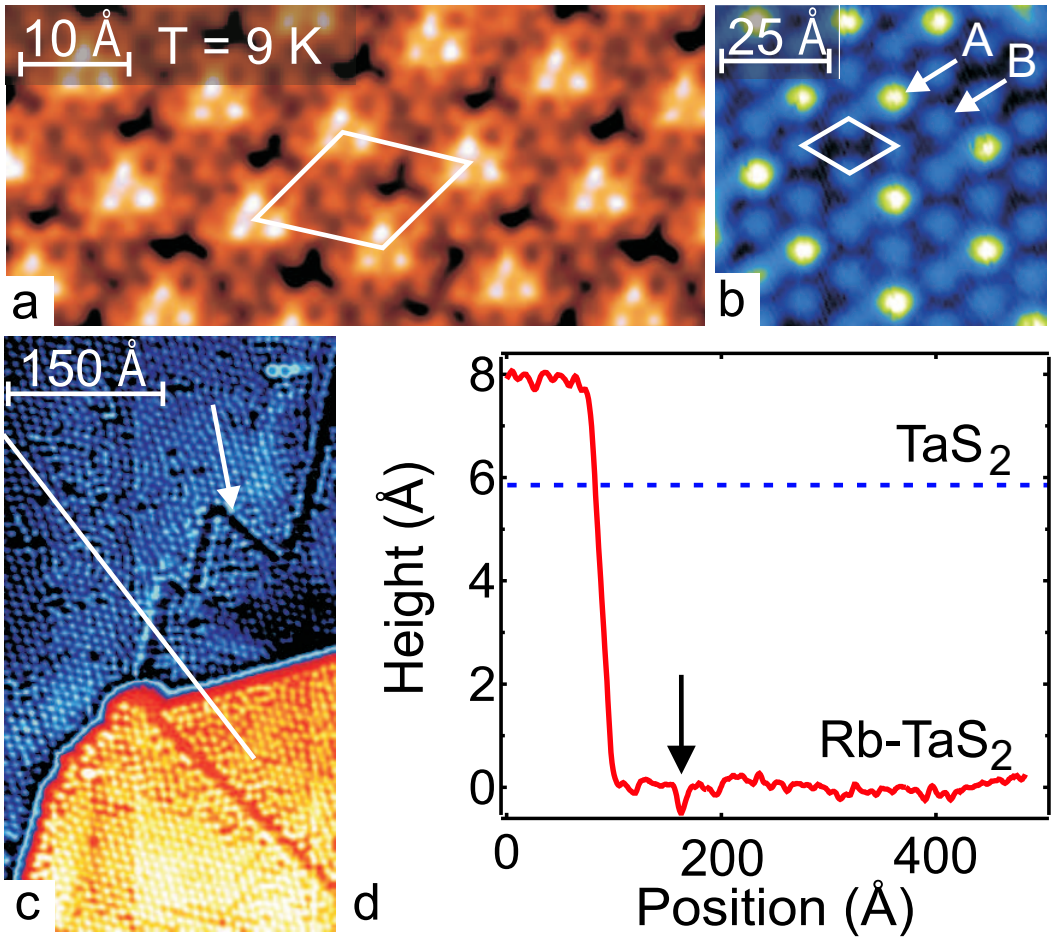

Figure 11.2: (Color online) STM constant-current images of clean and Rb-covered $1T$-TaS_2 at 9 K. (a)Pristine surface atomically resolved (sample voltage V = 850 mV, current I = 480 pA). Maxima with 12.1 Å periodicity are due to the CDW which gives rise to the commensurate $\sqrt{13} \times \sqrt{13}$ superstructure. The CDW unit cell is marked in (a) and (b). (b) Rb-exposed surface with single Rb adatoms (bright spots) residing at some of the CDW maxima (V = 870 mV, I = 370 pA). (c) Two adjacent terraces on the Rb-exposed surface (lighter color depicts upper terrace). Arrow indicates disruption as frequently observed at low temperature. (V = 700 mV, I = 210 pA). (d) Profile across adjacent terraces along the line marked in c. The dashed line indicates the step height of the clean crystal.

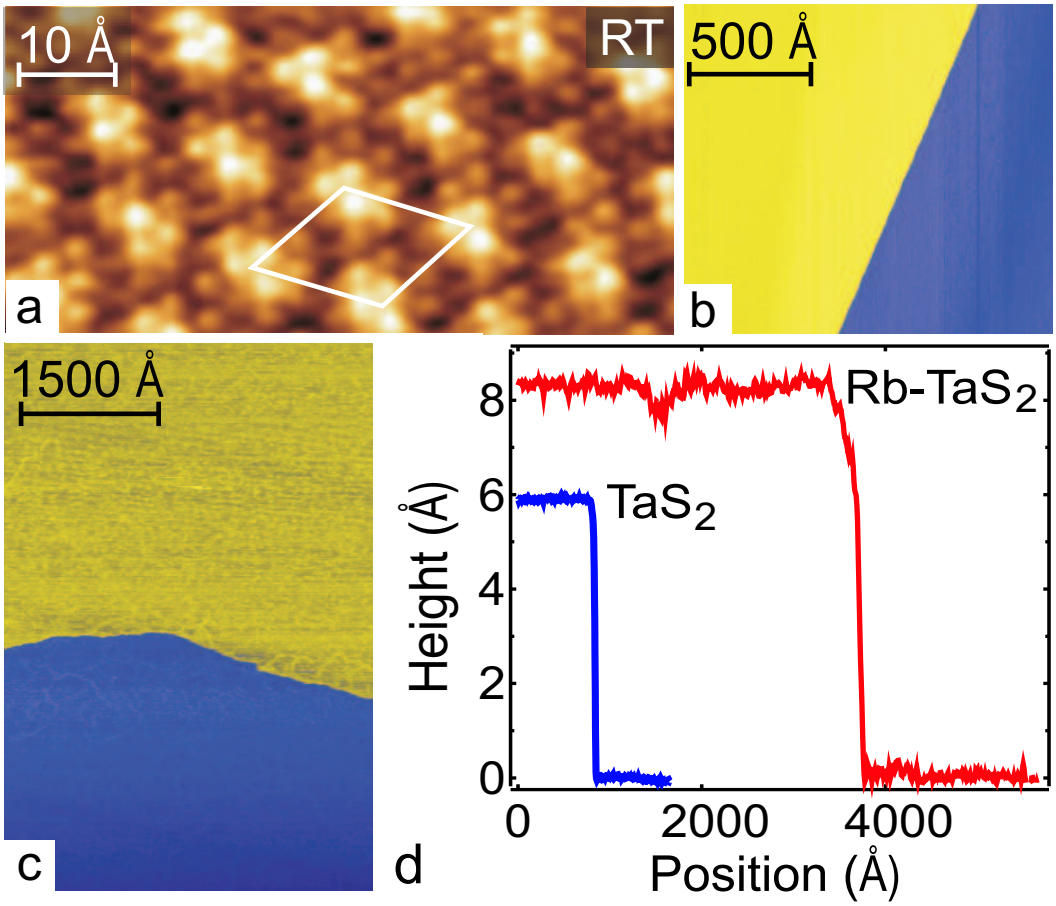

Figure 11.3: (Color online) STM images of $1T$-TaS_2 at room temperature. (a) CDW unit cell of pristine surface in the p($\sqrt{13} \times \sqrt{13}$)R13.9° CDW phase ($V = 75\,\mathrm{mV}$, $I = 140\,\mathrm{pA}$). (b) Adjacent terraces on clean $1T$-TaS_2 with the upper one appearing on the left hand side ($V = 75\,\mathrm{mV}$, $I = 5\,\mathrm{pA}$). (c) Rb-covered TaS_2. The description of the added lines is given in the text.(d) Profiles across two adjacent terraces on the clean (lower curve) and on the Rb-covered (upper curve) surface.

of (7.9 ± 0.3) Å which is 2 Å higher than the expected clean surface step height of 5.9 Å [34, 207]. Intriguingly, the entire top terrace is lifted by $\Delta = (2.0 \pm 0.3)$ Å with respect to the lower one.

At room temperature we also observe an increase in the interlayer spacing of the top two layers. A typical constant-current STM image of an atomically resolved pristine $1T$-TaS_2 surface is presented in Fig. 11.3a. Protrusions correspond to the surface sulfur layer. The height of the protrusions varies according to the periodicity of the p($\sqrt{13} \times \sqrt{13}$)R13.9° CDW. Figure 11.3b shows an example of a straight step edge separating two terraces. The upper and lower terraces appear as two parallel planes with a mutual distance of 5.9 Å as expected (see the lower profile in Fig. 11.3d).

A typical room temperature STM image of Rb-covered TaS_2 is shown in Fig. 11.3c. Rb was again deposited on the clean substrate at room temperature (RT) for 5 minutes [206]. Characteristics of this surface are flat terraces whose step edges do not reveal the same high degree of straightness as observed for the clean surface. In contrast to our observations at low temperatures there is no evidence of layer distortion at room temperature. An observed increase in tunneling current noise is most likely due to diffusing Rb atoms. In Fig. 11.3d profiles across step edges of pristine $1T$-TaS_2 (lower curve) and Rb-TaS_2 (upper curve) are compared. The two data sets are the average over 260 profiles [2]. For the Rb-exposed substrate the step height is increased to (8.3 ± 0.3) Å which corresponds to a lifting of the topmost layer by $\Delta = (2.4 \pm 0.3)$ Å. As in the low-temperature experiment this observation is clear evidence of Rb intercalation into the topmost van der Waals gap. The profile presented in Fig. 11.3d (upper curve) shows that intercalation is not only confined to the vicinity of the step edges but occurs over extended length scales of at least 3000 Å.

Our observations are consistent with a structural model of expected adsorption sites for Rb atoms intercalated in the van der Waals gap. Below we relate the measured step height increase to Rb-induced opening of the van der Waals gap. Figure 11.4a shows a sketch of two adjacent S layers embracing the van der Waals gap. Possible Rb adsorption sites between these sulfur layers are depicted by large circles. The top adsorption site (t) is coordinated by three sulfur atoms in the lower layer and by a single sulfur atom of the top layer; the hollow site (h) is coordinated by six S atoms (three each in the lower and upper layer); the bridge site is positioned between two S atoms of the lower level. The width of the van der Waals gap is defined as the distance between these adjacent sulfur layers. While the S atoms are described as spheres with a radius of 1.67 Å [208], the radius of the sphere representing the Rb ion is varied such as to give the experimentally observed increase of the step height. Using simple geometric considerations and keeping the in-plane lattice parameter of 3.36 Å as suggested by recent theoretical work [34, 209], we calculate the step height increase within the sphere model of S

[2] Each cross section is taken along the (cs) line in Fig. 11.3c and start from (s) line and end at (e) line. Then all extracted cross sections are averaged. The step edge is not exactly running in one direction, and as a result of averaging the step edge in Fig. 11.3d seems to be broadend. The step edge within a single cross section is step like.

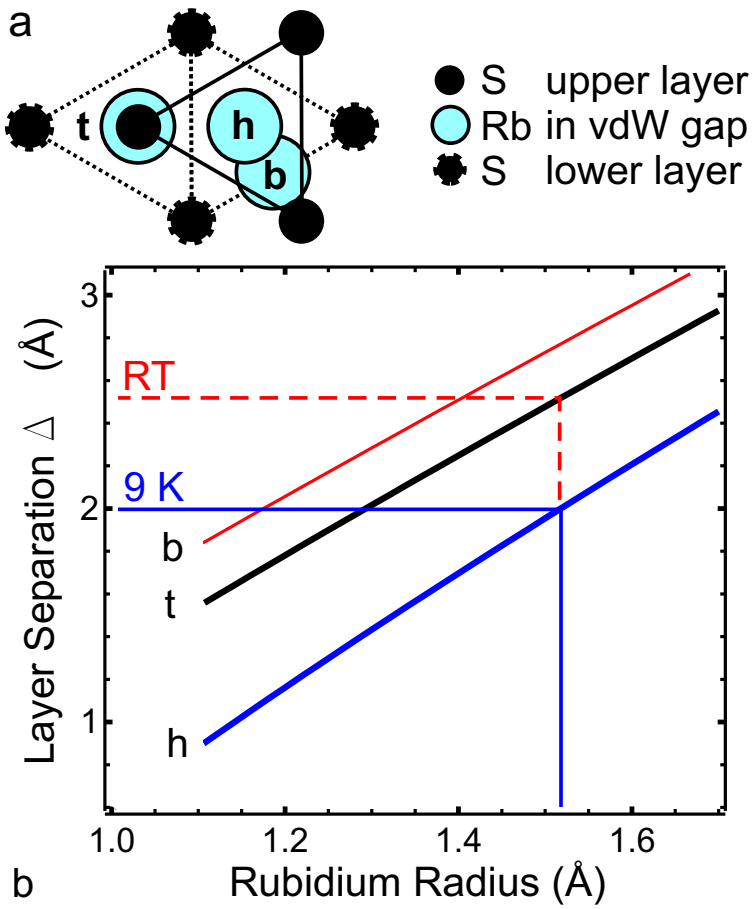

Figure 11.4: (Color online) (a) Top view of three high-symmetry adsorption sites within the van der Waals gap of $1T$-TaS_2 between the top layer (full lines) and lower layer (dashed lines). Small circles denote S atoms, large circles denote Rb atoms occupying (h) hollow, (t) top, and (b) bridge sites. (b) Calculated layer separation Δ versus Rb radius for high-symmetry adsorption sites at room temperature (RT) and 9 K.

and Rb atoms for the different adsorption sites within the van der Waals gap. Three curves (Fig. 11.4b) correspond to Rb occupation of the three high-symmetry sites shown in Fig. 11.4c. At 9 K the experimentally observed increase in layer spacing is $\Delta = (2.0 \pm 0.3)$ Å which is consistent with Rb atoms occupying the h site and revealing a sphere radius of (1.5 ± 0.1) Å. This result is in agreement with an ion radius of Rb of 1.49 Å [208]. The Rb atom is known to transfer much of its valence electron to the *d* band of the substrate [217, 218]. Using the ion radius of Rb obtained for the low-temperature situation the layer lifting of $\Delta = (2.4 \pm 0.3)$ Å at room temperature can be reproduced, if we assume that Rb additionally resides at the t sites within the van der Waals gap. Lacking data for the energy required to lift a layer of TaS_2, we estimate the interlayer binding energy using calculated results for MoS_2 [210]. In order to increase the interlayer separation necessary to occupy t sites a barrier of approximately 15 meV has to be overcome per unit cell. This very small difference suggests that, at room temperature, Rb atoms diffusing within the van der Waals gap can occupy h and t sites simultaneously, while at 9 K only the h sites are predominantly occupied.

11.5 Conclusion

In summary, on the basis of STM data the key question of where Rb atoms are located following *in vacuo* adsorption on $1T$-TaS_2 has been answered. The increase in interlayer spacing observed in the STM data is clear evidence that Rb intercalates into the van der Waals gap between the topmost layers. This evidence is confirmed within a geometrical model of the atomic layers. Small differences in the spacing between room temperature and low temperature data are consistent with Rb atoms residing at different high-symmetry sites within the van der Waals gap. As the behavior of alkali or metal adatoms on TMDCs is generally similar, we propose that our results are also valid for this class of materials in general.

We are delighted to thank K. Rossnagel and L. Kipp for providing TaS_2 crystals and for discussions. This work was supported by the Deutsche Forschungsgemeinschaft grants FOR 353/2-2 and KR 2912/3-1.

Chapter 12

Scanning tunnelling microscopy and spectroscopy investigation of rubidium-induced Mott -Hubbard transition on *1T*-TaS_2

The text from this Chapter has also been published with this title in *New Journal of Physics* **10**, 13022 (2008). J. Kröger, B. Murphy and Richard Berndt are the co-authors.

12.1 Abstract

The effect of rubidium deposition on $1T - TaS_2$ was investigated by scanning tunnelling microscopy and spectroscopy at room temperature. While the clean surface is characterized by a charge density wave with hexagonal symmetry, the rubidium-covered surface exhibits a rectangular symmetry of the charge density wave. The spectroscopy data signals a Mott-Hubbard phase transition by an energy gap between upper and lower Hubbard bands giving rise to a Coulomb interaction energy of 1 eV. Owing to spatially resolved spectroscopy the energy gap can be directly related to the rectangular charge density wave phase. In addition, rubidium adsorption further leads to the formation of a network of linear wires. Scanning tunnelling spectroscopy indicates that the wires are most likely not fabricated from rubidium.

12.2 Introduction

Transition metal dichalcogenides have attracted considerable attention because of their quasi-two-dimensional character giving rise to unique electronic properties [27]. They present a material class with intriguing phase diagrams which include metal-insulator transitions, charge density waves, and superconductivity [26, 27]. Owing to their peculiar geometric structure consisting of a periodic stacking of van der

Waals-bonded transition metal dichalcogenide layers, dimensionality effects on the above mentioned phases can be investigated.

In this article, particular interest is devoted to a Mott-Hubbard-type metal-insulator transition where the width of involved electron bands decreases such as to render the o*n*-Site Coulomb repulsion between electrons dominant. As a result of this phase transition, a formerly partially filled band is split into an unoccupied and an occupied band. The latter are generally referred to as the upper and lower Hubbard bands. A phase transition of the Mott-Hubbard type may be induced by modifiying the chemical composition [211], by the application of pressure [212], by changing the temperature of charge density wave systems [213], or by adsorption of alkali metals on transition metal dichalcogenides [30].

The two latter methods are particularly appealing since they allow control of the band width and the Coulomb correlation energy in the same crystal. A recent angle-resolved photoelectron spectroscopy experiment [30] was performed on $1T - TaS_2$ and revealed the evolution of the electronic structure near the Fermi level across the metal-insulator transition. Upon rubidium deposition at room temperature a Ta $5d$ band was observed to shift to higher binding energies and therefore interpreted as the lower Hubbard band. The upper Hubbard subband, however, was not monitored since photoemission experiments are sensitive to occupied electronic states while unoccupied states are difficult to access.

Here we present scanning tunnelling microscopy and spectroscopy data for the clean and rubidium-covered $1T - TaS_2$ surface. As key results we show in direct space the rubidium-induced modification of the charge density wave from a hexagonal to a rectangular symmetry and, owing to the sensitivity of tunnelling spectroscopy to occupied as well as unoccupied electronic states, spectroscopic evidence for the rubidium-driven splitting of the upper and lower Hubbard bands. Thus, we directly relate the rectangular charge density wave phase to the Mott-Hubbard gap and provide a direct measure of the Coulomb interaction energy. By spatially resolved spectroscopy we find indication that the rubidium-induced wire network is not fabricated from rubidium.

12.3 Experiment

Experiments were performed using a home-built scanning tunnelling microscope operated in ultrahigh vacuum at a base pressure of 10^{-9} Pa and at room temperature. Single crystal samples were grown by chemical vapor transport and clean surfaces were obtained by *in vacuo* cleavage. Rubidium was deposited onto freshly cleaved $1T - TaS_2$ from commercial dispensers [206]. The deposition rate of $\approx 0.9\,\text{Å}\,\text{min}^{-1}$ was monitored by a quartz microbalance. Deposition was performed for 5 min to obtain a similar coverage to that reported in Ref. [30]. During deposition the pressure of the recipient stayed below 5×10^{-8} Pa. Prior to scanning tunnelling microscopy (STM) experiments the surfaces were characterized by low-energy electron diffraction (LEED). Spectroscopy of the differential conductance ($\mathrm{d}I/\mathrm{d}V$) was performed by superimposing a sinusoidal voltage (root-mean-square amplitude $1 - 2$ mV, frequency $4 - 8$ kHz) onto the tunnelling voltage and measuring the current response

with a lock-in amplifier. STM images were acquired in the constant-current mode and the voltage was applied to the sample.

12.4 Results and Discussion

To reveal the rubidium-induced changes in direct space most clearly, the charge density wave (CDW) of clean and rubidium-covered $1T - TaS_2$ is presented in Figs. 12.1a and 12.1b, respectively. The clean surface exhibits a CDW visible as the brightest protrusions in Fig. 12.1a. The CDW superstructure is described by a $p(\sqrt{13} \times \sqrt{13})R13.9°$ unit cell indicated by the lozenge with dimensions of $\approx 12\,\text{Å} \times 12\,\text{Å}$. This finding is in good agreement with electron diffraction results [214] and LEED patterns reported in Ref. [31]. Sulfur atoms appear as almost circular protrusions in a hexagonal arrangement and with a mutual distance of $\approx 3.4\,\text{Å}$ in accordance with the in-plane lattice constant [215]. After deposition of rubidium for $\approx 5\,\text{min}$ the LEED pattern changed from a $(\sqrt{13} \times \sqrt{13})R13.9°$ to a three-domain $c(2\sqrt{3} \times 4)$ structure which has previously been observed [30, 31]. A typical STM image of this surface is presented in Fig. 12.1b. We experienced an increase in the tunnelling current noise which we attribute to diffusing rubidium atoms [37] and therefore stable imaging was possible only for several scan lines. Nevertheless, in case of stable imaging a rectangular structure as depicted in Fig. 12.1b was observed. We attribute the protrusions in Fig. 12.1b to the maxima of the CDW which exhibit a rectangular arrangement. By measuring the distances a and b for more than 100 protrusions we find $a = (12.0 \pm 0.6)\,\text{Å}$ and $b = (13.0 \pm 0.6)\,\text{Å}$ where the error margins correspond to standard deviations. These dimensions are close to the CDW unit cell dimensions reported in Ref. [31] ($a = 11.64\,\text{Å}$, $b = 13.44\,\text{Å}$). We notice that images with larger lateral sizes (not shown) exhibit three $c(2\sqrt{3} \times 4)$ domains which are rotated by 60° with respect to each other and which are in accordance with the above mentioned diffraction patterns [31]. On an average, domain sizes are $\approx 150\,\text{Å} \times 150\,\text{Å}$. In agreement with previous studies [29, 31, 221], we find that alkali metal adsorption on $1T - TaS_2$ induces strong modifications of the CDW phase. The transition from a hexagonal to a rectangular symmetry of the CDW phase has not been unraveled yet. In Ref. [31] the authors suggest that the rubidium-induced network of nanowires (to be discussed below) causes the CDW to align along the wires leading to the observed reduction of symmetry. For a similar system, namely TaS_2-Na, Pettenkofer *et al.* [29] found that the Ta d_{z^2} band was populated by Na $3s$ electrons leading to a shift of the band below the Fermi level and thus giving rise to an increase of the Fermi surface. As a consequence, spanning vectors of nested Fermi surface contours were modified leading to the new superstructure. The relation between Fermi surface nesting vectors and CDW superstructures is discussed, for instance, in Refs. [222, 223].

Next, we discuss the electronic properties of clean and rubidium-covered $1T - TaS_2$. Rossnagel *et al.* [30] showed by angle-resolved photoelectron spectroscopy that for the $c(2\sqrt{3} \times 4)$ CDW phase, the lower Hubbard band reached its lowest binding energy. In Fig. 12.2 we compare $\mathrm{d}I/\mathrm{d}V$ spectra of the clean and the rubidium-covered TaS_2 surface. For clean $1T - TaS_2$ a half-filled Ta $5d$ band lies close to

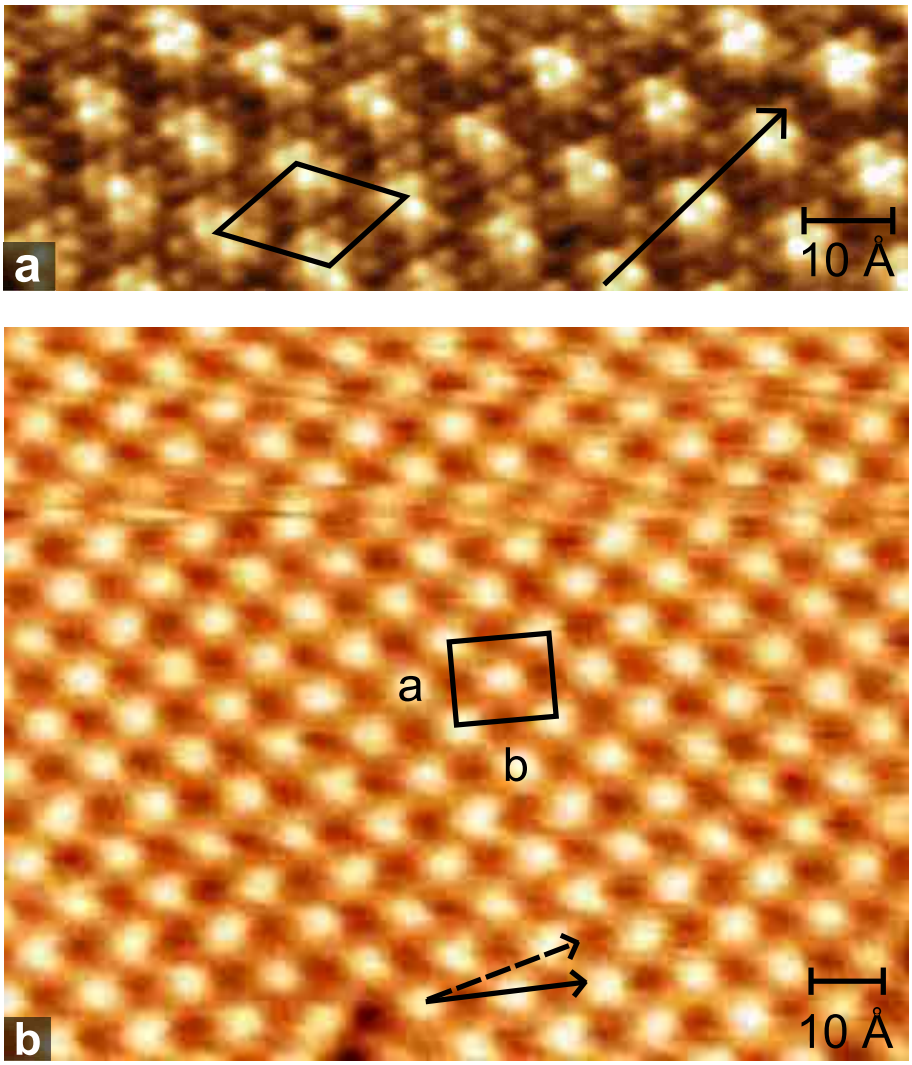

Figure 12.1: (Color online) (a) Atomically resolved charge density wave on clean $1T - TaS_2$ (current $I = 0.15\,\mathrm{nA}$, voltage $V = 75\,\mathrm{mV}$). The lozenge shows the charge density wave unit cell. The arrow indicates one crystallographic direction of the charge density wave unit cell. (b) STM image of the charge density wave of rubidium-covered $1T - TaS_2$ ($I = 25\,\mathrm{pA}$, $V = 0.75\,\mathrm{mV}$). The unit cell of the charge density wave is illustrated by the rectangle. Arrows indicate crystallographic directions of charge density wave unit cells of clean (dashed line, see also (a)) and rubidium-covered (full line) $1T - TaS_2$. The angle between these directions is $\approx 14°$ and corresponds to the rotation angle of the charge density wave phase on clean $1T - TaS_2$. The STM image shows plane-subtracted raw data.

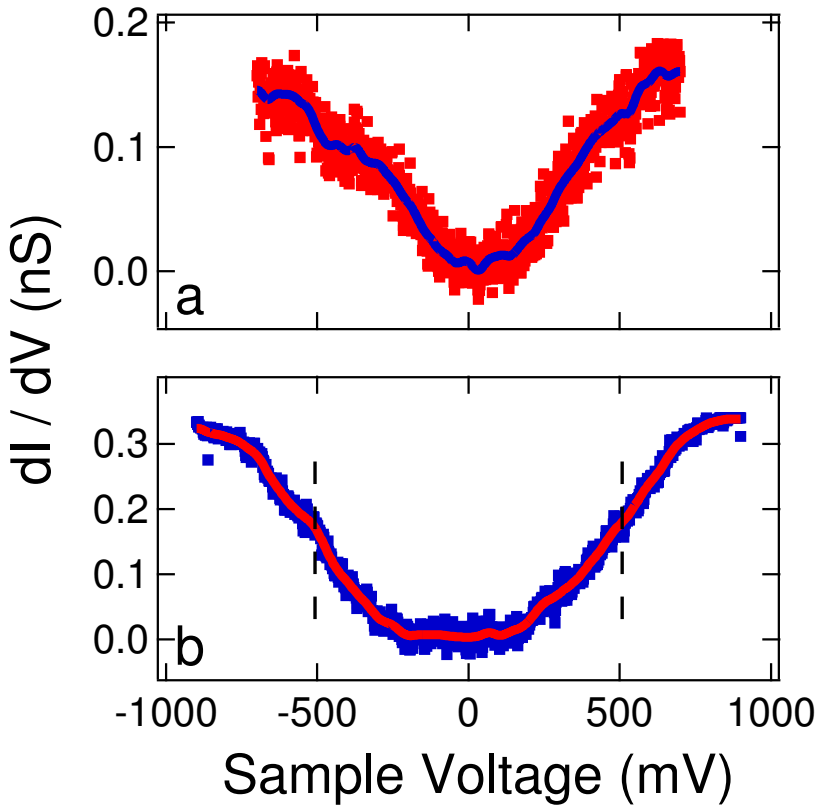

Figure 12.2: (Color online) (a) $\mathrm{d}I/\mathrm{d}V$ spectrum of clean $1T - TaS_2$. Feedback was opened at $V = 610\,\mathrm{mV}$ and $I = 50\,\mathrm{pA}$. (b) $\mathrm{d}I/\mathrm{d}V$ spectrum of rubidium-covered $1T - TaS_2$. Feedback loop parameters: $V = 710\,\mathrm{mV}$, $I = 80\,\mathrm{pA}$. Dashed lines indicate the position of the middle of the $\mathrm{d}I/\mathrm{d}V$ signal onsets. Lines in (a) and (b) display smoothed data and serve as a guide for the eye.

the Fermi level and defines the Fermi surface [30, 224]. We interpret the spectroscopic structure in Fig. 12.2a as the signature of the Ta $5d$ occupied and unoccupied density of states (the Fermi level is located at $V = 0$). Rubidium adsorption leads to marked changes in the electronic structure as revealed by the spectrum shown in Fig. 12.2b which is representative for areas exhibiting the c($2\sqrt{3} \times 4$) CDW superstructure. The onsets of the Ta $5d$ band are split further away from the Fermi level and thus give rise to a depletion of the density of states in an energy interval of $\approx 0.4\,\mathrm{eV}$ width around the Fermi energy. The middle of the d band onsets are located at $\approx \pm 0.5\,\mathrm{eV}$. An analogous shift of spectral weight of the occupied Ta $5d$ band to $\approx 0.5\,\mathrm{eV}$ below the Fermi energy was reported by Rossnagel *et al.* [30] and interpreted as a result of a rubidium-induced Mott-Hubbard transition and consistently the photoemission peak as the spectroscopic signature of the lower Hubbard band. Adopting this interpretation, we attribute the onsets in the $\mathrm{d}I/\mathrm{d}V$ spectrum of Fig. 12.2b to the lower and upper Hubbard band. The width of the gap between the onsets is $\approx 1.0\,\mathrm{eV}$. Pristine $1T-TaS_2$ is known to exhibit a temperature-induced Mott-Hubbard transition at $\approx 180\,\mathrm{K}$ with the centroids of the Hubbard bands being separated by 0.3 to 0.4 eV [225–227]. Owing to the sensitivity to occupied as well as to unoccupied electronic states with tunnelling spectroscopy we can measure the gap width without resorting to more sophisticated data evaluation and thus have direct access to the Coulomb interaction energy. The spectroscopic data gives complementary information to previously published photoemission data [30] and corroborates the conclusion of a rubidium-induced Mott-Hubbard transition.

To understand why rubidium adsorption may drive a Mott-Hubbard phase transition, it is helpful to understand the induced modifications of the Coulomb repulsion energy, the width and the filling of the involved electron bands. First, as can be deduced from the $\mathrm{d}I/\mathrm{d}V$ spectra, the width of the energy gap between the lower and upper Hubbard band and thus the Coulomb repulsion energy is increased. Further, a previous STM investigation of rubidium-covered $1T - TaS_2$ by Schmidt *et al.* [37] showed that the adsorbate intercalates into the van der Waals gaps between the transition metal dichalcogenide layers and therefore gives rise to an increased distance between the layers. As a consequence, the interlayer coupling may be reduced. This assumption is corroborated by an observed decreased width of electron bands perpendicular to the layers [30]. Calculations reported by Bovet *et al.* [228] indicate that the bandwidth perpendicular rather than parallel to the layers is an important parameter for the Mott-Hubbard transition. Moreover, Rossnagel *et al.* [30] concluded by analysing the evolution of the Fermi surface of $1T - TaS_2 - Rb$ for various rubidium coverages that electron transfer from the alkali metal to the Ta $5d$ conduction band is negligible. As a consequence, the band filling is almost unaltered upon rubidium deposition. We therefore conclude that rubidium adsorption increases the ratio of the Columb repulsion energy and the band width giving rise to a critical value which induces a Mott-Hubbard transition.

Taking advantage of scanning tunnelling spectroscopy to provide information about the local electronic structure we explored the extent the Mott-Hubbard gap was influenced by surface modifications. Rubidium-covered TaS_2 exhibits a network of nanometer scale wires whose nature is still under debate. Similar honeycomb-like

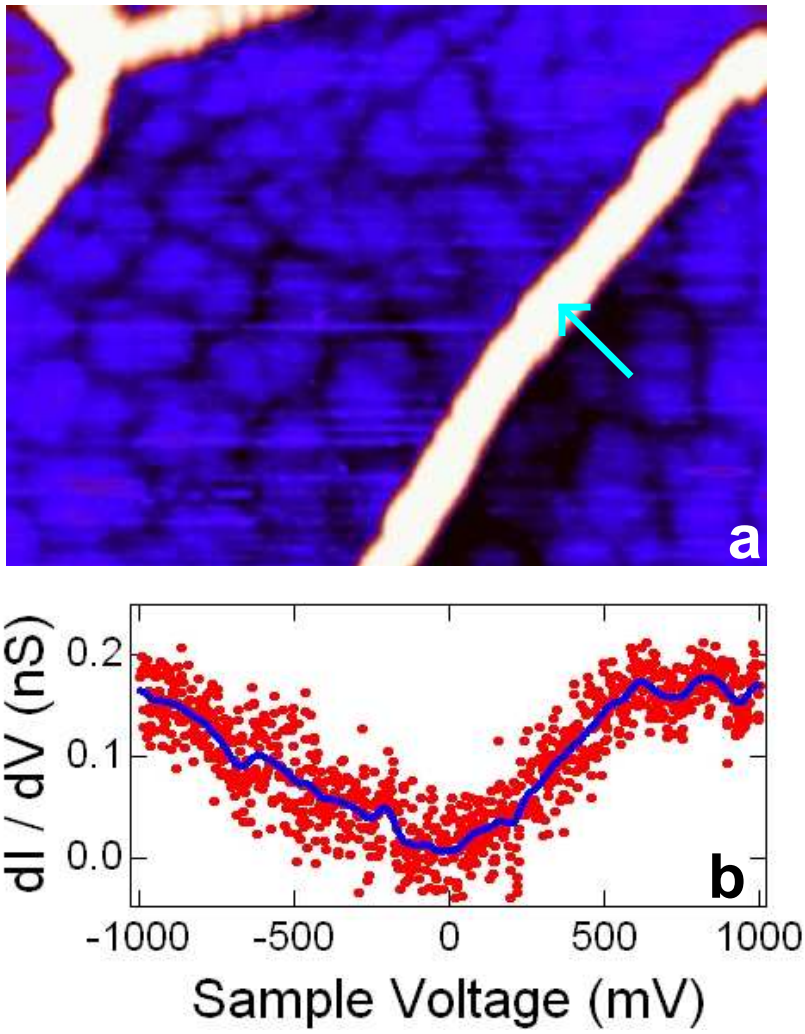

Figure 12.3: (Color online) (a) STM image of rubidium-covered $1T - TaS_2$ at room temperature. The linear protrusions are part of an adsorbate-induced network of wires. ($V = 0.86\,\mathrm{V}$, $I = 0.04\,\mathrm{nA}$, $5400\,\text{Å} \times 4000\,\text{Å}$). (b) $\mathrm{d}I/\mathrm{d}V$ spectrum acquired at the site indicated by the arrow in (a). The line depicts smoothed data. Feedback loop parameters: $V = 1\,\mathrm{V}$, $I = 0.1\,\mathrm{nA}$.

networks on rubidium-covered $TiTe_2$ [32] and copper-covered VSe_2 [219, 229] were reported previously. While in Refs. [32, 229] it was argued that the nanostructures consist of adsorbate material within cracks of the layered crystal surface, in Ref. [219] the nanostructures were interpreted as nanoscale folding patterns induced by adsorbate intercalation and strain relief.

Linear nanostructures observed on the rubidium-covered $1T - TaS_2$ surface are shown in Fig. 12.3a. The STM image shows a part of a network of wires whose width is $\approx 400\,\text{Å}$ and whose apparent height is $\approx 30\,\text{Å}$. As the composition of these structures is a topic of discussion (see above), we acquired $\mathrm{d}I/\mathrm{d}V$ spectra on top of the wires. A generally noisy tunnel current hampered spectroscopy data collection. However, several curves were successfully obtained. In Fig. 12.3b a representative spectrum is shown. The spectrum shows a depletion of the $\mathrm{d}I/\mathrm{d}V$ signal close to the Fermi level. Therefore, the wires are probably not fabricated from rubidium as then one would expect an almost constant $\mathrm{d}I/\mathrm{d}V$ signal around the Fermi level.

12.5 Conclusion

In summary, rubidium adsorption on $1T - TaS_2$ leads to marked structural and electronic modifications. The symmetry of the CDW phase changes from hexagonal to rectangular and concomitantly the surface undergoes a Mott-Hubbard transition. Using scanning tunnelling spectroscopy a direct relation between the rectangular CDW phase and the Mott-Hubbard gap was established. A Coulomb interaction energy of 1 eV was obtained. The adsorbate-induced network of linear wires is most probably not fabricated from rubidium.

We thank K. Rossnagel and L. Kipp for providing TaS_2 crystals and for discussions. STM images were processed using Nanotec WSxM [231]. This work was supported by the Deutsche Forschungsgemeinschaft through KR 2912/3-1.

Chapter 13

Summary

In this thesis evidence was given that the induced light emission by STM in silicon occurs from radiative transitions between electronic states in the Brillouin zone of silicon bulk. The well known direct optical transitions at several points in the silicon Brillouin zone were successfully resolved. In the case of electrons tunneling from the tip into the silicon sample, the electrons undergo an Auger process and electron-hole pairs are generated. The generated holes might be radiatively recombine either with one of the electrons participated on the Auger process or with a second tunneled electron.

If the electron tunnels from the silicon into the STM-tip (opposite applied voltage), an explanation of luminescence based on interband transitions or electron-hole recombination has to take into account that light emission was observed experimentally only from p-type silicon, while spectra from n-type silicon appear still dark. Note, that for this polarity the n-type silicon samples were driven under forward bias and the p-type silicon under reverse bias where strong band bending occurs. The radiation still results from electron-hole recombination, but in this case the strong band bending enables light emission. A model proposed for light emission claims that the emission is balanced by band bending, Zener tunneling, Auger processes, and hole tunneling. Theoretical investigations support this scenario of strong band bending and of the electrons' transfer via Zener tunneling into the conduction band states.

Since the band bending in n-type silicon for this polarity is suppressed due to the forward current direction, no light emission is expected to be observed in agreement with experimental data.

In order to find optical transitions resulting from molecules, a new experiment was started. C_{60} molecules were evaporated on a n-type (2×1)-Si(100) surface; and to get a high intensity of the light emission spectra the tunneling current was increased. A modification of the C_{60} layer was induced by the STM-tip. Analysis of the molecules heights indicate a change of the bonding status from a weak van der Waals bonding into a chemisorbed one. After the surface has altered once, stable tunneling conditions were achieved which enable spectra recording. Sadly, the spectra recorded from this surface exhibit no indication of C_{60} transitions, and the spectra are still dominated by radiation resulting from silicon bulk. The above

mentioned silicon interband transitions are again found, but also an another type of optical transitions in silicon bulk is suggested to be resolved in the spectra.

The silicon sample is driven under reverse bias (positive sample voltage) and strong band bending is suggested to happen. A potential well is created by the upward bent bands at the surface. Within this band bending induced potential well a series of additional states -named hole subbands- appear. Radiative transitions from the conduction bands at the Γ-point into these hole subbands are most likely observed in the light emission spectra. This allows one to measure the energy levels of the hole subbands system below the bulk valence band edge. The measured energy levels are compared with calculated energy levels. The good matching of calculated and measured energy levels confirms that the band bending induced hole subbands can be explored using STM light emission.

Nevertheless, it is suggested to repeat this experiment on pristine n-Si(100) samples to eliminate any influence of the adsorbates. The work on the hole subbands may offer a way for getting a deeper insight into the nature of hole subbands and the band bending of semiconductors under STM tunneling contact. For that further, investigations are required.

The second part of this thesis is about the influence of Rb on $1T$-TaS_2. The question of where Rb atoms following *in vacuo* adsorption on $1T$-TaS_2 are located, has been answered. The increase in interlayer spacing observed in the STM data is clear evidence that Rb intercalates into the van der Waals gap between the topmost layers. This evidence is confirmed within a geometrical model of the atomic layers. As the behavior of alkali or metal adatoms on TMDCs is generally similar, it is proposed that the results are also valid for this class of materials in general.

The presence of Rb changes the charge density wave from an incommensurate $p(\sqrt{13} \times \sqrt{13})$R13.9° CDW into a $c(2\sqrt{3} \times 4)$ CDW, previously seen with LEED investigations. This CDW transition was observed in direct space with STM. From ARPES investigations, it has been shown that a gap at the Fermi energy opens, which is related to a Mott-Hubbard transition upon *in vacuo* Rb deposition. The complete gap of 1 eV was estimated using scanning tunneling spectroscopy. The high spatial resolution of scanning tunneling spectroscopy allows one to explore the electronic structure atop a Rb driven nanostructure. The spectroscopic signature is not metallic, and it is concluded that the nanostrucures are not fabricated from the adsorbed Rb.

Appendix A

Chemical identification of Se and S in $TiSe_{1.2}S_{0.8}$ using Scanning Tunnelling Microscopy

---

TMDCs are of great interest due to the physical behavior related to their quasi two dimensional structure. In one focus of research is the topic of diffusion properties of intercalated material like ions or atoms [210, 232]. Since surface corrugation may influence diffusion properties in this work, the surface structures of mixed phase TMDC $TiSe_{1.2}S_{0.8}$ and $TiSe_2$ were analyzed. Investigations were done to identify individual Se and S atoms by their heights as they appear in the surface layer. It was possible to get atomic resolution in a high quality so that the atomic heights of the surface atoms could be estimated. A model for identifying the individual species was developed and successfully used for this system.

The experiments were done at the RT–STM. All samples were cleaved in vacuum and tips were made of tungsten just heated in vacuum.

The samples of the single phase $TiSe_2$ crystal type exhibit an atomic lattice made of Se atoms as can be seen by the regular protrusions in Fig. A.1a. Irregular arrangements of bright areas on a larger size of several Se atoms' diameters are also visible at the surface. Since $TiSe_2$ is known to be a semiconductor [207] or a semimetal [217] this bright structure may eventually result from dopants buried under the surface analogue to III–V semiconductors where dopants appear in STM topographs in a similar way as observed here [233–237]. On the layered structure, semiconductors TMDCs WS_2 and WSe_2 burried dopants are observed as well [238–240]. Since the STM is sensitive to the changed local density of states around the buried dopants an area of increased height is observed. The height of this dopant area appears of ≈ 0.3 Å above the undisturbed surface layer. A closer view on the atomic scale is given in Fig. A.1b where the surface atoms appear in a uniform manner.

A STM image from the mixed phase crystal $TiSe_{1.2}S_{0.8}$ is displayed in Fig. A.2a. Here, a structure of irregular bright areas, as well as the uniform hexagonal lattice of the surface atoms, is visible. A closer view on the atomic scale is given in Fig. A.2b. The protrusions attributed to single surface atoms are arranged in a uniform hexag-

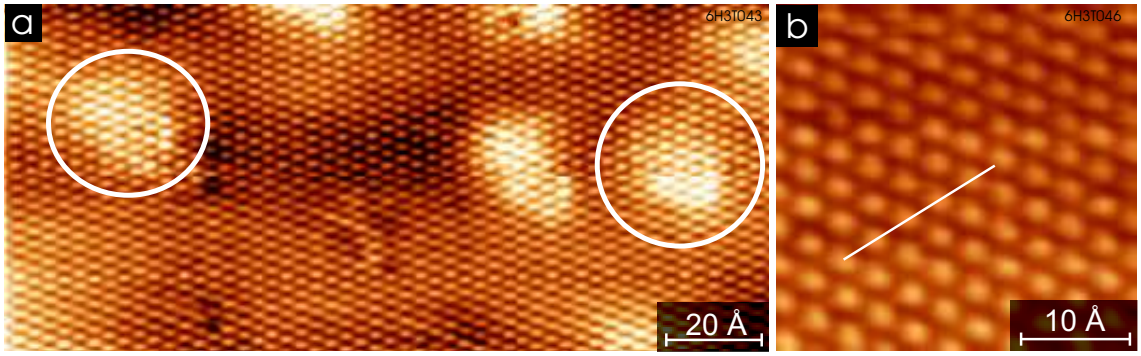

Figure A.1: (a) STM topograph of $TiSe_2$ (-20 mV; 200 pA). The uniform lattice represents individual Se atoms. The larger bright areas (two of those are inside the white ellipses) may result from dopant states buried under the surface. (b) Closer view to the Se lattice (-11 mV; 200 pA). Individual Se atoms are clearly to see. A cross sectional profile along the white line is shown in Fig. A.3a.

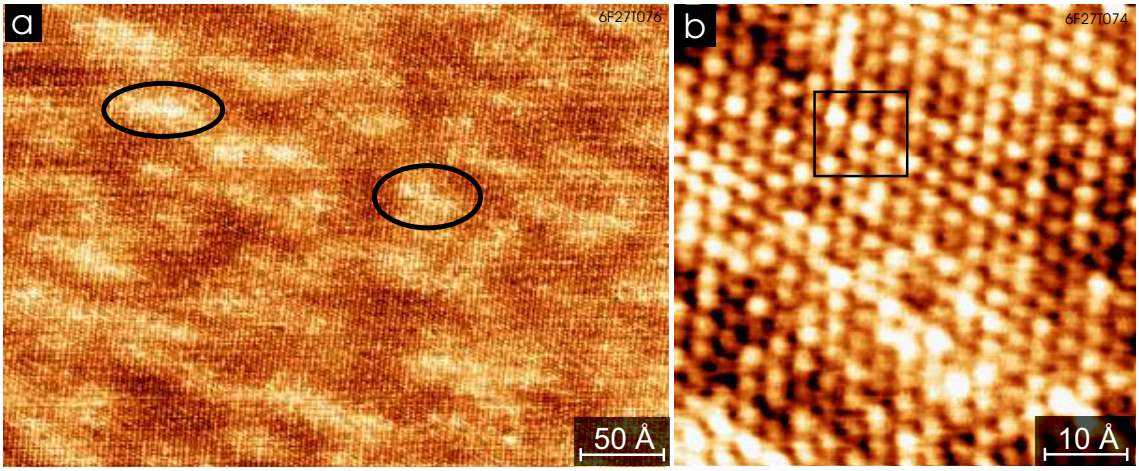

Figure A.2: (a) STM topograph of $TiSe_{1.2}S_{0.8}$ (-167 mV; 720 pA). The deformations, as mentioned in the text, are the bright areas. Two of those are indicated in the black ellipses. (b) $TiSe_{1.2}S_{0.8}$ topograph (-167 mV; 720 pA) with atomic resolution. The individual atoms do not appear as uniform as on $TiSe_2$. The different appearance results from the two species of surface atoms (S and Se) resolved differently in STM.

onal lattice, but the appearance of an individual atom is not as uniform as for the single phase crystal $TiSe_2$. Here Fig. A.2b suggests an attribution of the atoms to a S or Se atoms. By analyzing the atomic corrugation here chemical identification is possible.

Cross sectional profiles along the centers of the atom and along the crystal main directions are shown in Figs. A.3 a,b. Each protrusion of the data represents an individual surface atom. The profile of $TiSe_2$ represents the uniform shape as expected from the topograph (Fig. A.1b). The in plane lattice constant of (3.3 ± 0.2) Å is in accordance with the value 3.4048 Å known from literature [207]. The atoms in the profile from $TiSe_{1.2}S_{0.8}$ are of different heights. To analyze the surface heights a model based on atomic corrugations was used to identify individual species. The atomic corrugation is defined here as the difference between the maximum height of an atom and the minimum height next to it in the direction of its nearest neighbor (also named *valley* in this text). Fig. A.3b demonstrates the procedure of estimating values of atomic corrugations. Note, each valley has two corrugation heights and each surface atom has six corrugation values due to its six next neighbors. The values of corrugation for a centered surface atom may differ due to two possible neighboring species (S and Se). Here, the idea is to identify individual Se or S atoms by their six corrugation values.

A histogram of the atomic corrugation values from $TiSe_2$ is shown in Fig. A.4[1]. A lowest limit appears in the distribution at 0.26 Å. Smaller corrugation values are never measured and the lowest value for the corrugation was found at 0.26 Å. A maximum in the number of events can be estimated around 0.35 Å. Indicated by *B* in the figure. At ≈ 0.5 Å the measured distribution approaches zero level.

The open squares in Fig. A.4 represent data points from corrugation values of the mixed phase $TiSe_{1.2}S_{0.8}$. This distribution is remarkably broader than that for the single phase crystal. Corrugation heights between 0.07 Å and 0.7 Å were extracted from the STM topograph. Two peaks named *a* and *b* in the averaged curve can be seen at 0.22 Å and 0.31 Å. Note, the position of the minimum at 0.26 Å between the maxima *a* and *b* is equal to the lowest corrugation value of $TiSe_2$. Assuming that the corrugation from Se –neighbored with Se– in the $TiSe_{1.2}S_{0.8}$ surface layer is not completely different as for the $TiSe_2$ crystal, the corrugation values between 0.26 Å and ≈0.5 Å are tentatively attributed to Se atoms' corrugations with a neighbored Se atom.

The stoichiometric relation from the species can be seen here in the histogram. Overall 286 corrugation heights were measured, and 110 corrugation heights are lower than 0.26 Å and 176 are larger than 0.26 Å. From the given stoichiometric relation, 114.4 number of events related to S and 171.6 numbers of events related to Se were expected. Using this simple approach some questions still remain to be answered. First, values of atomical corrugations larger than 0.5 Å were obtained while the corrugation's distribution of $TiSe_2$ approaches zero around this value. Second, each surface atom has six nearest neighbors and as well six values of atomical

[1]The influence of STM tips on the corrugation is evident since a blunt tip produces a topography with smaller corrugation values than a sharp one. To minimize this influence, just the best STM topographs were taken into account for estimating the corrugations in every case.

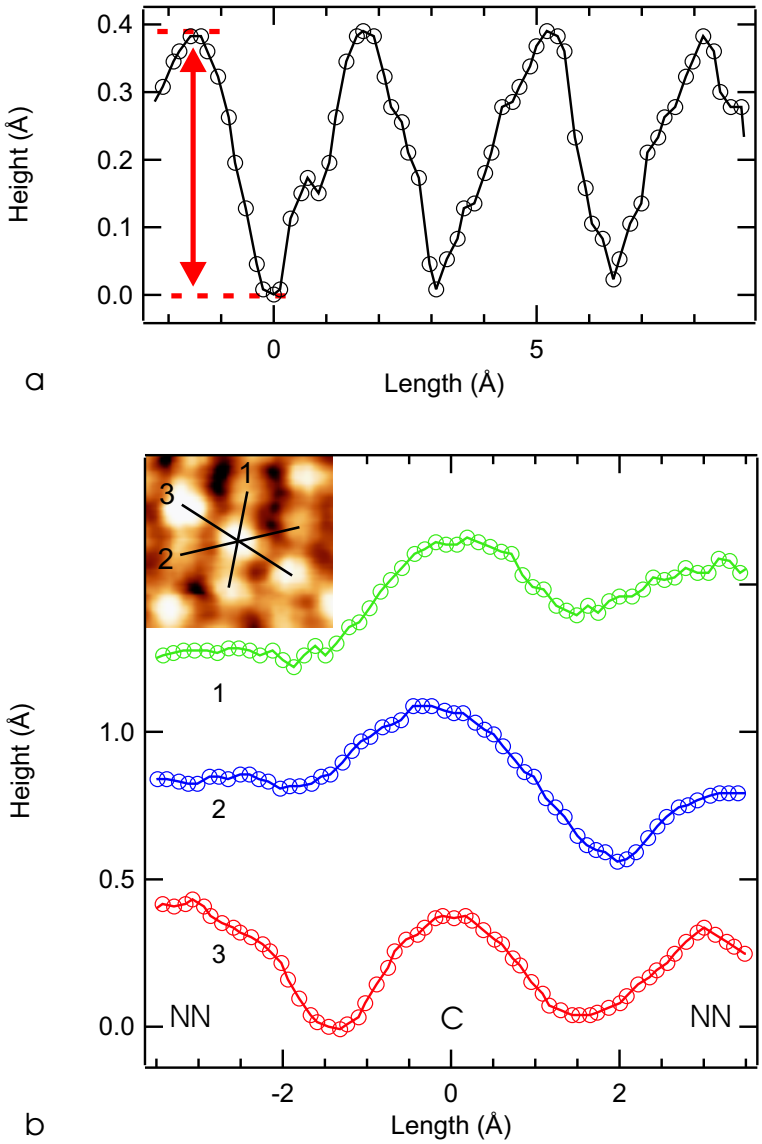

Figure A.3: (a) Cross sectional profile from TiS_2 (taken from Fig. A.1b) along the nearest neighbor directions of the crystal. The image clarifies how the atomic corrugation was estimated. The lengths of the arrow represent the value for the atomic corrugation measured from the top of an atom to its nearest neighbor valley. (b) Three cross sectional profiles from $TiSe_{1.2}S_{0.8}$ surface. The centered atom was denoted by C and the nearest neighbors (NN) with. The positions of the shown profiles are as indicated in the inset. The inset was taken from from the rectangle of Fig. A.2b. From this three profiles all six values of the atomical corrugations of the centered atom can be extracted. (See text). From the corrugation heights, which are all larger than 0.26 Å, the centered atom can be identified as a Se one.

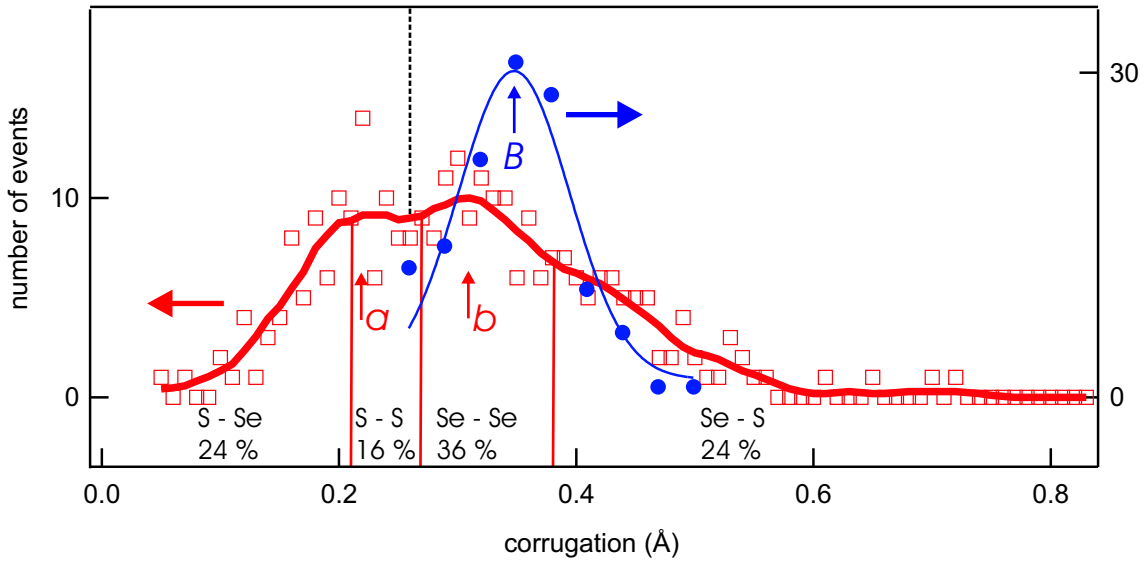

Figure A.4: Histogram of the atomic corrugations. The filled dots are the measured atomic corrugations from $TiSe_2$. Values correspond to the right axis. The thin blue line just guides the eye giving an idea about the distribution of the atomical corrugation. The minimum limit of distribution is marked by the vertical dashed line. A maximum in the number of events can be estimated around 0.35 Å. Indicated by B in the figure. At ≈ 0.5 Å the measured distribution approaches zero level. The open squares represent data points extracted from corrugation values of the mixed phase $TiSe_{1.2}S_{0.8}$. The solid thick line along the data points is an averaged curve from data points. Values correspond to the right axis. Two peaks named a and b within the averaged curve can be seen at 0.22 Å and 0.31 Å. Results from the structural model are shown under zero level of the graph. See text.

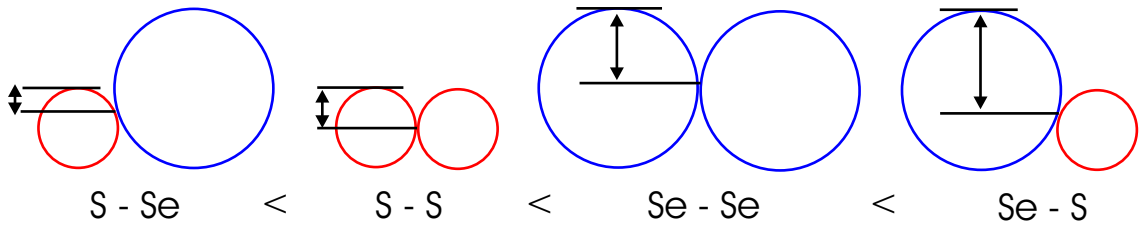

Figure A.5: Sketches of corrugation types with two chemical species (Se and S) as used for model description to explain the histogram of atomical corrugations from $TiSe_{1.2}S_{0.8}$. The S atoms are represented by small circles. Big circles are Se atoms. The Arrow's length represent values of the atomical corrugation. The Se and S system has 4 discrete levels displayed with increasing atomic corrugation, S – Se, S – S, Se – Se and Se – S (from left to right and from small corrugation to large corrugation).

corrugations which may all be different. So how can a chemical identification of an individual surface atom be achieved?

To answer the above mentioned questions a statistical model was used. Some assumptions were necessary for describing: Se atoms are supposed to appear higher in STM topography because S has one electron shell less than Se which can also be seen in the extended in-plane lattice constant of $TiSe_2$ (3.535 Å) compared to TiS_2 (3.4048 Å) [207, 241]. Additionally -as done in Ref. [37]- the Se and S atoms are described by spheres with two discrete diameters. A local even plane on which just two surface atoms are located is only necessary for this model. The assumption of an even surface plane is not necessary and will be wrong due to the measured surface deformations (see Fig. A.2). Four different values of corrugation heights, -namely S–Se, S–S, Se–Se and Se–S can be expected for this model system as shown in Fig. A.5. The combination S–Se has the lowest corrugation while Se–S has the highest one. The nomenclature was chosen in a way that the name of the first species represents the atom to be identified while the second is its nearest neighbor.

Without calculation the model clarifies that corrugation heights larger than 0.5 Å on the mixed phase crystal are measured and contribute to Se–S atom's arrangement. From the stoichiometric relation of S and Se atoms, the statistical frequency of each atomic arrangement can be calculated. A Se atom has six surrounding surface neighbors. From a statistical view 3.6 neighbors are Se atoms as well while 2.4 are S atoms, whereas the probability to have a Se in the center of this arrangement is 0.6. The same calculations can be done for a S center atom. It can be expected that 24 % of all measured corrugation values correspond to S–Se arrangement, 16 % of S–S, 36 % of Se–Se and 24 % of Se–S. The results allow one to separate the histogram in Fig. A.4 into the four types of corrugations due to the above percentage distribution (displayed under the curve). The results of the model confirm that the peak denoted with *b* contributes to Se–Se atoms corrugation. Clear identification of the peak *a* is not possible with the available data. It seems that the differences in the corrugation values for S–Se and S–S are too close to each other for being separated.

Chemical species identification in this special case can be done due to the uniform

behavior of S and Se atoms. Se atoms are identified by its atomic corrugation. In Fig. A.3b three cross sectional profiles along one centered surface atom are displayed. The corresponding six values of corrugation are 0.44 Å and 0.26 Å from profile **1**, 0.27 Å and 0.52 Å from **2**, and 0.38 Å and 0.34 Å from **3** (from left to right). The centered surface atom can be attributed to a Se atom since all six corrugation values are either of Se–Se or Se–S type. From the shown cross sectional profiles the chemical identification of the nearest neighbor atoms is also possible, but for a well-defined surface atom all six values have to indicate one species.

Here the above described model is successful because it disclaims of a global even plane (of Ti atoms) where the surface atoms are arranged. Instead only a local plane is required to define a plane for two nearest neighbor surface atoms to eliminate the surface deformation dependency in the model. The distortions of the Ti layer may result from in plane stress introduced by the different bonding lengths of the S or Se atoms.

Thanks to Prof. Dr. W. Bensch for providing TMDCs crystals.

Appendix B

Molecule powder deposition on Si(100) substrate

For spin effects research in molecules like $Fe(phentroline)_2(NCS)_2$ the preparation of sample surfaces with those molecules is crucial [242, 243]. Since the molecule ($Fe(phentroline)_2(NCS)_2$) is not able to deposit on sample surfaces in UHV with available standard procedures, a new method for molecule preparation in UHV was tested. The motivation for this experiment was just to test the preparation method and not to explain the physical behavior of this molecule on the surface in detail. The packaged molecule powder was put in a supersonic bath for 5 minutes in hope to reduce the grain size of the powder. The idea is to put a small visible amount of the molecule powder, which is of purple color, on a horizontally held sample. By rotating the sample, the overrun material will fall off the sample due to gravitational force. By shaking the sample carefully with a transfer rod, some more molecules fall off. This is done with a clean and heated (2×1)–Si(100) surface checked with STM previously. The STM topographs of this single preparation were shown in Figs. B.1a,b,c. The molecule distribution on the sample surface -as one can expect- is not as uniform as known from standard deposition methods. There are areas covered with small grains ($\approx$ 2000 Å in diameter) of $Fe(phentroline)_2(NCS)_2$ molecules, see Fig. B.1a. Other areas are covered with $Fe(phentroline)_2(NCS)_2$ molecules of different coverage. In Fig. B.1b an arrangement of the molecules was found, which could not analyzed in detail, but single $Fe(phentroline)_2(NCS)_2$ molecules can be identified by their size of (10 $\pm$2) Å × (6 $\pm$ 1) Å. The dimensions of a single molecule are estimated from areas with low coverage below one closed monolayer (Fig. B.1c). Here the $Fe(phentroline)_2(NCS)_2$ molecules appear slightly larger with (12 $\pm$ 1) Å × (6 $\pm$ 1) Å in size, located along the dimer rows. In this low coverage areas still the (2×1) reconstruction is present, but partly the dimers are broken and individual Si surface atoms were monitored. Since our interest was to monitor individual molecules the test was successfully. One advantage using this method may be that different coverages of molecules can be found. Another advantage is that it is easy to perform. By careful heating of the sample without destroying the molecule, the growth of ordered layers may be favored. Here -if needed- extra research will be still necessary. Thanks to Prof. Dr. F. Tuczek for providing the molecule.

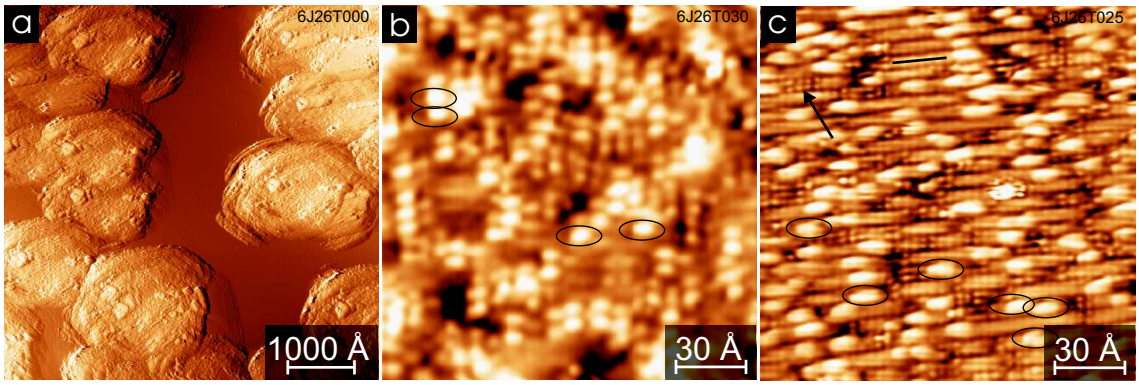

Figure B.1: (a) STM topograph shows grains of Fe(phentroline)$_2$(NCS)$_2$ molecules. Since flat areas from the substrate between the grains are visible, it may be possible to achieve with this preparation method having the surface covered locally with one "monolayer" of grains. The height of those is around 200 Å. (2,5 V; 88 pA). (b) Since the coverage was not constant over the entire surface, an area was found where a structure was observed attributed to individual Fe(phentroline)$_2$(NCS)$_2$ molecules (inside ellipses). (1,42 V; 194 pA). (c) Area with molecule coverage lower than a closed monolayer. The dimer lines of the (2×1) Si reconstruction are visible. Direction of the dimer lines is along the black line. Partially the dimer rows are broken and individual Si surface atoms appear. Arrow points on single Si surface atom. Ellipses contain smallest observed structure attributed to individual Fe(phentroline)$_2$(NCS)$_2$ molecule. (1,35 V; 240 pA).

List of Figures

2.1 The tunneling effect . . . 8
2.2 Energy levels in tunneling process . . . 10
2.3 Two modes of STM scanning . . . 11
2.4 Drift analysis . . . 13
2.5 z-drift correction . . . 13

3.1 Radiation from inelastic tunneling . . . 16
3.2 Radiative processes in direct semiconductors . . . 17
3.3 Types of radiative transitions in Silicon . . . 19
3.4 Light emission spectra from MOS structure . . . 19

4.1 Technical drawing of LT-STM apparatus . . . 22
4.2 Technical drawing of RT-STM apparatus . . . 22
4.3 Technical drawing of the STM . . . 23
4.4 Recording setup for optical spectra . . . 24
4.5 Transmission of the optical setup . . . 25

5.1 Sample holders for TMDCs . . . 27
5.2 Tool for re-cleaving TMDCs . . . 27
5.3 Silicon sample holder . . . 28

6.1 Brillouin zone of silicon and direct optical transitions . . . 31
6.2 STM image of Si(100) and Si(111) . . . 32

7.1 Luminescence spectra recorded from *p*-Si(111). . . . 35
7.2 Luminescence spectra from *n*-Si. . . . 36
7.3 Processes for STM-induced light emission for electron injection. . . . 38
7.4 Processes for STM-induced light emission for electron extraction. . . . 39

8.1 External quantum efficiency of emitted light from silicon . . . 43

9.1 Individual C_{60} molecules on *n*-Si(100) . . . 47
9.2 C_{60} on *n*-Si(100) . . . 49
9.3 Heights of C_{60} clusters on *n*-Si(100) . . . 50

10.1 Spectra from the C_{60}-*n*-Si(100) sample . . . 53
10.2 Spectra from the C_{60}-*n*-Si(100) sample . . . 55
10.3 Quantum well states of *n*-Si(100) . . . 58

11.1 Sketch of two adjacent layers of $1T$-TaS_2 63
11.2 STM images of (Rb–)TaS_2 at 7 K 64
11.3 STM images of (Rb–)TaS_2 at RT 65
11.4 Model of intercalation 67

12.1 CDW on Rb-TaS_2. 72
12.2 dI/dV of Rb-TaS_2. 73
12.3 Nanostructures network on Rb–TaS_2 75

A.1 STM image of $TiSe_2$ 80
A.2 STM image of $TiSe_{1.2}S_{0.8}$ 80
A.3 Atomical corrugation of TiS_2 and $TiSe_1.2S_{0.8}$ 82
A.4 Histogram of atomical corrugation of TiS_2 and $TiSe_{1.2}S_{0.8}$ 83
A.5 Sketches of model atoms 84

B.1 Fe(phentroline)$_2$(NCS)$_2$ molecules on Si(100) 87

Appendix C

List of abbreviations

TMDC	Transition Metal Dichalcogenite
ARPES	Angle Resolved Photon Emission Spectroscopy
APUPS	Angle Resolved Ultraviolet Photon Spectroscopy
c-c	Conduction band to Conduction band
CDW	Charge Density Wave
c-v	Conduction band to Valence band
DOS	Density of States
HSB	Hole-jSubband
HREELS	High-Resolution Energy Electron Loss Spectroscopy
IPES	Inverse Photon Emission Spectroscopy
LDOS	Local Density of States
LEED	Low Energy Electron Diffraction
LT	Low Temperature
LT–STM	Low Temperature Scanning Tunneling Microscope
MIM	Metal Insulator Metal
MIS	Metal Insulator Semiconductor
ML	Monolayer
MOS	Metal Oxide Semiconductor
MOSFET	Metal Oxide Semiconductor Field Emission Transistor
PES	Photon Emission Spectroscopy
RT–STM	Room Temperature Scanning Tunneling Microscope
STM	Scanning Tunneling Microscope
UHV	Ultra-High Vacuum

Appendix D

Thanks and Acknowledgements

Thanks to Prof. Richard Berndt for offering me the possibility to study in his excellent working group. He guided me during this work and gave helpful advice.

Second, I will say thanks to Dr. Jörg Kröger and Dr. Bridget Murphy who always have a minute left to listen to my ideas for solving physical problems. I really thank you both for your unique help for writing the publications and for your proofreading large parts of this thesis.

I will thank Dr. Guillaume Schull for proofreading parts of this text.

I will also say thanks to Dr Thomas Jürgens who has built the room temperature scanning tunneling microscope. He always has always a helping hand for solving problems in the laboratory.

I am thankful to all the other group members for advice, help and talks.

Many thanks are addressed to Mikhail Vexler from the A. F. Ioffe Physicotechnical Institute, St. Petersburg, Russia. He has performed the calculations of the band bending.

Further theoretical support was given by Peter Johansson from the Department of Natural Sciences, University of Örebro, Sweden.

Advice and transition metal dichalcogenide crystals were spend by Prof. Dr. Lutz Kipp and his collaborators.

I would like to say thanks to all my friends. They will know why. A special thanks to Prof. Dr. Volkmar Helbig and his "fellows" Dr. Daniel Esch and Dr. Ingo Grothkopp. In this context: thanks to all working coffee machines around the physics department but especially to *Jura Impressa F70* in our "Wasseraufbereitung".

Thanks to Jesko Banck for proofreading this work and for your private lessons on the English language.

Ein riesiges Dankeschön an meine Eltern Udo und Sylvia Schmidt, die mich immer in allen Lebenslagen unterstützten. Ich bin stolz auf Euch.

Thanks to my girlfriend Anne who supported me during the last years of my work.

Lebenslauf

Name:	Schmidt
Vorname:	Patrick
Geburtsdatum:	9. März 1973
Geburtsort:	Koblenz
Staatsangehörigkeit:	deutsch
Familienstand:	ledig, ein Sohn
1979 - 1981	Grundschule Koblenz-Moselweiß
1981 - 1983	Grundschule Siershahn
1983 - 1985	Fürst-Johann-Ludwig-Schule Hadamar, Realschulzweig
1985 - 1993	Fürst-Johann-Ludwig-Schule Hadamar, Gymnasialzweig
1993	Abitur
Oktober 1993 - Dezember 1994	Zivildienst beim Deutschen Roten Kreuz in Montabaur
April 1995 - September 1995	Beginn des Studiums an der Universität Köln.
Oktober 1995	Beginn des Ozeanographiestudiums an der CAU Kiel.
Februar 1998	Vordiplom in Ozeanographie.
Oktober 1998	Studienfachwechsel zu Physik.
Februar 2003	Diplom in Physik.
März 2003	Beginn der Promotion an der CAU

Eidesstattliche Erklärung

Hiermit erkläre ich an Eides Statt, dass ich diese Arbeit selbständig unter der Beratung meiner wissenschaftlichen Lehrer und nur mit den angegebenen Hilfsmitteln erstellt habe. Diese Arbeit wurde weder ganz noch in Teilen an anderer Stelle im Rahmen eines Prüfungsverfahrens vorgelegt. Frühere Promotionsversuche wurden von mir nicht vorgenommen.

Kiel, den

Bibliography

[1] G. Binnig, H. Rohrer, Ch. Gerber, and E. Weibel, Phys. Rev. Lett. **50**, 120 (1983).

[2] X. Lu, M. Grobis, K. H. Khoo, S. G. Louie, and M. F. Crommie, Phys. Rev. Lett. **90**, 96802 (2003).

[3] J. K. Gimzewski, B. Reihl, J. H. Coombs, and R. R. Schliter, Z. Phys. B: Condens. Matter **72**, 497-501 (1988).

[4] D. L. Abraham, A. Veider, Ch. Schöneberger, H. P. Meier, D. J. Arent, and S. F. Alvarado, Appl. Phys. Lett. **56**, 1564 (1990).

[5] R. Berndt, R. Gaisch, W. D. Schneider, J. K. Gimzewski, B. Reihl, R. R. Schlitter, and M. Tschudy, Phys. Rev. Lett. **74**, 102 (1995).

[6] N. Asli, *Experimentelle Untersuchungen der Electrolumineszenz von MOS-Tunnelstrukturen*, Ph.D. thesis, Christian-Albrechts-Universtät zu Kiel, 2003.

[7] J. Bude, K. Hess, and G. J. Iafrade, Phys. Rev. B **45**, 10958 (1992).

[8] P. D. Yoder, M. I. Vexler, A. F. Shulekin, N. Asli, S. V. Gastev, I. V. Grekhof, P. Seegebrecht, S. E. Tyaginov, and H. Zimmermann, J. Appl. Phys. **98**, 83511 (2005).

[9] J. Bude, N. Sano, and A. Yoshii, Phys. Rev. B **45**, 5848 (1992).

[10] M. I. Vexler, A. F. Shulekin, S. A. Solov'ev, A. G. Tkachenko, and A. F. Shulekin, Tech. Phys. Lett. **21**, 530 (1995).

[11] M. Pavesi, P. L. Rigolli, M. Manfredi, P. Palestri, and L. Selmi, Phys. Rev. Lett. **65**, 195209 (2002).

[12] A. Gustafsson, M.-E. Pistol, L. Montelius, and L. Samuelson, J. Appl. Phys. **84**, 1715-1775 (1998).

[13] C. Thirstrup, M. Sakurai, K. Stokbro, and M. Aono, Phys. Rev. Lett. **82**, 1241 (1999).

[14] M. Sakurai, C. Thirstrup, and M. Aono, Phys. Rev. Lett. **93**, 46102 (2004).

[15] A. Downes and M. E. Welland, Phys. Rev. Lett. **81**, 1857 (1998).

[16] R. Berndt, J. K. Gimzewski, and P. Johansson, Phys. Rev. Lett. **67**, 3796 (1991).

[17] F. Stern, Phys. Rev. **5**, 4891 (1972).

[18] K. von Klitzing, G. Landwehr, and G. Dorda, Sol. State Comm. **14**, 387 (1974).

[19] K. von Klitzing, G. Landwehr, and G. Dorda, Sol. State Comm. **15**, 489 (1974).

[20] T. Neugebauer, K. von Klitzing, G. Landwehr, and G. Dorda, Sol. State Comm. **17**, 295 (1975).

[21] J. P. Kotthaus and R. Ranvaud, Phys. Rev. B **15**, 5758 (1977).

[22] U. Gennser, V. P. Kesan, D. A. Syphers, T. P. Smith, III, S. S. Iyer, and E. S. Yang, Phys. Rev. Lett. **67**, 3828 (1991).

[23] L. Rapoport, Y. Bilik, Y. Feldman, M. Homyonfer, S. R. Cohen, and R. Tenne, Nature (London) **387**, 791 (1997).

[24] M. S. Whittingham, Science **192**, 1126 (1976).

[25] H. Tributsch, Faraday Discuss. Chem. Soc. **70**, 189 (1980).

[26] V. Grasso, *Electronic Structure and Electronic Transitions in Layered Materials*, Reidel Publishing Company, Dordrecht (1986).

[27] J. A. Wilson, F. J. DiSalvo, and S. Mahajan Adv. Phys. **24**, 117 (1975).

[28] H. I. Starnberg, H. E. Brauer, L. J. Holleboom, and H. P. Hughes, Phys. Rev. Lett. **70**, 3111 (1993).

[29] C. Pettenkofer and W. Jaegermann, Phys. Rev. B **50**, 8816 (1994).

[30] K. Rossnagel, E. Rotenberg, H. Koh, N. V. Smith, and L. Kipp, Phys. Rev. Lett. **95**, 126403 (2005).

[31] R. Adelung, J. Brandt, L. Kipp, and M. Skibowski, Phys. Rev. B **63**, 165327 (2001).

[32] R. Adelung, J. Brandt, K. Rossnagel, O. Seifarth, L. Kipp, M. Skibowski, C. Ramírez, T. Strasser, and W. Schattke, Phys. Rev. Lett. **86**, 1303 (2001).

[33] R. Adelung, L. Kipp, J. Brandt, L. Tarcak, M. Traving, C. Kreis, and M. Skibowski, Appl. Phys. Lett. **74**, 3053 (1999).

[34] A. Spijkerman, J. L. de Boer, A. Meetsma, and G. A. Wiegers, Phys. Rev. B **56**, 13757 (1997).

[35] P. Schmidt and R. Berndt, Phys. Rev. Lett. **99**, 246103 (2007).

[36] P. Schmidt, J. Kröger, B. Murphy, and R. Berndt, New Journal of Physics **10**, 13022 (2008).

[37] P. Schmidt, B. Murphy, J. Kröger, H. Jensen, and R. Berndt, Phys. Rev. B **74** 193407 (2006).

[38] F. Schwabel, *Quantenmechanik*, Springer Verlag, Berlin, 1998.

[39] Th. von Hofe, *Electron Dynamics of Cs covered Cu(111): A Scanning tunneling Spectroscopy Investigation at Low temperatures*, Ph.D. thesis, Christian-Albrechts-Universtät zu Kiel, 2005.

[40] J. Tersoff and D. R. Hamann, Phys. Rev. Lett. **50**, 1998 (1983).

[41] J. Tersoff and D. R. Hamann, Phys. Rev. B **31**, 805 (1985).

[42] N. D. Lang, Phys. Rev. B **34**, 5947 (1986).

[43] Thomas Jürgens, *Aufbau und Test eines Raumtemperatur-Ultrahochvakuum-Rastertunnelmikroskops*, Ph.D. thesis, Christian-Albrechts-Universtät zu Kiel, 2003.

[44] F. Calleja, A. Arnau, J. J. Hinarejos, A. L. Vázquez de Parga, W. A. Hofer, P. M. Echenique, and R. Miranda, Phys. Rev. Lett **92**, 206101 (2004).

[45] N. D. Lang, Phys. Rev. Lett. **58**, 45 (1987).

[46] G. Binnig and H. Rohrer, Phys. Rev. Mod. **59**, 615 (1987).

[47] D. Bonnell (Ed.), *Scanning probe Microscopy and Spectroscopy*, Wiley-VCH, New York, 2001.

[48] A. M. Russell and D. A. Torchia, Rev. Sci. Instrum. **33**, 442 (1962).

[49] M. L. Meade, *Lock-in amplifiers: principles and applications*. Peter Peregrinus Ltd., London, 1983.

[50] H. Jensen, *Zusammenbau eines Rastertunnelicroskops und erste Messungen an einkristallinen Metalloberflächen*, Diploma thesis, Christian-Albrechts-Universtät zu Kiel, 2003.

[51] C. J. Chen, *Introduction to Scanning Tunneling Microscopy*, Oxford University Press, New York (1993).

[52] G. V. H. Wilson, J. Appl. Phys. **34**, 3276 (1963).

[53] J. Lambe and S. L. McCarthy, Phys. Rev. Lett. **37**, 923 (1976).

[54] A. Adams, J. C. Wyss, and P. K. Hansma, Phys. Rev. Lett. **42**, 912 (1979).

[55] B. Laks and D. L. Mills, Phys. Rev. B **20**, 4962 (1979).

[56] P. Johansson, R. Monreal, and P. Apell, Phys. Rev. B **42**, 9210 (1990).

[57] B. N. Persson and A. Baratoff, Phys. Rev. Lett. **68**, 3224 (1992).

[58] R. Berndt, J. K. Gimzewski, and P. Johansson, Phys. Rev. Lett. **71**, 3493 (1993).

[59] P. Johansson, Phys. Rev. Lett. **58**, 10823 (1998).

[60] K. Meguro, K. Sakamoto, R. Arafune, M. Satoh, and S. Ushioda, Phys. Rev. B **65**, 165405 (2002).

[61] R. Berndt and J. K. Gimzewski, Phys. Rev. B **48**, 4746 (1993).

[62] A. W. McKinnon, M. E. Welland, T. M. H. Wong, and J. K. Gimzewski, Phys. Rev. B **48**, 15250 (1993).

[63] Ph. Dumas, M. Gu, C. Syrykh, A. Hallimaoui, F. Salvan, J. K. Gimzewski, and R. R. Schlitter, J. Vac. Technol. B **12(3)**, 2064 (1994).

[64] K. I. Ohyama, Y. Uehara, and S. Ushioda, Appl. Phys. Lett. **67**, 2536 (1995).

[65] M. Sakurai and M. Aono, Phys. Rev. B **64**, 45402 (2001).

[66] G. Hoffmann, L. Libioulle, and R. Berndt, Phys. Rev. B **65**, 212107 (2002).

[67] F. Silly, A. O.Gusev, A. Taleb, F. Charra, and M.-P. Pileni, Phys. Rev. Lett. **84**, 5840 (2000).

[68] D. Fujita, K. Onishi, and N. Niori, Nanotechnology **15**, 355-361 (2004).

[69] G. Hoffmann, Th. Maroutian, and R. Berndt, Phys. Rev. Lett. **93**, 76102 (2004).

[70] G. Hoffmann, J. Kliewer, and R. Berndt, Phys. Rev. Lett. **87**, 176803 (2001).

[71] X. H. Qiu, G. V. Nazin, and W. Ho, Science **299**, 542 (2003).

[72] D. Fujita, T. Ohgi, W.-L. Deng, K. Ishige, T. Okamoto, S. Yokohama, T. Kamikado, S. Mashiko, Surf. Sci. **493**, 702-707 (2001).

[73] Z. C. Dong, X. L. Guo, A. S. Trifonov, P. S. Dorozhkin, K. Miki, K. Kimura, S. Yokohama, and S. Mashito, Phys. Rev. Lett. **92**, 86801 (2004).

[74] E. Ćavar, M.-Chr. Blüm, M. Pivetta, F. Patthey, M. Chergui, and W.-D. Schneider, Phys. Rev. Lett. **95**, 196102 (2005).

[75] H. Liu, Y. Ie, T. Yoshinobu, Y. Aso, and H. Iwasaki, Appl. Phys. Lett. **88**, 61901 (2006).

[76] H. Liu, Y. Ie, R. Nishitani,, Y. Aso, and H. Iwasaki, Phys. Rev. B **75**, 115429 (2007).

[77] T. Tsuruoka, Y. Ohizumi, R. Tanimoto, and S. Ushioda, Appl. Phys. Lett. **75**, 2289 (1999).

[78] Ph. Dumas, V. Derycke, R. Houdré, P. Guaino, and A. Downes, Appl. Phys. Lett. **77**, 3992 (2000).

[79] R. Berndt and J. K. Gimzewski, Phys. Rev. B **45**, 14095 (1992).

[80] Ph. Renaud and S. A. Alvarado, Phys. Rev. B **44**, 6340 (1991).

[81] T. Murashita, J. Vac. Sci. Technol. B **15**, 32 (1997).

[82] T. Yokoyama and Y. Takiguchi, Surf. Sci. **482-485**, 1163 (2001).

[83] M. Kemerink, K. Sauthoff, P. M. Koenraad, J. W. Gerritsen, H. van Kempen, and J. H. Wolter, Phys. Rev. Lett. **86**, 2404 (2001).

[84] L. Montelius, M.-E. Pistol, and L. Samuelson, Ultramicroscopy **42-44**, 210 (1992).

[85] S. F. Alvarado, Ph. Renaud, D. L. Abraham, C. Schönenberger, D. J. Arent, and H. P. Meier, J. Vac. Sci. Technol. B **9**, 409 (1991).

[86] I. Appelbaum, W. Yi, K. J. Russell, V. Narayanamurti, M. P. Hanson, and A. C. Gossard, Appl. Phys. Lett. **86**, 063110 (2005).

[87] F. Buda, J. Kohanoff, and M. Parrinello, Phys. Rev. Lett. **69**, 1272 (1992).

[88] J. P. Proot, C. Delerue, and G. Allan, Appl. Phys. Lett. **61**, 1948 (1992).

[89] S. Ushioda, J. Electr. Spectr. Rel. Phenom. **109**, 169 (2000).

[90] A. G. Cullis, L. T. Canham, and P. D. J. Calcott, Appl. Phys. Rev. **82**, 909 (1997).

[91] M. Enachescu, E. Hartmnn, A. Kux, and F. Koch, J. Lumin. **57**, 191 (1993).

[92] M. Gu, C. Syrykh, A. Halimaoui, Ph. Dumas, and F. Salvan, J. Lumin. **57**, 315 (1993).

[93] Ph. Dumas, M. Gu, C. Syrykh, J. K. Gimzewski, I. Makarenko, A. Halimaoui, and F. Salvan, Europhys. Lett. **23**, 197 (1993).

[94] K. Ito, S. Ohyama, Y. Uehara, and S. Ushioda, Surf. Sci. **363**, 423 (1996).

[95] B. Delley and E. F. Steigmeier, Phys. Rev. B **47**, 1397 (1993).

[96] M. Kemerinka, J. W. Gerritsen, J. G. H. Hermsen, H. Van Kempen, and J. H. Wolter, Rev. Sci. Instrum. **72**, 132 (2001).

[97] G. Hoffmann, J. Kröger, and R. Berndt, Rev. Sci. Intrum. **73**, 305 (2002).

[98] N. J. Watkins, J. P. Long, Z. H. Kafafi, and A. J. Mäkinen, Rev. Sci. Instrum. **78**, 53707 (2007).

[99] A. J. Forsyth, A. E. Smith, and T. W. Josefsson, Surf. Sci. **357-258**, 270 (1996).

[100] R. Losio, K. N. Altmann, and F. J. Himpsel, Phys. Rev. B **61**, 10845 (2000).

[101] R. Schillinger, C. Bromberger, H. J. Hänsch, H. Kleine, O. Kühlert, C. Weindel, and D. Fick, Phys. Rev. B **72**, 115314 (2005).

[102] I. Barke, F. Zheng, A. R. Konicek, R. C. Hatch, and F. J. Himpsel, Phys. Rev. Lett. **96**, 216801 (2006).

[103] J. W. Wells, J. F. Kallehauge, T. M. Hansen, and Ph. Hoffmann, Phys. Rev. Lett. **97**, 206803 (2006).

[104] J. W. Wells, *A combined study of the elctronic structure and transport properties of surfaces*, Ph. D. thesis, University of Aarhus, Denmark (2006).

[105] T. Figielski and A. Torum, *On the origin of light emitted from reverse-biased p-n-junctions*, Int. Conf. Phys. Semicond., Pergamon London, 863-868 (1992).

[106] A. Toriumi, M. Yoshimi, M. Iwase, Y. Akiyama, and K. Taniguchi, IEEE Transactions on Electron Devices **34**, 1501 (1987).

[107] K. Kobayashi, A. Teramoto, M. Hirayama, and Y. Fujita, J. Appl. Phys. **77**, (1995).

[108] Private Communication.

[109] G. Hoffmann, *Light emission from Metals and Adsorbates in the Scanning Tunneling Microscope*, Ph.D. thesis, Christian-Albrechts-Universtät zu Kiel, 2001.

[110] P. Schmidt, *Nachweisoptiken für Licht aus Rastertunnelexperimenten*, Diploma thesis, Christian-Albrechts-Universtät zu Kiel, 2002.

[111] O. Madelung, *Semiconductor-Basic Data*, Springer Berlin, (1996).

[112] Ch. Kittel, *Einführung in die Festkörperphysik*, R. Oldenbourg Verlag München Wien, 12. Auflage, 1999.

[113] S. M. Sze, *Semiconductor Devices, Physics and Technology*, John Wiley & Sons New York, 1985.

[114] We use the notation from O. Madelung, *Semiconductor-Basic Data*, (Springer, Berlin, 1996).

[115] W. Bludau, A. Onton, W. Heinke, J. Appl. Phys **45**, 1846 (1974).

[116] D. E. Aspnes, A. A. Studna, Solid State Commum. **11**, 1375 (1972).

[117] G. Grosso and C. Piermarocchi, Phys. Rev. B **51**, 16772 (1995).

[118] Y. B. Zhao, D. M. Poirier, R. J. Pechmann, and J. H. Weaver, Appl. Phys. Lett. **64**, 577 (1994).

[119] M. Rohlfing, P. Krüger, and J. Pollmann, Phys. Rev. B **48**, 17791 (1993).

[120] T. B. Boykin, G. Klimek, and F. Oyafuso, Phys. Rev. B **69**, 115201 (2004).

[121] R. I. G. Uhrberg, G. V. Hansson, J. M. Nicholls, and S. A. Flodström, Phys. Ref. B **24**, 4684 (1981).

[122] R. I. G. Uhrberg, G. V. Hansson, U. O. Karlsson, J. M. Nicholls, P. E. S. Persson, S. A. Flodström, R. Engelhardt, and E.-E Koch, Phys. Rev. B **31**, 3795 (1985).

[123] D. Straub, L. Ley, and F. J. Himpsel, Phys. Rev. Lett. **45**, 142 (1985).

[124] A. L. Wachs, T. Miller, T. C. Hsieh, A. P. Shapiro, and T.-C. Chiang, Phys. Rev. B **32**, 2326 (1985).

[125] L. S. O. Johansson, P. E. S. Persson, U. O. Karlsson, and R. I. G. Uhrberg, Phys. Rev. B **42**, 8991 (1990).

[126] L. S. O. Johansson, R. I. G. Uhrberg, P. Mårtensson, and G. V. Hansson, Phys. Rev. B **42**, 1305 (1990).

[127] Y. He, S. Bouzidi, B.-Y Han, L.-M. Yu, P. A. Thiry, R. Caudano, and J.-M. Debever, Phys. Rev. B **54**, 17654 (1996).

[128] J. E. Ortega and F. J. Himpsel, Phys. Rev. B **47**, 2130 (1993).

[129] K. Kondo, A. Moretani, Nuovo Cimento **39 B**, 387 (1977).

[130] A. Daunois, D. E. Aspnes, Phys. Rev. B **18**, 1824 (1978).

[131] R. R. L. Zucca, Y. R. Shen, Phys. Rev. B **1**, 2668 (1970).

[132] G. E. Jellison, F. A. Modine, Phys. Rev. B **27**, 7466 (1983).

[133] H. Ibach, H. Lüth, *Festkörperphysik*, Springer Verlag, Berlin, S. 269 (1990).

[134] R. M. Tromp, R. J. Hamers, and J. E. Demuth, Phys. Rev. Lett. **55**, 1303 (1985).

[135] R. A. Wolkow, Phys. Rev. Lett. **68**, 2636 (1992).

[136] J. E. Northrup, Phys. Rev. B **47**, 10032 (1993).

[137] A. Ramstadt, G. Brocks, and P. J. Kelly, Phys. Rev. B **51**, 14504 (1995).

[138] P. Krüger, J. Pollmann, Phys. Rev. Lett. **74**, 1155 (1995).

[139] M. Dubois, P. Perdigão, C. Delerue, G. Allan, B. Grandidier, D. Deresmes, and D. Stiévenard, Phys. Rev. B **71**, 165322 (2005).

[140] F. J. Himpsel and D. E. Eastman, J. Vac. Sci. Technol. **16**, 1297 (1979).

[141] Y. Enta, S. Suzuki, and S. Kono, Phys. Rev. Lett. **65**, 2704 (1990).

[142] L. S. O. Johansson and B. Reihl, Surf. Sci. **269/270**, 810 (1992).

[143] K. Nagaoka, M. J. Comstock, A. Hammack, and M. F. Crommie, Phys. Rev. B **71**, 121304 (2005).

[144] R. E. Schlier and H. E. Farnswoth, J. Chem. Phys. **30**, 917 (1959).

[145] K. Takanayagi, Y. Tanishiro, S. Takahashi, and M. Takahashi, Surf. Sci. **164**, 367 (1985).

[146] K. Takayanagi, Y. Tanishiro, M. Takahashi, and s. Takahashi, J. Vac. Sci. Technol. A **3**, 1502 (1985).

[147] R. I. G. Uhrberg, G. V. Hansson, J. M. Nicholls, P. E. S. Persson, and S. A. Flodström, Phys. Rev. B **31**, 3805 (1985).

[148] J. E. Demuth, W. J. Thomson, N. J. DiNardo, and R. Imbihl, Phys. Rev. Lett **56**, 1408 (1986).

[149] P. Martensson, W.-X. Ni, G. V. Hansson, J. M. Nicholls, and B. Reihl, Phys. Rev. B **36**, 5974 (1987).

[150] R. Losio, K. N. Altmann, and F. J. Himpsel, Phys. Rev. B **61**, 10845 (2000).

[151] F. J. Fauster, J. Vac. Sci. Technol. A **2**, 815 (1984).

[152] J. M. Nicholls and B. Reihl, Phys. Rev. B **36**, 8071 (1987).

[153] F. J. Himpsel, Surf. Sci. Reports. **12**, 3 (1990).

[154] U. Backes and H. Ibach, Solid State Communications **49**, 575 (1981).

[155] R. Schillinger, C. Bromberger, H. J. Hänsch, H. Kleine, O. Kühlert, C. Weindel, and D. Fick, Phys. Rev. B **72**, 115314 (2005).

[156] J. R. Haynes and W. C. Westphal, Phys. Rev. **101** , 1676 (1956).

[157] W. P. Dumke, Phys. Rev. **105** , 139 (1957).

[158] S. Villa, A. L. Lacaita, and A. Pacelli, Phys. Rev. B **52**, 10993 (1995).

[159] E. Cartier, J. C. Tsang, M. V. Fischetti, and D. A. Buchanan, Microelectron. Eng. **36**, 103 (1997).

[160] D. Brust, M. L. Cohen, and J. C. Phillips, Phys. Rev. Lett. **9**, 389 (1962).

[161] C. Chang, C. Hu, and R. W. Brodersen, J. Appl. Phys. **57**, 302 (1985).

[162] I. V. Grekhov, A. F. Shulekin, and M. I. Vexler, J. Phys. Condens. Matter **7**, 7037 (1995).

[163] R. M. Feenstra and Joseph A. Stroscio, J. Vac. Sci. Technol. B **5**, 923-929 (1987).

[164] N. Néel, J. Kröger, L. Limot, T. Frederiksen, M. Brandbyge, and R. Berndt, Phys. Rev. Lett. **98**, 065502 (2007).

[165] N. Néel, L. Limot, J. Kröger, and R. Berndt, Phys. Rev. B **77**, 125431 (2008).

[166] P. Moriarty, Y. R. Ma, M. D. Upward, and P. H. Beton, Surf. Sci. **407**, 27 (1998).

[167] D. Chen and D. Sarid, Surf. Sci. **329**, 206 (1995).

[168] X. Yao, R. K. Workman, C. A. Peterson, D. Chen, and D. Sarid, Appl. Phys. A **66**, 107 (1998).

[169] D. Frohlich, M. Haselhoff, K. Reimann, T. Itoh, D. Sarid, and D. Chen, Surf. Sci. **329**, 206 (1995).

[170] D. Sarid, X. Yao, T. G. Ruskell, R. K. Workman, and D. Chen, Surf. Sci. **367**, 85 (1996).

[171] S. Suto, K. Sakamoto, T. Wakita, Ch.-W. Hu, and A. Kasuya, Phys. Rev. B **56**, 7439 (1997).

[172] K. Sakamoto, D. Kondo, Y. Ushimi, M. Harada, A. Kimura, A. Kakizaki, and S. Suto, Phys. Rev. B **60**, 2579 (1999).

[173] M. De Seta, D. Sanvitto, and F. Evangelisti, Phys. Rev. B **59**, 9878 (1999).

[174] D. L. Keeling, M. J. Humphry, R. H. J. Beton, C. Hobbs, and L. Kantorovich, Phys. Rev. Lett **94**, 146104 (2005).

[175] N. Martsinovich, C. Hobbs, L. Kantrorovich, R. H. J. Fawcett, M. J. Humphry, D. L. Keeling, and P. H. Beton, Phys. Rev. B **74**, 85304 (2006).

[176] A. W. Dunn, E. D. Svensson, and C. Dekker, Surf. Sci. **498**, 237 (2002).

[177] SAES Getters, Cologne, Germany.

[178] G. Schull and R. Berndt, Phys. Rev. Lett. **99**, 226105 (2007).

[179] Ryo Nouchi, Kosuke Masunari, Toshio Ohta, Yoshihiro Kubozono, and Yoshihiro Iwasa, Phys. Rev. Lett. **97**, 196101 (2006).

[180] P. Lautenschlager, M. Garriga, L. Viña, and M. Cardona, Phys. Rev. B **36**, 4821 (1987).

[181] T. Aoki and S. Adachi, J. Appl. Phys. **69**, 1574 (1991).

[182] T. Miyazaki and S. Adachi, J. Appl. Phys. **77**, 1741 (1995).

[183] M. Cardona, K. L. Shaklee, and F. H. Pollak, Phys. Rev **154**, 696 (1967).

[184] K. Kondo and A. Moriatini, Phys. Rev. B **14**, 1577 (1976).

[185] J. W. Grover and P. Handler, Phys. Rev. B **9**, 2600 (1974).

[186] S. N. Takeda, N. Higashi, and H. Daimon, Phys. Rev. Lett. **94**, 37401 (2005).

[187] C. Moglestute, J. Appl. Phys. **59**, 3175 (1986).

[188] B. C. Cyca, K. G. Robins, N. G. Tarr, D. X. Xu, J.-P. Noel, D. Landheer, and M. Simard-Normandin, J. Appl. Phys. **81**, 8079 (1997).

[189] S. Rodríguez, J. A. López-Villanueva, I. Melchor, and J. E. Carceller, J. Appl. Phys. **86**, 438 (1999).

[190] R. K. Hayden, D. K. Maude, L. Eaves, E. C. Valadares, M. Henini, F. W. Sheard, O. H. Hughes, J. C. Portal, L. Cury, Phys. Rev. Lett. **66**, 1749 (1991).

[191] G. Fasol and H. P. Hughes, Phys. Rev. B **33**, 2953 (1986).

[192] L. W. Molenkamp, R. Eppenga, G. W. 't Hooft, P. Dawson, C. T. Foxon, and K. J. Moore, Phys. Rev. B **38**, 4314 (1988)

[193] J. A. Kash, M. Zachau, M. A. Tischler, U. Ekenberg, Phys. Rev. Lett. **69**, 2260 (1992).

[194] M. Zachau, J. A. Kash, and W. T. Masselink, Phys. Rev. B **44**, 4048 (1991).

[195] B. P. Zakharchenya, P. S. Kop'ev, N. D. Mirlin, D. G. Polakov, I. I. Reshina, V. F. Sapega, and A. A. Sirenko, Sol. State Comm. **69**, 203 (1989).

[196] J. Schmidt, M. R. C. Hunt, P. Miao, and R. E. Palmer, Phys. Rev. B **56**, 9918 (1997).

[197] D. Li, S. Velasquez, and S. E. Schnatterly, Phys. Rev. B **49**, 2969 (1994).

[198] G. Gensterblum, J. J. Pireaux, P. A. Thiry, R. Caudano, J. P. Vigneron, Ph. Lambin, A. A. Lucas, and W. Krätschmer, Phys. Rev. Lett. **67**, 2171 (1991).

[199] A. A. Lucas, G. Gensterblum, J. J. Pireaux, P. A. Thiry, R. Caudano, J. P. Vigneron, Ph. Lambin, and W. Krätschmer, Phys. Rev. B **45**, 13694 (1992).

[200] V. V. Sobolev and E. L. Busypina, Semiconductors **33**, 26 (1999).

[201] L. Margulis, G. Salitra, R. Tenne, and M. Talianker, Nature (London) **365**, 113 (1993).

[202] P. A. Parilla, A. C. Dillon, K. M. Jones, G. Riker, D. L. Schulz, D. S. Ginley, and M. J. Heben, Nature (London) **397**, 114 (1999).

[203] M. Remskar, A. Mrzel, Z. Skraba, A. Jesih, M. Ceh, J. Demšar, P. Stadelmann, F. Lévy, and D. Mihailovic, Science **292**, 479 (2001).

[204] F. R. Gamble, F. J. DiSalvo, R. A. Klemm, and T. H. Geballe, Science **168**, 568 (1970).

[205] H. Fernández-Morán, M. Ohstuki, A. Hubino, and C. Hough, Science **174**, 498 (1971).

[206] SAES Getters, Cologne, Germany. Evaporation current was set to 5 Ampere.

[207] J. A. Wilson and A. D. Yoffe, Adv. Phys. **18**, 193 (1969).

[208] N. W. Ashcroft and N. D. Mermin, *Solid State Physics*, Holt, Rinehard and Winston, New York, (1976).

[209] C. Ramirez, R. Adelung, R. Kunz, L. Kipp, and W. Schattke, Phys. Rev. B **71**, 35426 (2005).

[210] H. Rydberg, M. Dion, N. Jacobson, P. Hyldgaard, S. I. Simak, D. C. Langreth, and B. I. Lundqvist, Phys. Rev. Lett. **91**, 126402 (2001).

[211] J. S. Ahn, J. Bak, H. S. Choi, T. W. Noh, J. E. Han, Y. Bang, J. H. Cho, and Q. X. Jia, Phys. Rev. Lett. **82**, 5321(1999).

[212] A. Husmann, J. Brooke, T. F. Rosenbaum, X. Yao, and J. M. Honig, Phys. Rev. Lett. **84**, 2465(2000).

[213] L. Perfetti, A. Georges, S. Florens, S. Bierman, S. Mitrovic, H. Berger, Y. Tomm, H. Höchst, and M. Grioni, Phys. Rev. Lett. **90**, 166401(2003).

[214] J. A. Wilson, F. J. DiSalvo, and S. Mahajan, Phys. Rev. Lett. **32**, 882 (1974).

[215] F. Jellinek, J. Less Common Met. **4**, 9 (1962).

[216] S. E. Stoltz, H. I. Starnberg, and L. J. Holleboom, Phys. Rev. B **67**, 125107 (2003).

[217] R. H. Friend and A. D. Yoffe, Adv. Phys. **36**, 1 (1987).

[218] W. Y. Liang, Electronic Properties of Transition Metal Dichalcogenides and their Intercalation Complexes, Vol. **148** of NATO Advanced Studies Institute (Plenum, New York, 1986).

[219] E. Spiecker, A. K. Schmid, A. M. Minor, U. Dahmen, S. Hollensteiner, and W. Jäger, Phys. Rev. Lett. **96**, 086401 (2006).

[220] B. Burk, R. E. Thomson, A. Zettl, and J. Clarke, Phys. Rev. Lett. **66**, 3040 (1991).

[221] H. J. Crawack and C. Pettenkoffer, Solid State Commun. **118**, 325 (2001).

[222] G. Grüner, *Density waves in solids*, Cambridge, Perseus (2000).

[223] J. Kröger, Rep. Prog. Phys. **69**, 899 (2006).

[224] P. Fazekas and E. Tosatti, Philos. Mag. B **39**, 229 (1979).

[225] F. Zwick, H. Berger, I. Vobornik, G. Margaritondo, L. Forró, C. Beeli, M. Onellion, G. Panaccione, A. Taleb-Ibrahimi, and M. Grioni, Phys. Rev. Lett. **81**, 1058 (1998).

[226] B. Dardel, M. Grioni, D. Malterre, P. Weibel, Y. Baer, and F. Lévy, Phys. Rev. B **45**, R1462 (1992).

[227] B. Dardel, M. Grioni, D. Malterre, P. Weibel, Y. Baer, and F. Lévy, Phys. Rev. B **46**, 7407 (1992).

[228] M. Bovet, S. van Smaalen, H. Berger, R. Gaál, L. Forrò, L. Schlapbach, and P. Aebi, Phys. Rev. B **67**, 125105 (2003).

[229] R. Adelung, F. Ernst, A. Scott, M. Tabib-Azar, L. Kipp, M. Skibowski, S. Hollensteiner, E. Spiecker, W. Jäger, S. Gunst, A. Klein, W. Jägermann, V. Zaporojtchenko, and F. Faupel, Adv. Mater. **14**, 1056 (2002).

[230] All images were processed using Nanotec WSxM [231].

[231] I. Horcas, R. Fernández, J. M. Gómez-Rodríguez, J. Colchero, J. Gómez-Herrero, and A. M. Baro, Rev. Sci. Instrum. **78**, 013705 (2007).

[232] M. Wilkening, W. Küchler, and P. Heitjans, Phys. Rev. Lett. **97**, 65901 (2006).

[233] R. M. Feenstra, A. Vaterlaus, D. G. Petit, Phys. Rev. Lett. **71**, 1176 (1993).

[234] J. F. Zheng, N. Newman, X. Liu, E. R. Weber, D. F. Ogletree, and M. B. Salmeron, Phys. Rev. Lett. **72**, 1490 (1994).

[235] Z. F. Zheng, M. B. Salmeron, and E. R. Weber, Appl. Phys. Lett. **64**, 1836 (1994).

[236] R. de Kort, M. C. M. M. Van der Wielen, A. J. A. van Roij, and H. van Kempen, Phys. Rev. B **63**, 125336 (2001).

[237] A. M. Yakumin, A. Yu. Silov, P. M.Koenraad, J. H. Wolter, W. van Roy, J. De Boek, J.-M. Tang, and M. E. Flatté, Phys. Rev. Lett. **92**, 216806 (2004).

[238] M. H. Wangbo, J. Ren, S. N. Maganov, H. Bengel, B. A. Parkinson, and A. Suna, Surf. Sci **326**, 311 (1995).

[239] R. Schlaf, D. Louder, M. W. Nelson, and B. A. Parkinson, J. Vac. Sci. Technol. A. **15**, 1466 (1997).

[240] Th. Matthes, Ch. Sommerhalter, A. Rettenberger, P. Bruker, J. Boneberg, M. Ch. Lux-Steiner, and P. Leiderer, Appl. Phys. A **66**, 1007-1011 (1998).

[241] D. L. Greenaway and R. Nitsche, J. Phys. Chem. Solids **26** , 1445 (1965).

[242] Ph. Gütlich, A. Hauser, and H. Spiering, Angew. Chem. Int. Ed. Engl. **33**, 2024 (1994).

[243] A. Hauser, Top. Curr. Chem. **234**, 155 (2004).